2013

Evaluation of an Enhanced Steel Orthotropic Bridge Deck for Temporary Interstate Applications

Ellen Sarah Grace Sweet
Lehigh University

Evaluation of an Enhanced Steel Orthotropic Bridge Deck for Temporary Interstate Applications

by

Ellen Sarah Grace Sweet

A Thesis

Presented to the Graduate and Research Committee

of Lehigh University

in Candidacy for the Degree of

Master of Science

in

Structural Engineering

Lehigh University

December 2013

This thesis is accepted and approved in partial fulfillment of the requirements for the Master of Science

_____
Date

_____
Dr. Sougata Roy
Thesis Advisor
ATLSS Engineering Research Center
Lehigh University

_____
Dr. Richard Sause
Thesis Advisor
Department of Civil and Environmental Engineering
Engineering, Lehigh University

_____
Dr. Panayiotis Diplas
Chairperson
Department of Civil and Environmental Engineering
Engineering, Lehigh University

Acknowledgements

The author would like to thank Dr. Sougata Roy for his guidance and supervision during the research process, and his direction and patience during the completion of this thesis. Testing was conducted at the Fritz Laboratory of Lehigh University, and much gratitude is due towards the staff of Fritz Lab for their contributions to the successful completion of the project. The post-mortem evaluation of the specimen was conducted at the ATLSS Engineering Research Center of Lehigh University, and sincere thanks towards the staff of the ATLSS Center are extended as well. The author would like to personally thank Mr. Gene Matlock and Mr. Darrick Fritchman for their encouragement.

The author would also like to thank LARSA Inc., for their generosity in providing the LARSA 4D software free of cost for this research work.

The help of Yeun Chul Park throughout the research and testing process cannot be understated. The author would like to thank him for his previous work, which influenced the advancement of this project, and for his help during testing, which was greatly appreciated.

Sincere gratitude is extended towards my wonderful parents and family, whose encouragement was a necessary aspect of this pursuit. The author would also like to thank her friends at the ATLSS Center, for their support and open ears.

Finally, gratitude must be expressed towards the Lehigh University Rowing Coaches and Team, which in hiring the author as a graduate assistant allowed her to come to graduate school.

Table of Contents

List of Tables

List of Figures

ABSTRACT

Recently, there has been an interest in to enhancing the longevity of temporary bridge structures. These structures have successfully survived up to five years in-service in rural areas and secondary roads. However, the decks develop significant fatigue cracking within eight months when subjected to heavy truck traffic.

A pilot study of the existing deck design including 3D Finite Element Analyses and static and fatigue testing of three full size specimens showed that the stringer-to-tube connections were the most fatigue critical deck details. To improve the fatigue performance, the deck design was enhanced with a thicker deck plate, thicker transverse tubes, and rearrangement of the stringer-to-deck plate welds.

Grillage analyses of the deck designs, validated against the 3D FEA results, were performed to assess the global behavior of the decks under load. In general, the grillage analysis results were accurate along the deck stringers. Two full size enhanced bridge decks were tested under static and fatigue loading. The enhanced deck deflected less than the existing deck, and had some reduction in stresses. Both decks had fatigue cracking at the stringer-to-tube fillet welded connections after about 9 million cycles; this was less than the target lifespan. Post-mortem evaluation revealed that the subpar fatigue performance of the decks was due to poor weld quality. The fatigue life of the connection detail was found to be on the AASHTO Category D design curve in the finite life regime.

Quality weld fabrication at the stringer-to-tube connections is recommended for improved fatigue performance of the enhanced deck design. In addition, asymmetric rearrangement of the stringer-to-tube welds may be investigated to increase the flexibility of the stringer web and reduce the out-of-plane bending stresses.

1. INTRODUCTION

1.1 Background

The performance of an enhanced orthotropic bridge deck designed primarily as a temporary structure for emergency bridge replacement, or for large construction projects, was evaluated. The earlier version of this design has successfully survived four to five years in rural areas and secondary roads that are lightly traveled and typically do not experience heavy truck traffic. In busy urban roadways and/or on interstates, where the deck is subject to heavy truck traffic, the life of this deck design has been limited to eight months due to fatigue cracking of several welded connections.

The deck panel is used in a modular pre-fabricated steel through truss bridge, shown in Figure 1. The trusses are comprised of cross braced square panels. The floor framing system consists of transoms that span transversely between the lower chords of the trusses at panel points, and lateral/sway bracing at the bottom flange of the transoms. The orthotropic deck panels span across the top flange of the transoms.

The temporary bridge is designed so it can be erected quickly, with minimal heavy equipment. The primary objective of the deck design is to produce a light weight construction with an optimal balance of strength that is also economical in its reduced costs of fabrication, handling, and erection. This results in a relatively flexible deck design that is susceptible to fatigue crack growth at several locations, mainly due to large localized distortion of the deck under wheel loads.

In light of this, this study was conducted to evaluate the performance of the temporary bridge deck on interstate highways, where it would be subjected to a large volume of truck traffic. The lifetime would be limited to a time period that would exceed

a few months, but be much less that the requirements of a permanent bridge deck, which would require infinite life.

In 2009, the performance of the earlier version, or the existing design, of the bridge deck (version 1 deck, or the V1 deck) was analytically and experimentally evaluated at Lehigh University. The study had two objectives: to evaluate the fatigue performance of the V1 deck under AASHTO loading, and to recommend cost-effective design improvements to enhance the fatigue performance of the bridge deck panel.

A three-dimensional (3D) Finite Element Analysis (FEA) of the deck was performed, where the model of a simply supported V1 bridge deck panel, including the supporting transoms, was subjected to multiple longitudinal and transverse dispositions of wheel loads from the AASHTO fatigue truck in tandem configuration. The purpose of the analysis was to determine the response characteristics of the deck, and to identify the critical locations of the deck for instrumentation during testing.

Due to the limited deck width, only one half of the tandem axle could be accommodated on the deck surface. The load pattern corresponded to two 10 in. (254 mm) by 20 in. (508 mm) load areas, spaced 4 ft. (1.2 m) from the load area centers. The FEA studies showed that the load disposition, illustrated in Figure 3, produced the most severe stresses at the critical connections of the deck. In this load case, identified as LC-5 in the V1 deck study, the load areas were positioned symmetrically about the longitudinal center line of the deck, with one load area centered on the inner transverse tube T2, and the second load area centered 6 in. (152 mm) from the deck end.

Three full size specimens were subjected to static and fatigue testing. The wheel loads were simulated by two load pads having a 10 in. (254 mm) by 20 in. (508 mm)

footprint, each loaded by a hydraulic actuator. All three decks were instrumented to determine the response of the deck under the simulated wheel load, and to observe the stress at critical locations. The first specimen was extensively instrumented with 91 strain gauges. The second and third specimens were instrumented with 16 strain gauges each. Additionally, load cells and displacement transducers were used during the static tests for each specimen.

For the fatigue tests of the first two specimens, a load range of 7 kip (31.1 kN) at each load pad was applied to represent the existing AASHTO LRFD Bridge Design Specifications (BDS), as the fatigue performance of the deck was unknown. Specimen #1 survived 10 million cycles without any observable fatigue damage. Specimen #2 had developed a fatigue crack at the stringer-to-tube weld near the weld termination at the lower end that grew around the tube wall after 9.4 million cycles. The postmortem evaluation showed typical fatigue crack growth from micro-discontinuities at the weld toe.

On the third specimen, a load range of 21 kip (93.4 kN) was applied to acknowledge that overloaded trucks are a common occurrence on highways, and can be as much as three times the design fatigue loading. Specimen #3 endured 400,000 cycles and developed fatigue cracks that originated from the stringer-to-tube welded connection.

The objective of the current study was to evaluate the improved performance of the V2 deck compared to the V1 deck. Accordingly, the V2 deck specimens were tested under similar conditions and simulated AASHTO loading as the V1 deck. Three V2 deck specimens were provided by the manufacturer, however only two were subject to static and fatigue testing.

A grillage analysis of the V2 deck was performed replicating the test setup, to determine the global response characteristics of the deck. The deck specimens were subsequently subjected to static and fatigue testing. For easy comparison, the specimens were instrumented similar to the V1 deck specimens.

1.2 Description of the Deck

The V1 and V2 decks were geometrically identical, except for the deck plate and tubes. An overview of the decks is shown in Figure 2. The decks consisted of a 6 ft. (1.8 m) by 10 ft. (3.0 m) deck plate that was $^{3/}_{16}$ in. (4.76 mm) thick on the V1 deck, and $^{3}/_{8}$ in. (9.53 mm) thick on the V2 deck. The deck plate was stiffened by ten stringers in the longitudinal direction, and four tubes in the transverse direction.

The stringers were specially ordered S5x7.2 shapes. In the thesis, the stringers are numbered as S1 through S10. The eight inside stringers were spaced 7 $^{19}/_{32}$ in. (192.9 mm) apart, and the two outside stringers were spaced 7 $^{11}/_{32}$ in. (187.5 mm) apart. The stringers were connected to the deck plate using $^{3}/_{16}$ in. (4.76 mm) intermittent fillet welds. The welds were 1 $^{1}/_{2}$ in. (38.1 mm) long at 11 in. (279 mm) centers, and had an asymmetric layout on either side of the top stringer flange.

The transverse tubes had an exterior diameter of 2 $^{7}/_{8}$ in. (73.03 mm). For the V1 and V2 decks, the tubes were $^{13}/_{64}$ in. (5.16 mm) and $^{17}/_{64}$ in. (6.75 mm) thick, respectively. In the thesis, the tubes are labeled as T1 through T4. The tubes passed through the center of the stringer web and were placed at 12 in. (305 mm) centers about the mid-span. The tubes were connected to the stringer webs using two 2 in. (50.8 mm) long $^{3}/_{16}$ in. (4.76 mm) fillet welds, placed symmetrically about the horizontal axis of the

tubes. These welds were placed only on one side of the stringer, and on the same side for all stringers, along the middle of the tube perimeter, symmetrical about its vertical axis.

End plates were provided over the entire deck width, at the longitudinal ends of the deck, to act as vertical load carrying elements that bear on the top flange of the supporting transoms. The plates were $^1/_4$ in. (6.35 mm) thick and 5 in. (127 mm) high, and were welded to the stringer flanges and webs using $^3/_{16}$ in. (4.76 mm) intermittent fillet welds. The end plates extended up to the deck plate, but were not welded to the deck plate itself. Tight fabrication tolerances were used to ensure uniform bearing along the entire surface between the end plate and the transom top flange.

Two cover plates were welded to the soffit of the outer two stringers on either side of the deck, using $^3/_{16}$ in. (4.76 mm) intermittent fillet welds. The cover plates were $^1/_4$ in. (6.35 mm) thick, 94 $^1/_2$ in. (2.4 m) long, and 8in. (203 mm) wide. The cover plates were centered in the longitudinal direction, and the width was centered with the stringers.

1.3 Outline

This thesis contains six chapters and two appendices. The first chapter provides the background of the study, including a description of the previous study and test results, as well as an overview of the current study and study objectives.

The second chapter presents the grillage analyses conducted on the V1 and V2 bridge decks, and the validation of the grillage model with respect to the FEA results and physical measurements of the V1 deck.

The third chapter provides the details of the static and fatigue tests of the V2 deck, including the test set up, loading, test procedures, and instrumentation.

The fourth chapter discusses the static test results of the V2 deck. The response of the deck elements under the test loading are described in this chapter. The comparisons between the grillage analysis results and the static test results, and the V1 and the V2 decks are also presented in this chapter.

The fifth chapter discusses the fatigue test results of the V2 deck, and the performance of fatigue critical details under the fatigue loading. Additionally, it presents the post-mortem evaluation of the fatigue fractures, including characterization of the origin and growth of the fatigue cracks.

The sixth and final chapter concludes the study, with further recommendations for possible improvement of the deck design, and possible future studies.

2. GRILLAGE ANALYSIS OF DECKS

Grillage analyses of the V1 and V2 decks were carried out to evaluate and compare the global response of the two bridge decks. The grillage model was created and analyzed using LARSA 4D, a commercially available structural analysis software. The background of grillage analysis, modeling, and verification of the V1 deck model, and grillage analysis results of the V2 deck are presented in this section. The grillage analysis results of the V2 deck are compared with the experimental results in Section 4.

2.1 Background to Grillage Analysis

Grillage analysis refers to the analysis of a bridge deck by idealization as a grillage of interlocking members. Introduced first in 1964 by Lightfoot, this analysis method originated from plate bending equations. A comprehensive treatise of this analysis technique is provided by Hambly (1975, 1991) and Jaeger (1982). This analysis provides an overview of the global deck response; it shows the general distribution of forces or stress resultants in a bridge deck, and how the live loads are distributed. Compared to 3D FEA, grillage analysis of a bridge deck is efficient (less computationally demanding) and can be conducted with commonly available 2D structural analysis software. When modeled adequately, the grillage analysis can yield consistent and accurate results. However, unlike 3D FEA, where the structure is modeled as a continuum, the grillage analysis of discrete interlocking members cannot accurately assess local stresses in members and connections. Only nominal stresses can be estimated based on strength of material calculations using the member forces and section properties of a section.

In grillage analysis, the 3D bridge deck is idealized or modeled as a 2D grid of longitudinal and transverse members. Each member represents a finite section normal to the member and is assigned the structural properties of that section. In short, the longitudinal members represent longitudinal deck properties, and the transverse members represent transverse deck properties. It is assumed that compared to the bridge deck it represents, an ideal grillage would have identical deflections, and develop identical moments, shears, and torsions at the member intersections.

2.2 Grillage Model Configuration

The V1 and V2 deck panels had similar geometry, allowing the same grillage layout to be used for both. This section discusses the process of developing the grillage model. Any differences between the V1 and V2 decks are appropriately noted.

The grillage model of the deck is shown in Figure 4 and the grillage idealization is shown in Figure 5, with the grillage model overlaid on a 3D rendering of the deck. The deck was modeled as a grillage of 10 longitudinal members and 12 transverse members. Due to symmetry of the modeled deck in the longitudinal and transverse directions about the deck centerlines (the actual deck is not symmetric in the transverse direction because of asymmetry in the welded connections, which could not be incorporated in the grillage model), the discussion in this section is presented with respect to five longitudinal members and six transverse members. These are labeled in Figures 4 and 5, as L1 through L5 for the longitudinal members, Tr1 through Tr5, and EP, for the transverse members.

In grillage idealization, a bridge deck is usually sectioned based on the cross section, with due considerations of the structural behavior and lines of designed strength.

In the grillage mesh of the deck, the members were aligned with the stringers. The deck was longitudinally sectioned in the middle between the S-beams, and the grillage member cross sections were defined at the centroid of the sections.

The interior members, L3, L4, and L5, had identical cross sections that included the S-beam and half of the deck plate on either side. The member L2 also included half of the deck plate on either side, but due to the shorter spacing between the two exterior stringers than the interior stringers, member L2 had a smaller section width than L3, L4 and L5. In addition, where the edge stringers were connected by a cover plate, the cross section of L2 included half of the cover plate. The edge member L1 included one half of the deck plate towards the inside of the deck, and the remaining width of the deck plate on the outside. Similar to L2, the member cross section for L1 included half of the cover plate, when present. Due to variations in the cross sections, the centroids were located in different planes. However, the grillage was modeled such that all members were placed in one plane through the centroid of the sections. In the actual deck, the depth of the neutral axis varied across the width, whereas in the grillage model, the neutral axis remained in the same plane. The division of the sections, the positioning of the grillage members, and the placement of the sections in the idealized grillage are shown in Figure 6, for sections without a cover plate, and in Figure 7 for sections that included a cover plate. This difference in the neutral axes between the physical and the idealized deck does not significantly influence the results of the grillage analysis, and may be ignored (Hambly 1991).

In the transverse direction, four transverse members were aligned with the transverse tubes. These members had identical cross sections and were symmetrical about

the vertical axis, through the tube. The remaining segments of the deck were divided into six sections of equal width. In addition, two sections representing the end plates only were included. The division and the placement of these members in the grillage are shown in Figures 8 and 9, which show the cross sections without and with the cover plate, respectively. The interior members were 12 in. (305 mm) wide and included the deck plate across the section width. Members Tr4 and Tr5, containing the transverse tubes, were identical. These members also included the cover plate joining the bottom flange of the stringers, where present. Except at locations were the cover plates were present, members Tr1, Tr2, and Tr3 were identical and contained only the deck plate. For member Tr3 the cover plate extended over the entire section width; for member Tr2, the cover plate extended over 11 in. (279 mm) of the section. The cover plate did not extend into member Tr1, which was constant over the entire width of the deck. The end plates at each deck end were considered as individual members (labeled EP). In the deck fabrication, these end plates were not attached to the deck plate, but were welded to the stringers, so any load applied on the deck plate had no direct path to the end plates. Due to this, instead incorporating the end plate into the adjacent member (Tr1), the deck plate and the end plate were modeled as two separate members. Although the centroids of different sections lay on different planes, all members of the grillage were placed in one plane through the centroid of the section.

2.3 Section Properties

The member section properties for the all members used in the grillage model were computed using an excel spreadsheet. The spreadsheet was created to determine the section centroids, moments of inertia, St.Venant torsion constant, and the warping

moment of inertia, for all cross sections. The warping moment of inertia for each cross section was determined using the equations for thin walled plated sections provided by Galambos (1978). The section properties were also verified in LARSA 4D section composer.

The two exterior stringers, when connected by the cover plate, formed a closed beam section, as shown in Figure 10. Since the torsional resistance of a closed section is significantly greater than the torsional resistance of an open section due to the larger contribution of St. Venant torsion, the torsional section properties of L1 and L2, in the presence of the cover plate, were estimated as half the torsional properties of a box beam (Hambly 1991).

The torsional section properties of members Tr4 and Tr5 were relatively large due to the tube. The thing-walled, doubly-symmetric closed section of the tube does not warp, and therefore does not contribute to the section's ability to resist warping. However, the cover plate changed the centroid of the cross section, and influenced the calculations of the warping torsion constant of the section. Thus, the transverse sections that included a cover plate and tube had the largest ability to resist torsion.

A summary of the calculated section properties of the V1 deck grillage members is shown in Table 1. The calculated section properties of the V2 deck grillage members are summarized in Table 2.

2.3.1 Equivalent Torsion Constant

The transverse distribution of loads in a slab-girder type bridge deck, similar to the deck under investigation, primarily depends of the torsional stiffness of the longitudinal members (Hambly 1991). Accurate representation of the torsional section

properties is essential for procuring an accurate structural response of the deck from its representation, particularly the transverse load distribution. An underestimation of the torsional stiffness would result in a model that is more flexible, with poor transverse load distribution. Therefore, an over estimation of the torsional stiffness would result in a stiffer deck and more favorable response than in actuality.

The total torsional resistance of a section consists of two components: the St.Venant's torsion (also described as pure torsion), and the warping torsion. The two components are related to the applied torsion moment through the twist angle, as presented in the well-known third order ordinary linear differential equation (ODE).

$$T(x)=GJ\frac{d\phi(x)}{dz}-EC_w\frac{d^3\phi(x)}{dz^3} \qquad \text{Eq. 1}$$

where *T(x)* is the applied torsional moment distribution through the length of the member (function of x). *G* is the shear modulus, *E* is the modulus of elasticity, *J* is the pure torsion constant of the cross-section, and C_w is the warping torsion constant. The St.Venant's torsion, manifested as a rigid body twist without distortion of the cross section, is represented by the first part of the equation. The second part of the equation is the warping torsion component. Warping torsion is manifested by distortion, or warpage, of the cross section associated with variable out-of-plane (in the axial direction of the member) deformation of the section. For closed sections, the torsion response is dominated by St.Venant's torsion. For thin walled open sections, such as the stringers, the ability of the beam to resist torsion is mainly attributed to the warping of its flanges. Thus, to accurately determine the torsion response of the deck, warping of the beams must be included.

The general solution of the third order ODE shown in Eq. 1 contains seven constants. In general, commercially available structural analysis software uses elements having six degrees of freedom (DOF) per node, which can only solve for six unknowns. This issue can be addressed by an element with one additional DOF per node that captures axial warping deformation. However, this element is not available in most commercial software (Sanchez 2011).

Due to this limitation, commercial structural analysis software neglects the warping torsional resistance of a section, and calculates the member torsional response including only the contribution of the St.Venant torsion (Sanchez 2011). This method is only effective for members having symmetrical thin-walled closed cross sections. However, in the case of the V1 and V2 decks, which employed thin-walled open sections for the longitudinal stringers, neglecting of warping torsion would neglect the significant contribution of flange warping on the torsional resistance of the member.

Another technique to better represent the torsional properties of a thin-walled open section is to use an equivalent torsion constant (Ahmed and Weisgerber 1996). This method alters the pure torsion constant, *J*, to include the effects of flange warping. For commercial structural analysis software that allows the creation of user defined member properties, the equivalent torsion constant is a viable option for accurately incorporating the torsional properties and warping resistance of a member.

It should be noted that neither the additional warping DOF nor the equivalent torsion constant method can reproduce the effects of cross section distortion, or web distortion, under torsional loading. However, web distortion typically has a minor effect on the torsional response of an open section (Sanchez 2011). In addition, for the

temporary bridge deck, the stringers were small enough that the likelihood of web distortion was small, and not considered to be an issue.

As presented by Ahmed and Weisgerber (1996), the equivalent torsion constant for thin walled open sections is determined from the general solution of the governing differential equation (Eq. 1) for a constant applied torque and given boundary conditions. The general solution of the torsion equation, where ϕ is the angle of twist at a distance x along the beam, is given as:

$$\phi(x)= \frac{T(x)x}{GJ} + A_1\sinh(px) + A_2\cosh(px) + A_3 \qquad \text{Eq. 2}$$

In Eq. 2, A_1, A_2, and A_3 are constants that are determined from the boundary conditions; p is a normalized parameter based on the member section and material properties, and is defined as:

$$p^2= \frac{GJ}{EC_w} \qquad \text{Eq. 3}$$

For steel, E was taken as 29,000 ksi (200,000 MPa), and G was determined from the relationship $E = 2G(1 + v)$. Using an assumed poisson's ratio of 0.30, G was found to be 11,150 ksi (76,880 MPa). For open cross sections that could be broken into thin-walled rectangles, the torsion constant J was determined as:

$$J_{twos}= \sum\left(\frac{bt^3}{3}\right) \qquad \text{Eq. 4}$$

In this equation, b is the width and t is the thickness for each rectangle. The torsion constant for the tube was determined as:

$$J_{tube}= \frac{\pi}{2}(R_o^4 - R_i^4) \qquad \text{Eq. 5}$$

Where R_o is the tube outer radius, and R_i is the tube inner radius. The total torsion constant for sections that included a tube and other open sections was calculated as the sum of Eq. 4 and Eq. 5, where

$$J_{total} = J_{twos} + J_{tube} \quad \text{Eq. 6}$$

The warping torsional constant, C_w, was determined using equations for plate warping (Galambos 1978). In plate elements, between points of intersection, the unit warping properties vary linearly. After determining the section's normalized unit warping, ω_n, the warping moment of inertia, or the torsion constant C_w, can be calculated as:

$$C_w = \frac{1}{3}\sum_{i=0}^{i=n}(\omega_{ni}^2 + \omega_{ni}\omega_{nj} + \omega_{nj}^2)t_{ij}b_{ij} \quad \text{Eq. 7}$$

where ω_{ni} and ω_{nj} represent the normalized unit warping at either end of the plate. An illustration of this is shown in Figure 12. For cross sections that included a tube, the tube being a closed section was resistant to warping and was not included in the calculation of the warping constant.

For calculation of the equivalent torsion constant, Ahmed and Weisgerber (1996) considered three boundary conditions: members with torsionally rigid connections at either end, members with one rigid connection and one simple connection, and members with partial restraint at both ends. For the given boundary conditions, the constants A_1, A_2, and A_3 could be solved using the known values at $x = 0$, and $x = L$, where L is the total length of the member. Knowing these constants, the equivalent torsion constant, J_{eq}, could be found.

For instance, for a beam fixed against warping at its ends, the boundary conditions are $\phi(0) = 0$, $\phi'(0) = 0$, and $\phi'(L) = 0$. When these boundary conditions are applied to Eq. 2, the unknown constants are solved to be:

$$A_1 = -\frac{T}{GJp} \quad \text{Eq. 8}$$

$$A_2 = \frac{T}{GJ}\,\frac{\cosh(pL)-1}{p\sinh(pL)} \quad \text{Eq. 9}$$

$$A_3 = -\frac{T}{GJ}\,\frac{\cosh(pL)-1}{p\sinh(pL)} \qquad \text{Eq. 10}$$

When these values are substituted into the general torsion equation shown in Eq. 2, the twist angle in a member with fixed flanges (warping restrained) subjected to constant torque is:

$$\phi(x) = \frac{Tx}{GJ} - \frac{T}{GJp}\sinh(px) + \frac{T}{GJ}\frac{\cosh(pL)-1}{p\sinh(pL)}\cosh(px) - \frac{T}{GJ}\frac{\cosh(pL)-1}{p\sinh(pL)} \qquad \text{Eq. 11}$$

Therefore, the relative rotation between the beam ends is

$$\phi = \frac{T}{GJ}\left[L - \frac{\sinh(pL)}{p} + \frac{\cosh(pL)-1}{p\sinh(pL)}\cosh(pL) - \frac{\cosh(pL)-1}{p\sinh(pL)}\right] \qquad \text{Eq. 12}$$

which can be rewritten as

$$\phi(x) = L\frac{T}{GJ_{eq}} \qquad \text{Eq. 13}$$

where J_{eq} is the equivalent torsion constant for the member. In the same way, the equivalent torsion constant can be determined for a member with an end connection that is free to warp, and an end connection that is fixed. Calculation of the equivalent torsion constant for the partially restrained beam was derived through use of the warping springs, which is not presented here as it is not readily applicable for the bridge deck.

For a beam under constant torsion with fixed-fixed, and fixed-free end conditions, the equivalent torsions are given as (Ahmed and Weisgerber 1996):

$$J_{eq(fx\text{-}fx)} = J\left[1 - \frac{\sinh(pL)}{pL} - \frac{[\cosh(pL)-1]^2}{p\,L\sinh(pL)}\right]^{-1} \qquad \text{Eq. 14}$$

$$J_{eq(fx\text{-}fr)} = J\left[1 - \frac{\sinh(pL)}{pL}\cosh(pL)\right]^{-1} \qquad \text{Eq. 15}$$

As is evident, J_{eq} is influenced by the unbraced length of the member (L). An increase in the unbraced length greatly reduces the equivalent torsion constant, regardless of end conditions. For the analysis of a permanent bridge, the unbraced length is usually

defined as the "distance between cross-frames, regardless of whether there are cross-frames on both sides of the web… or on only one side" (Sanchez 2011). For the subject bridge deck, the top flange of the stringers was connected to the deck plate by intermittent welds. As a result, the deck plate provided some lateral restraint to the top flange of the stringers. Due to the intermittent fillet welds, and the staggering of these welds on either side of the stringer flange, this restraint was not continuous. Considering the flexibility of the thin deck plate, the stiffness and extent of this lateral restraint (bracing) was not clear. As an approximation, the unbraced length of the longitudinal members (the deck stringers) was considered to be the distance between the stringer-to-deck plate welds, which resulted in a maximum unbraced length of 4.75 in. (120.7 mm). For the transverse members, including the tubes, the distance between the top flanges of the stringers, or $5\ ^{3}/_{32}$ in. (129.4 mm) was considered as the largest unbraced length.

For most sections, the use of the equivalent torsion constant increased the torsional section properties, usually by an order of magnitude or more. This is shown in Table 1 and Table 2, which present a summary of the calculated section properties for the V1 and V2 deck grillage members, respectively.

2.3 Boundary Conditions

In service, the bridge deck was supported at its longitudinal ends on the top flange of the transoms. The boundary conditions of the grillage model were set to reflect the service conditions of the bridge deck. From the FEA of the V1 deck conducted in 2009, it was found that modeling the transoms as rigidly supported (as they were in the test set up, described in Section 3.3) did not significantly influence the deck response. The transoms were not modeled in the grillage, therefore it was assumed the transoms acted

as rigid supports. The deck was restricted in the vertical direction along both longitudinal ends of the deck. At the locations of the deck bolt channels, the deck was restricted in all three coordinate directions. The boundary conditions of the grillage model are illustrated in Figure 11.

2.5 Loading

As described in Section 1.1 and discussed further in Section 3.2, the applied load followed the fatigue loading requirements of the AASHTO LRFD BDS for orthotropic decks. The design truck reproduced from the BDS in shown in Figure 13, which illustrates the recommended truck tire footprint for orthotropic deck design. The truck consists of five axles; each axle is spaced 6.0 ft apart in the transverse direction. The lead, or tractor axle, has two 8.0 kip (35.6 kN) wheel loads distributed over a 10 in. (254 mm) by 10 in. (254 mm) tire contact area. The lead axle is followed by two rear tandem axles of the trailer, and tandem axle is comprised of two 16.0 kip (71.2 kN) axles spaced 4.0 ft. (1.2 m) apart. Each axle in the tandem configuration contains an adjacent pair of wheel loads at each end, distributed over a 10 in. (254 mm) by 20 in. (508 mm) tire contact area (AASHTO 2012).

As reported earlier with respect to the studies on the V1 deck, the deck, being 6 ft. (1.8 m) wide, will only accommodate one side of the fatigue design truck. The largest load on the deck is under the weight of one half of the tandem axle. Therefore, the deck was analyzed and fatigue tested under two 16.0 kip (71.2 kN) wheel loads distributed over two 10 in. (254 mm) by 20 in. (508 mm) tire contact areas, spaced 4 ft. (1.2 m) apart in the longitudinal direction.

For finite fatigue life design, the design truck weight is reduced by a load factor of 0.75 to represent the effective truck weight in the truck traffic spectrum (AASHTO 2012). To account for the inertial effect during by dynamic loading, the truck weight is increased an impact factor of 15% (AASHTO 2012). This results in a fatigue design load of approximately 7 kip (31 kN) (16 kip * 0.75 * 1.15). However, weigh-in-motion studies conducted across the country indicate that overloaded trucks are a common occurrence. Often, the truck gross vehicle weight is nearly three times the weight of the effective fatigue design truck. In addition, field measurements on signature bridges around New York City have shown that for orthotropic decks the fatigue limit state load is three times the fatigue design load. In the absence of any field measurements on temporary bridge decks in service, a load of 22 kip (98 kN) per wheel, or approximately three times the finite life fatigue design load, was assumed to be the upper bound load for the bridge deck in service. The test load is discussed fully in Section 3.2.

The 22 kip (98 kN) load was used as the maximum load for the static tests conducted on the first and third V1 deck specimens, and the V2 deck specimens. The load was applied to both load pads simultaneously, resulting in a pressure of 110 psi (758 kPa) applied over the two 10 in. (254 mm) by 20 in. (508 mm) load pad areas.

As noted in Section 1.1, the FEA of the V1 deck identified that the most critical longitudinal and transverse bending effects in the stringers and tubes occurred when the load areas were symmetrically spaced about the deck longitudinal centerline. When the fatigue design truck tandem axle crosses the deck in this position, the most critical stresses in the stringer web gaps and the stringer-to-tube connections occurred when the

interior load pad was centered over tube T2 (load area center 6 in. (152 mm) from deck centerline) and the exterior load area centered 6 in. (152 mm) from the deck end.

To represent this loading for the grillage analysis in LARSA, the load was input as a moving pressure that followed a load path. An illustration of the load areas and paths on the grillage model is shown in Figure 14. In the grillage model, the load paths must follow the existing members, so two load paths were defined along the longitudinal members that coincided with stringers S5 and S6. Each load path was assigned half of the applied load, which was defined as a pressure of 110 psi (758 kPa) on two 10 in (254 mm) by 10 in (254 mm) areas that were longitudinally separated by 4.0 ft. (1.2 m) along the path. This was effectively the applied load, or the pressure due to a single wheel of the wheel pairs at each end of the tandem axle.

The spacing between the members, however, was less than 10 in. (254 mm), which resulted in overlap of 10 in (254 mm) by 10 in (254 mm) load areas, due to each wheel of the pair. This was resolved by symmetrically offsetting the load paths from the stringer centerlines. When the half load was assigned to both load paths simultaneously, the moving pressure areas formed two 10 in (254 mm) by 20 in (508 mm) load pads, spaced 4.0 ft. (1.2 m) apart in the longitudinal direction.

2.6 Results

Results of the grillage analyses including validation of the grillage model, and comparison of the V1 and V2 decks are discussed in this section. The grillage model was validated by comparing the grillage analysis results of the V1 deck with the 3D FEA results and static test measurements from the 2009 study on the V1 deck. In this previous study, a realistic 3D FEA model of the V1 deck was conducted in ABAQUS, a

commercially available FEA software, using continuum elements. The FEA model was validated against the experimental results and provided spatial distribution of the stresses throughout the deck. However, the grillage analysis of discrete interlocking members could not provide an assessment of local stresses in members and connections. Only nominal stresses could be estimated using strength of material calculations from the member forces at a section. Accordingly, the grillage model of the V1 deck was validated by comparing the global member responses among the 3D FEA measurements and grillage results that were not significantly influenced by local effects.

This primarily included the response of the stringers and transverse tubes. The local flexural response of the deck plate under the loads, or the local out-of-plan deformations at the tube-to-stringer connections were not captured by the grillage analysis, and were excluded from the comparison. Once the grillage model of the V1 deck was validated, the V2 deck was modeled accordingly. The grillage analysis results of the V2 deck were then compared with the V1 deck.

2.6.1 Validation of the Grillage Model

The grillage model was validated by comparing the grillage analysis results, the FEA results, and the LVDT and strain gauge measurements recorded during static testing of Specimen #1 of the V1 deck. For brevity of presentation in this document, the grillage analysis results are noted as “LARSA” and the FEA results are listed as “ABAQUS”. For plots that compare the vertical deck deflections, the displacements are shown on the ordinate, or y-axis. The abscissa, or x-axis, presents the distance from the deck end, from east to west (in the case of longitudinal paths) or the distance from the deck edge, from north to south (in the case of transverse paths). For the plots comparing the stress

responses, the stress values are shown on the x-axis, and the distance from the deck end or edge are shown on the y-axis. The paths, along which the distances were measured, are indicated in the key plan of the deck, and the locations of the LVDTs or strain gauges are shown on the key plan as open circles. The paths are also indicated on the key elevation.

The deflections of the V1 deck along stringers S5 and S3 are shown in Figure 15. In general, the grillage analysis results predicted less displacement than the FEA results. Along S3 the predicted displacements were closer to the actual displacements, however, along S5 the displacements adjacent to the load pads differed by about 50%. The measured displacements near the mid-span of the deck agreed well with the grillage analysis results at S3, and the FEA results at S5, though the FEA results were slightly larger. The measured displacements near the quarter spans were significantly less than the analysis results.

The vertical displacement of the deck along the transverse path on the soffit of T2 is shown in Figure 16. The FEA results, although larger, followed the same trend as the measured displacements at the soffit of S3 and S5. The vertical displacements at the soffit of the stringer (the locations of the LVDTs) should be almost the same as the vertical displacements at the soffit of the tube (the deflection path of the FEA and grillage analysis). The grillage analysis results were significantly lower than the FEA results and the measurements, particularly under S5 adjacent to the interior load pad. At S3, the displacement from the grillage analysis matched the measurement.

From Figure 16, it is evident that the grillage model was too stiff in the transverse direction; this was manifested by the relatively uniform vertical displacement of the grillage model. The increased stiffness could be due to a higher torsional stiffness of the

stringers and/or it could be due to a high flexural stiffness of the tubes and the deck in the transverse direction, as modeled in the grillage. The high transverse stiffness allowed more uniform sharing of the load among the stringers, resulting in an underestimation of the vertical deflection by the grillage analysis. The deflected shape of the stringers as determined by both the grillage analysis and the FEA was representative of simple spans, as assumed in Section 1.1. The lesser measured displacements at the quarter span suggest that the boundary or support conditions at the ends of the physical deck were not simple, but provided some rotational restraint. The transverse deck stiffness was adequately modeled in the FEA.

The stresses at the bottom soffit of the stringer and at the top of the deck plate along the centerline of S5 as obtained from the FEA, the grillage analysis, and the strain gauge measurements are compared in Figure 17. Along the soffit of the stringer, all results generally agreed well. Along the top of the deck plate, the grillage analysis results and the strain gauge measurements agreed very well. The FEA results, which exhibited the same general trend, predicted higher stresses. The FEA results showed a significant variation along the stress path, particularly on the deck plate at the intersection with the tubes, where the local stiffness changed significantly. This effect could not be modeled within a point representation of the stringer and tube intersection in the grillage model. Nonetheless, the global stress response predicted by the grillage model coincided extremely well with the measurements.

Similar stress responses of the deck along the centerline of S3 are presented in Figure 18, where the stresses from the FEA results, the grillage analysis results, and the strain gauge measurements are compared at the soffit of the stringer and at the top of the

deck plate All stress responses exhibited the same general trend, with the FEA results showing significant oscillations at and between the stringer-to-tube intersections. The grillage analysis results generally agreed well, and tended to constitute the lower bound to the FEA results. The strain gauge measurements at the soffit of S3 matched well with the grillage analysis and the FEA results, however, the measurements at the top of the deck plate were less than the analysis results.

The stresses along the soffit of the tube and at the top of the deck plate along the centerline of T2 as obtained from the FEA, the grillage analysis, and the strain gauge measurements are compared in Figure 19. At the soffit of the tube, all results agreed well near the deck edge, however, under the load pad, the grillage analysis results underestimated the deck response. The FEA results, however, agreed well with the strain gauge measurements. Along the top of the deck plate, the grillage analysis results generally agreed with the strain gauge measurements. The FEA results showed large oscillations as the deck plate spanned between the stringers, especially under the load pad. Again, this effect could not be modeled in the grillage analysis.

Overall, the grillage model was found to be too stiff, when compared to the LVDT and strain gauge measurements. The most accurate results of the grillage analysis were found along those members that coincided with stringers, specifically those members and stringers that were not under direct loading. In general, the grillage analysis results tended to indicate the lower bound to the FEA results.

2.6.2 Comparison of V1 and V2 Decks

The performance of the V1 and V2 decks was compared based on the grillage analysis results of the V1 and V2 decks. In the plots, these analysis results are labeled as

"V1" or "V2", followed by the location of the deck. These locations are identified by the grids (refer to Figure 26 for the grid layout) as S5, S3, T2, T1, or as "Deck Top". Paths along the deck top follow the deck plate above the centerline of the stringer or tube. The abscissa and ordinate axes are the same as on the plots in Section 2.6.1.

Figure 20 presents the V1 and V2 grillage analysis results for the vertical displacements along the grillage members that coincided with S5 and S3. The vertical displacements were reduced by 20% from the V1 deck to the V2 deck. However, the percent difference between the S5 and S3 deflections was about the same for the V1 and V2 decks.

The vertical displacements along the grillage members that coincided with T2 and T1 are shown in Figure 21. Again, the vertical deflection was reduced by 20% when comparing the V1 and V2 grillage analysis results. Similarly, the percent difference between the deflections along T1 and T2 of the V1 and V2 decks were about the same. As the grillage model was very similar between the V1 and V2 decks, similarity and consistency between the results is expected. The increased deck plate thickness and tube thickness increased the deck stiffness, however, the deck layout did not change, and the changes to the member cross sections were not extreme. As the deck response remains linear elastic, the consistent reduction in the vertical displacement is reasonable.

The stresses along the bottom soffit of the stringer and at the top of the deck plate along the centerline of S5 are presented in Figure 22. Along the bottom of S5, the stresses found in the V1 grillage analysis were reduced by 10% to 15% in the V2 grillage analysis. The largest stress reduction occurred between the interior and exterior load pad.

Along the top of the deck plate above the centerline of S5, there was a much larger stress reduction of about 35%.

The stresses at the bottom soffit of the tube and at the top of the deck plate along the centerline of T2 are shown in Figure 23. Along the bottom of T2 and along the deck plate above the tube centerline, the percent reduction in the stresses was variable. Large variations were found as the path moved between S2 and S4, and S7 and S9. As the path moved away from the stiffness provided by the cover plates towards the interior load pad, the percent difference between the V1 and V2 grillage analysis results did not remain consistent. In general, as found along the stringers, the stresses on the bottom soffit of the tube were not reduced as much as the stresses on the top of the deck plate, when comparing the V2 and V1 grillage analysis results.

Cross section changes greatly impact the stress response of the grillage model. The additional deck plate thickness influenced the cross section area, centroid location, and moment of inertia of all grillage members. These aspects of the cross section greatly influence the calculation of the grillage member forces. The changes to the grillage member cross section, though small enough to not cause variations in the grillage deflection, were enough to cause variation in the grillage forces.

3. FULL SCALE TESTS

3.1 Specimens

Two full size V2 deck specimens, identified as #1 and #2, were tested sequentially on the west dynamic test bed in the Fritz Laboratory at Lehigh University. As described in Section 1.1, the deck was supported on the longitudinal ends by a transom assembly and locked in place with Halfen channels and deck bolts. An extra wide transom assembly and deck bolts for interlocking the deck to the transoms were provided by the manufacturer.

The temporary bridge deck panels are typically fabricated by automatic robotic welding and are galvanized. Upon delivery of the V2 deck specimens, however, it was noted that specimens were not galvanized. Closer visual examination of the welds revealed significant spatters and poor weld profiles, which were inconsistent with robotic welding. It was later revealed that the welds for the V2 deck specimens were manually deposited. The effect of the weld quality on the performance of the deck specimens is discussed further in Section 5.2.

3.2 Test Load

As mentioned in Section 1.1 the test loads adhered to the fatigue loading provisions of the AASHTO LRFD BDS for orthotropic decks. The HL-93 live load for fatigue design consists of one design truck or the axles of the design truck, with a constant spacing of 30.0 ft. (9.1 m) between the 32.0 kip (142.3 kN) trailer axles. In the current 6th edition of the specification (AASHTO 2012), the design truck footprint is refined for design of orthotropic decks, where each trailer axle is presented in a tandem configuration, as shown in Figure 24. Each tandem axle consists of a pair of 16.0 kip

(71.2 kN) axles spaced 4.0 ft. (1.2 m) apart, with each axle comprising an adjacent pair of wheel loads at each end. The wheels are spaced 6.0 ft. (1.8 m) apart in the transverse direction. Each wheel load is distributed over a 10 in. (254 mm) by 10 in. (254 mm) tire contact area (AASHTO 2012).

In the field, the V1 deck has successfully survived for four to five years in rural areas and secondary roads that were lightly traveled and did not usually experience heavy truck traffic. Considering the improvements made between the V1 deck and the V2 deck (described in Section 1.2), it was estimated that the V2 deck would be capable of surviving seven years under the same circumstances. Under normal conditions, the average daily traffic of a road is physically limited to 20,000 vehicles per lane, and on rural interstate, the fraction of trucks in traffic is 0.20 (AASHTO 2012). For a temporary bridge deck in service for seven years, the total number of truck crossings is approximately 10 million ($20{,}000 * 0.20 * 365 * 7 = 10.2 * 10^6$), which falls under finite fatigue life design.

For finite fatigue life design, the design truck weight is reduced by a load factor of 0.75 (AASHTO 2012). The fatigue design truck was developed based on weigh-in-motion (WIM) studies of the gross vehicle weight (GVW) spectrum of trucks nationwide. It was developed assuming that (1) the bridge response to the truck weight is linear, thus the stress range induced at a detail by a truck crossing a bridge is proportional to the gross truck weight, and (2) the fatigue damage caused by all trucks crossing the bridge is the same as the fatigue damage produced by an equal number of fatigue design trucks. The fatigue design truck is therefore equivalent to trucks of all weights and configurations crossing a bridge, and it effectively produces the same fatigue damage as

all trucks in the spectrum. To account for the inertia imparted by dynamic loading, an impact multiplier of 15% is also required (AASHTO 2012).

The fatigue limit state load is three times the fatigue design load. Site specific WIM studies in the New York City area indicated the presence of trucks as heavy as 160 kip (710 kN) in the GVW spectrum. This weight is nearly three times the weight of the fatigue design truck. Field measurements of orthotropic decks in signature bridges suggest that the maximum stress range that occurs with sufficient frequency to cause fatigue damage in a deck corresponds to a load level of three times the fatigue truck loading. The maximum stresses experienced by the temporary deck in service may correspond to a higher load level due to distortion in the relatively thin and lightweight deck elements. Without field measurements, however, the load level cannot be established with certainty. Previous field measurements on bridges have demonstrated that the measured stress spectrums in various bridge members and elements do not exhibit one-to-one correspondence to the GVW spectrum due to various inherent non-linearity in the interactions and load transfers among the members, and in local distortion of the elements. In the absence of field measurements on decks in service, a load of 22 kip (98 kN) per wheel, or approximately three times the finite fatigue life design load, was assumed as an upper bound load level that occurs with sufficient frequency to cause fatigue damage in the deck. A load of 22 kip (98 kN) per wheel was used for static testing.

The transverse spacing of the wheels of the fatigue design truck is 6.0 ft. (1.8 m). Since the deck panel is 10 ft. (3.0 m) long and 6 ft. (1.8 m) wide, each deck panel could only accommodate one half of the axle during passage of the truck. As discussed in

Section 1.1, the most significant stresses found in the deck occurred under the tandem axle load. The tandem axle load on the deck is represented by two wheel load areas sized 10 in. (254 mm) by 20 in. (508 mm) separated longitudinally by 4.0 ft. (1.2 m). For the wheel load of 8.0 kip (35.6 kN) at each end of the tandem axle (described previously) the wheel load for the fatigue test of the orthotropic deck becomes 6.9 kip (30.7 kN) (8.0 * 0.75 * 1.15 = 6.9). For fatigue testing, this load was rounded to 7 kip (31 kN), and was planned to be applied over a maximum 10 million cycles, replicating the number of cycles the bridge deck is expected to experience during its service life.

Following 10 million load cycles under the finite fatigue life design load, if a specimen had not accumulated any noticeable fatigue damage, it was planned to be tested at the fatigue limit state load until failure. As was mentioned earlier, the fatigue limit state load for the specimens is three times the fatigue design load for finite life. This value was 20.7 kip (92.1 kN) (6.9 * 3 = 20.7) per wheel load, and it was rounded to 21 kip (93 kN) for testing.

3.3 Test Setup

3.3.1 Test Bed, Fixtures, and Arrangement

The test setup is shown in Figure 25. The specimens were oriented in the same direction for each test, and references to the cardinal directions refer to this orientation. The deck was placed such that the stringers ran from east to west, and the transverse tubes ran north to south. The stringers were labeled with S1 being the northern most stringer, and the labels ascended from north to south, with S10 being the southern most stringer. The tube T1 was on the east side of the deck, thus the tube labels increased to the west, with T2 being the east middle tube, and T3 being the west middle tube, and

finally T4 being the western most tube. The stringer-to-tube welds were located on the north face of the stringer webs. The test set up is such that the loading areas are on the eastern half of the deck, and situated along the longitudinal centerline.

The specimens were supported at each end on cut pieces of an extra wide transom assembly. In application, two or three deck panels would be supported on a transom assembly and discretely interlocked using Halfen channels and deck bolts. An extra wide transom assembly that could support two decks panels side-by-side was cut in half to create two supporting transoms at the ends of the specimen. Similar to the field installation, the specimens were interlocked with the transoms using deck bolts.

Both transoms were uniformly seated on buttressed steel pedestals that were anchored to the laboratory floor. The steel pedestals acted as rigid supports for the transoms. The bottom flanges of the transoms were clamped to the seat of the pedestal using C-clamps at discrete locations. Wooden bearing stiffeners were fitted in between the flanges of the transoms on both sides of the web under the Halfen channels. The wooden bearing stiffeners eliminated the possibility of local distortion of the transom flanges due to deck reaction.

The specimens were tested for the same load position as the V1 deck (discussed in Section 1.1), under a simulated pair of wheel loads spaced 4.0 ft. (1.2 m) apart in the longitudinal direction of the deck, corresponding to a tandem axle as discussed in the previous section. The wheel loads were located on the longitudinal center line of the deck, with the transverse center line of the tandem axle offset 30 in. (762 mm) towards east, with respect to the transverse center line of the deck. The placement resulted in one of the simulated wheel loads directly over the inside transverse tube T2, centered 6 in.

(152 mm) from the transverse center line of the deck, and the other simulated wheel load centered 6 in. (152 mm) from the east end of the deck. The load position was decided based on the study conducted in 2009 (discussed in Section 1.1), when the V1 deck was analyzed for several load positions to produce the most critical stresses. As per the AASHTO LRFD BDS, each wheel load was replicated by a 10 in. (254 mm) long and 20 in. (508 mm) wide rectangular loading pad, representing the tire contact area of a pair of adjacent wheels. Each loading pad consisted of four 2 in. (51 mm) thick steel plates with a $^{5}/_{8}$ in. (16 mm) thick high grade Nitrile rubber sheet glued to the underside of the bottom plate, which was in direct contact with the deck surface. Two actuators were used, each corresponding to one of the load pads.

The actuators were held in a fixed position, and reacted against a longitudinal beam directly above the longitudinal center line of the deck. The longitudinal beam was 10 ft. (3.0 m) long, and the mid-span of the beam coincided with the midpoint of the two actuators, or 30 in. (762 mm) from the east deck end. The longitudinal beam reacted against the two transverse beams of two portal frames. The transverse beams were both 11 ft. (3.4 m) long, and had an equal amount of overhang on either side of the deck. Each end of a transverse beam was connected to a floor column. The four floor columns were anchored to the laboratory floor, and were spaced 12.5 ft. (3.8 m) apart in the transverse direction of the deck, and 10 ft. (3.0 m) apart in the longitudinal direction of the deck. The two eastern floor columns were braced with lateral sway bracing.

3.3.2 Testing Equipment

The testing equipment was manufactured by Amlser and consisted of a variable stroke hydraulic pump (called a pulsator) to load the actuators. The actuators used for the

test program had a maximum dynamic capacity of 55 kip (245 kN) each. The two actuators, simulating the pair of wheel loads, were driven by a single pulsator. The actuators were interconnected and hydraulically synchronized to maintain an equal pressure of up to 110 psi (758 kPa), and load of up to 22 kip (98 kN).

3.3.3 Instrumentation

The specimens were instrumented with surface mounted, encapsulated metallic, bonded or welded electrical resistance strain gauges and displacement transducers. These were placed at critical locations to determine the response of the deck under test loads and to monitor the stresses during the fatigue tests. The gauge arrangements were decided based on the FEA results of the V1 deck, such that the longitudinal and transverse global and local behavior of the deck could be adequately captured.

Four types of strain gauges were used: (1) Vishay Micro Measurements LWK-06-W250B-350 uniaxial weldable gauges having 350Ω resistance and $^1/_4$ in. (6.4 mm) gauges length; (2) Vishay Micro Measurements CEA-06-UT-350 biaxial/tee rosette bondable gauges having 350Ω resistance and $^1/_4$ in. (6.4 mm) gauge length; (3) Tokyo Sokki Kenkyujo FLA-1-11 bondable gauges with 120Ω resistance and 0.04 in. (1.0 mm) gauge length; and (4) Tokyo Sokki Kenkyujo FRA-1-11 three-element rectangular rosette bondable gauges with 120Ω resistance and 0.04 in. (1.0 mm) gauge length. Lebow model # 3156-154-50k tension/compression fatigue rated canister load cells of ±50 kip (±222 kN) capacity were used to measure the applied load, and Macro Sensors model GHSD 750-500 linear voltage differential transformers (LVDT) with ±0.5 in. (±13 mm) displacement range were used to measure the deck displacements.

Due to the symmetry in the general global geometry and loading about the longitudinal centerline of the deck, and the application of the load over one half of the deck span, the strain gauges and LVDTs were concentrated over a quadrant of the deck. The intermittent fillet welds have an asymmetric layout. Despite this, the instrumentation arrangement was sufficient to provide the critical response of the entire deck. The instrumentation of each specimen is elaborated further in the following:

Specimen #1

The first specimen was extensively instrumented to capture the global and local behavior of the deck, and to validate the grillage analysis results. The instrument arrangement was kept similar to Specimen #1 of the V1 deck to compare the performance of the V1 and V2 decks. The instrumentation plans for Specimen #1 are shown in Figures 26−32. In total, 39 uniaxial $^1/_4$ in. (6.4 mm) gauges, 22 biaxial $^1/_4$ in. (6.4 mm) gauges, 14 uniaxial 0.04 in. (1.0 mm) gauges, and 4 three-element 0.04 in. (1.0 mm) rosettes were installed on the specimen. In addition, two load cells and nine LVDTs were provided. The load cells were placed between the actuators and the load pads, and were retained for both the static and the fatigue testing. The LVDTs were only used to measure deck displacements during the static tests.

The strain gauges and the LVDTs were distributed on a grid of five transverse and eight longitudinal locations, with the exception of two strain gauges, which were located on stringer S2. The gauges were located on a grid pattern for investigating the response of the deck at specific sections. The longitudinal sections were: (1) Section 1, through the mid width of the cover plate between stringers S1 and S2; (2) Section 2, midway between stringers S2 and S3; (3) Section 3, along the centerline of stringer S3; (4) Section 4,

midway between stringers S3 and S4; (5) Section 5, along the centerline of stringer S4; (6) Section 6, midway between stringers S4 and S5; (7) Section 7, along the centerline of stringer S5; and (8) Section 8, midway between stringers S5 and S6, or, along the longitudinal center line of the deck. The transverse sections were: (1) Section A, along the transverse center line of the deck, midway between the inner tubes T2 and T3; (2) Section B, 6 in. (152 mm) offset from Section A, along the transverse center line of tube T2, through the west (inner) loading pad; (3) Section C, 18 in. (458 mm) offset from the center line, along the transverse centerline of tube T1; (4) Section D, 36 in.(916 mm) offset from the center line, or 24 in. (610 mm) from the east end of the deck; and (5) Section E, 5 in. (127 mm) from the east end of the deck, through the east (outer) loading pad.

The gauge layouts on the top surface of the deck plate and on the deck underside are shown in Figure 26 and Figure 27 respectively. The grid pattern described above is shown on all figures that use the grid layout to identify gauge locations. Gauge names were kept the same between the V1 and V2 decks, but some gauges were removed during the instrumentation of the V2 deck. As a result, some of the gauge names are incongruous. For instance, gauge T1_4 was placed underside of the deck, though gauges T1_1, T1_2, and T1_3 were not included.

The gauge names indicate the general gauge location. Gauges labeled “TDP” and “BDP” were placed on the top and bottom of the deck plate, respectively. For biaxial gauges, this label was followed by an “L” or a “T”, to indicate the gauge orientation as longitudinal or transverse. The underside of the deck also had gauges labeled “BCP”, which indicate that the gauge was on the bottom of the cover plate. Gauges placed in line

with stringers started with the stringer label, and were be followed by a “T” to indicate placement on the top of the deck plate, or a “B” to indicate placement on the bottom of the stringer flange.

Along the center lines of the stringers, uniaxial strain gauges with $^1/_4$ in. (6.4 mm) gauge length were provided on the top surface of the deck plate and on the underside of the stringers, oriented in the longitudinal direction of the deck. Along sections 3, 5, and 7, uniaxial strain gauges were provided at the intersection of sections A, B, and D. These gauges were provided to capture the global longitudinal bending response. At Section 1, uniaxial gauges were provided at the intersections of sections A, B, and D, on the underside of the cover plate and on the top surface of the deck plate. Additionally, at Section E, uniaxial $^1/_4$ in. (6.4 mm) strain gauges were provided on the top of the deck plate and on the underside of stringer S2 oriented in the longitudinal direction. These two gauges were the exceptions to the grid arrangement.

On the deck plate, biaxial strain gauges of $^1/_4$ in. (6.4 mm) gauge length were placed back-to-back on the top and bottom surfaces, in between the stringers, along sections 2, 4, 6, and 8. These gauges were placed at the intersections with sections A and E, and were provided to capture the transverse bending response of the deck plate as it spans between the stringers, and to capture the longitudinal bending response of the deck plate in the primary span direction. At Section B, biaxial gauges were placed in between the stringers, along Sections 2, 4, 6, and 8, only on the top surface of the deck plate, as the bottom surface of the deck plate was inaccessible due to the transverse tube T2. At Section D, a uniaxial strain gauge of $^1/_4$ in. (6.4 mm) gauge length was installed at the intersection with Section 8, aligned in the longitudinal direction of the deck. At Section

E, biaxial gauges were placed in between the stringers, along sections 2, 4, 6, and 8, back-to-back on the top and bottom surface of the deck plate.

On transverse tubes T1 and T2, uniaxial strain gauges of $^1/_4$ in. (6.4 mm) gauge length were installed on the bottom soffit, oriented in the transverse direction of the deck, or along the tubes. At Section B (along T2), the gauges were placed at B2, B4, B6, and B8. At Section C (along T1), one gauge was installed at C8. These gauges were provided to capture the transverse bending response.

At the termination of the intermittent fillet welds between the top flange and stringer S5, four uniaxial strain gauges of 0.04 in. (1.0 mm) gauge length were installed. Figure 28 shows these gauges, with a closer view shown in Figure 29. The gauges were aligned with along the longitudinal axis of the welds, and were placed $^5/_{32}$ in (4.0 mm) ahead of the weld toe. From the testing of the V1 deck, it was expected that the stress at these gauges would be compressive, however, due to high tensile residual stresses, fatigue cracking can initiate in an area under compressive stress. Gauges were placed at the stringer-to-deck welds to perceive the possibility of fatigue cracking at this location.

The study of the V1 deck revealed that the connections between the stringers and the tubes were the most susceptible to fatigue cracking, due out of plane distortion of the web gap subject to the downward displacement of the tubes under wheel loads. The tubes were connected to the stringers with one sided intermittent fillet welds. In the laboratory testing, fatigue cracks developed in the tube wall of the S6-T1 connection, from the weld toe near the lower weld termination. Fatigue cracks also developed at the intersections of S5 with T1 and T2, from the weld root of the lower weld termination. Accordingly, selected stringer-to-tube connections in the V2 deck were densely instrumented with

strain gauges of 0.04 in. (1.0 mm) gauge length. Six uniaxial gauges and four three-element rectangular rosettes were installed as seen in Figure 30, which shows the connection between S4 and T2, and Figure 31, which shows the connection between S5 and T2.

At the S4-T2 connection, all gauges were placed back-to-back on the stringer web and were placed on the west side of the tube, towards the deck mid-span, or between T2 and T3. The two rosettes were oriented such that one of the orthogonal arms lay in the longitudinal direction of the deck. These gauges were placed such that the rosette on the welded side was $^{3}/_{32}$ in. (1.6 mm) radially from the weld toe termination. A uniaxial gauge was aligned with the 45˚ rosette arm and placed $^{3}/_{16}$ in. (2.4 mm) from the rosette. Another uniaxial gauge was aligned with the vertical arm of the rosette gauge, and was placed as close to the flange-to-web fillet termination as possible.

The remaining two rosettes and the two uniaxial strain gauges were installed adjacent to the stringer S5 and tube T2 connection, as shown in Figure 31. All gauges were placed on the west side of the tube, towards the deck mid-span. One rosette was placed on the web of S5, near the bottom of the S5-to-T2 weld. The rosette was oriented such that one of the orthogonal arms was aligned longitudinally. The rosette was placed $^{3}/_{32}$ in. (2.4 mm) radially from the bottom weld toe termination. Aligned with the longitudinal rosette gauge, a uniaxial gauge was placed $^{3}/_{16}$ in. (4.8 mm) from the weld toe. The other rosette was placed on T2, in line with the rosette on the web of S5, oriented such that one of the orthogonal arms was aligned transversely. The rosette was placed $^{1}/_{8}$ in. (3.2 mm) from the weld toe. The second uniaxial gauge was aligned with the transverse rosette arm, and was placed $^{9}/_{32}$ in. (7.1 mm) from the rosette.

The layout of the gauges at the stringer-to-tube connection was chosen in order to calculate the hot spot stress at the welded connection. The structural stress at the hot spot includes the stress effects of a structural detail, and excludes the stress concentrations due to the local weld profile. Therefore, the non-linear stress caused by the weld toe, which could approach infinity, is excluded from the structural stress. This method was used because of the complicated geometry at the connection, as there is no clearly defined nominal stress (IIW 2005). To calculate the hot spot stress, the strain measurements from two gauges are used as reference points in a linear extrapolation. The reference points are placed in line at specified distances from the weld toe, the closest at a distance of 0.4*t*, the farthest at 1.0*t*, where *t* is the thickness of the stringer web or the tube (IIW 2005). At the connections, the rosette gauge was placed 0.4*t* from the weld toe ($^{3}/_{32}$ in. (2.4 mm) on the stringer web, $^{1}/_{8}$ in. (3.2 mm) on the tube), and a uniaxial gauge was placed at 1.0*t* from the weld toe ($^{3}/_{16}$ in. (4.8 mm) on the stringer web, $^{13}/_{32}$ in. (10.3 mm) on the tube). The hot spot stresses at the stringer-to-tube connections are discussed further in Section 5.3.1.

Nine LVDTs were used during static testing of Specimen #1. As shown in Figure 32, the LVDTs were placed on the underside of the deck, at the intersection of transverse section A, B, and E and longitudinal sections 1, 3, and 5.

Specimen #2

Compared to Specimen #1, Specimen #2 was gauged sparsely to compare the response of the decks, and to monitor the fatigue test. The instrumentation plans for Specimen #2 are shown in Figure 30, and Figures 32–37. Total eight uniaxial $^{1}/_{4}$ in. (6.4 mm) gauges, 10 uniaxial 0.04 in. (1.0 mm) gauges, and six 0.04 in. (1.0 mm) rectangular

rosettes, two load cells, and nine LVDTs were installed on the deck. The LVDTs were in place for the static tests only.

The gauge layout on the top of the deck plate and the underside of the deck panel are shown in Figure 33 and Figure 34, respectively.

Uniaxial strain gauges of $^1/_4$ in. (6.4 mm) gauge length were provided on the top of the deck plate and on the underside of the stringers at section locations 3B and 5B, aligned in the longitudinal direction of the deck. At section location 5E, one uniaxial strain gauge was placed on the underside of stringer S4. These gauges were placed at common locations with Specimen #1.

On tubes T1 and T2, uniaxial strain gauges of $^1/_4$ in. (6.4 mm) gauge length were installed on the soffit at section locations B8 and C8, respectively, oriented parallel to the tube axis or the transverse direction of the deck. These gauges were also placed at common locations with Specimen #1.

The S4-T2 connection in Specimen #2 was gauged similarly to Specimen #1. Shown in Figure 30, two 0.04 in (1.0 mm) rectangular rosettes and four uniaxial two 0.04 in (1.0 mm) gauges were placed back-to-back on the web, on the west weld, closest to the deck mid-span. In Specimen #1, the strain gauges were placed at the S4-T2 connection before realizing that, due to the deck orientation, the S4-T2 connection was not the most critical. The deck was oriented such that the welds at the S4-T2 connection face away from the wheel load. The resulting web distortion causes the stress surrounding the weld to be compressive, however, the most critical stresses would occur when the web distortion causes the stress surrounding the weld to be tensile. This occurs at the S7-T2 connection.

At the S7-T2 connection, the welds face the wheel load, and the resulting distortion caused the stress around the weld to be tensile. Shown in Figure 35, the strain gauge arrangement was the same as at the S4-T2 connection, with two 0.04 in (1.0 mm) rectangular rosettes and four uniaxial two 0.04 in (1.0 mm) gauges arranged back-to-back on the stringer web.

The S6-T2 connection in Specimen #2, shown in Figure 36, was gauged similarly to the S5-T2 connection in Specimen #1, with two 0.04 in (1.0 mm) rectangular rosettes and two uniaxial 0.04 in (1.0 mm) gauges. As with the S4-T2 connection, in Specimen #1 the S5-T2 connection was gauged before realizing that, due to the deck placement, it was not the most critical connection. At the S6-T2 connection, the welded side faced the wheel load, and the stress surrounding the weld was tensile.

The S9-T2 connection was gauged similarly to the north side of the stringer web of S4-T2 and S7-T2. Due to the presence of the cover plate, gauging both sides of the web of S9 was impossible, and as shown in Figure 37, only the north side of the web was gauged. The S9-T2 connection was gauged due to the manifestation of cracks at this location during the fatigue test of Specimen #1.

Similar to Specimen #1, nine LVDTs were used during testing of Specimen #2, as shown in Figure 32. The LVDTs were placed at the same section locations (intersections of sections A, B, and E, and sections 1, 3, and 5).

3.3.4 Data Acquisition

Data were collected using Campbell Scientific programmable digital data logger CR9000. For Specimen #1, total 116 channels of data (105 strain gauge channels, nine LVDT channels, and two load cell channels) were collected using eight 9050 analog

cards. Each analog card could accommodate 14 channels. For Specimen #2, 52 channels of data (41 strain gauge channels, nine LVDT channels, and two load cell channels) were collected, using nine 9052DC digital filter cards. Each digital card accommodated six channels. The digital filter cards incorporated a programmable, real time, finite impulse response (FIR) low pass filter. The band pass frequency for the filters was set at 20 Hz for a test frequency of 4.3 Hz. Data were sampled at 50 Hz for the static and fatigue tests. To reduce noise and spurious signals in the collected data, the settling time was set at 200 μsecs and the integration time was set at 200 μsecs. The settling time is the time taken for the input or output channel to settle to its new value when a change in signal occurs. The integration time is the time over which the input signal is averaged to reduce the noise caused due to random fluctuations in the signal.

The strain gauges used were piezoelectric, therefore, as the strain gauges deformed the electrical resistance of the material changed proportionally. For strain gauges attached to the specimen, the deformation of the gauge was equivalent to the deck deformation, and the strain at that location could be determined from the change in the gauge electrical resistance. During the initial static tests of Specimen #1, the data logger program used a measurement range of ±200 mV for the strain gauges. For analog to digital (A/D) conversion, the sampled voltage is resolved to approximately one part in the full scale range, or one part in 62,500 (for example, with a measurement range of ±200 mV, the resolution was 400 mV/62,500 = 6.4 μV). Within the data logger program, the voltage from the gauge is converted into strain using the proportional relationship between the electrical resistance and the deformation. For data collection from uniaxial

and biaxial gauges, the strain was converted into stress using the material modulus of elasticity. Data collected from the rosettes remained as strain.

Prior to the final static test of Specimen #1, it was noticed that the strain gauge readings would not zero. Even under complete unloading, the gauge stress values would be as high as 2 ksi (14 MPa). The inability to zero the gauges would influence the accuracy of the gauge stress readings when the specimen is loaded. This problem was mitigated by narrowing the program's measurement range. By using a measurement range of ±50 mV, the resolution of the voltage measurement was refined by a factor of four (100 mV/62,500 = 1.6 μV). With a finer resolution, the program was able to measure the voltage more precisely, and zero the gauges. However, should the voltage measured by a strain gauge exceed ±50 mV, the data logger would be unable to read the strain gauge. To check this, a static test was conducted up to the maximum load of 22 kip (98 kN). During the final static test of Specimen #1, none of the gauge readings exceeded the measurement range, indicating that the change to the measurement range was suitable for static and fatigue testing.

During static testing, data were collected at discrete load levels (described in Section 3.4). At each load level, the program would record the average stress reading for one second (or, the average over 50 samples), over 30 seconds, resulting in 30 records, total.For fatigue testing, some data were collected continuously by the data logger, andsome data were collected by the user at inspection times only. In addition to the mechanical cycle counter on the pulsator (described in Section 3.5.1), the data logger program contained a built-in rainflow counting algorithm. Every 15 minutes, the program would automatically record the total cycle count, based on the signal amplitude in

gaugeS5_B3. The minimum and maximum response of the channels over 15 minutes was also recorded by the data logger program every 15 minutes.

At every inspection, the user would collect three sets of data. For all channels, a sample of the data would be collected in real time for five minutes, or 6000 records. The minimum and maximum at each channel over 30 seconds would also be recorded for five minutes, or 10 records. In the data logger program, a sub-routine was developed to calculate the principle stresses at the rosette gauges. The sub-program was used with data collection, allowing the program to record the strains and the corresponding principle stresses in the rosettes, as well as the stresses in the uniaxial gauges at the stringer-to-tube connections. This data was sampled in real time for 50 seconds or 1,000 records. Throughout the fatigue test, an electronic log sheet was used to monitor the stress in specific gauges. At each inspection, the date and time of inspection, the corresponding cycle count, and the minimum and maximum load readings from the Amsler pulsator and the two load cells were recorded. The minimum and maximum stress at specific gauges, described in sections 3.5.2 and 3.5.3, were also recorded. Tables that continuously sampled the data but did not save were used for this. The tables showed the gauge stress readings in real time, both live and as the minimum and maximum over 30 seconds. The data on the electronic log were also recorded on a paper log at each inspection, in the event of digital data loss.

3.4 Static Tests

3.4.1 General Test Procedure

Prior to fatigue testing, all specimens were tested at a slow loading rate or static loading to determine the overall deck response, the base line stress state in the deck, and the dynamic load limits (and stress limits at the control gauges) for the fatigue tests.

The static tests were conducted in an up-down fashion by slowly increasing the load at each actuator from zero to the maximum, followed by complete unloading. The maximum load of the tests was 22 kip (98 kN), the fatigue limit state load per load pad representing a pair of adjacent wheels, as described in Section 3.2. The loads were briefly held at discrete levels (described in the following section) to collect data from all instruments at the particular load level. To shakedown residual stresses and to verify repeatability, the static tests were repeated at least four times for each specimen, or until the residual strains at the gauges were negligible after unloading.

The loads were measured by the load cells located between the actuators and the loading pads. The loads were also indicated by the dial gauge on the Amsler pulsator, which was verified and correlated with the load cell measurements. During the static tests, the displacement of the deck was measured at specific locations by LVDTs (see Figure 32), which were removed prior to fatigue testing.

3.4.2 Static Testing of Specimen #1

Static testing of Specimen #1 was conducted on March 22, 2013. Data were collected at the 4, 7, 10, 16, and 22 kip (18, 31, 44, 71, 98 kN) loads. The test was repeated four times. Another test was performed where data were collected at 2 and 9 kip

(9 and 40 kN) to determine the stress limits at the gauges to be monitored during the fatigue test.

Following the changes to the testing machine set up (as described in Section 3.5.2), additional static tests were conducted up to 22 kip (10 kN), at the same load steps described previously. The fifth test was performed on April 24th, following the first change to the Amsler machine set-up. The sixth and seventh tests were performed on April 26th, following the second change to the Amsler machine set-up. The eighth test was performed on August 29th, following the change to the measurement range of the data logger program described in Section 3.3.4.

3.4.3 Static Testing of Specimen #2

Static testing of Specimen #2 was performed on June 17, 2013 for the same protocol as Specimen #1. The test was repeated four times to a maximum load of 22 kip (10 kN). Data were collected at 4, 7, 10, 16, and 22 kip (18, 31, 44, 71, 98 kN) loads.

3.5 Fatigue Tests

3.5.1 General Test Procedure

The fatigue tests were conducted under a constant amplitude sinusoidal pulsating load, applied at 4.3 Hz, or 260 cycles per minute. The tests were load controlled and monitored by the minimum and maximum load as indicated by the dial gauge on the Amsler machine and confirmed by the load cell readings. Fatigue testing was conducted at minimum and maximum load levels of 2 and 9 kip (9 and 40 kN), respectively, resulting in a load range of 7 kip (31 kN) at each actuator. Testing was conducted 24 hours a day, with inspections taking place every four hours between 7AM and 11PM.

Stress measurements at critical gauges were also monitored at each inspection. At each inspection, the specimens were inspected for any fatigue cracking, with the aid of a 10x magnifying glass and/or dye-penetrant testing as needed. A mechanical counter on the Amsler machine showed the number of applied load cycles. The load, the stress measurements, and the number of load cycles were recorded during each inspection. The fatigue tests were interrupted upon detection of a fatigue crack, and the location and length of the crack, and the number of cycles at time of detection, were recorded. The growth of these cracks was recorded at subsequent inspections.

3.5.2 Fatigue Testing of Specimen #1

Fatigue testing of Specimen #1 was initiated on April 22, 2013. Strain gauges S5_B3, S5_B4, T2_4 and T1_4 were monitored at every inspection, in addition to the principle stresses S4_T2N_SP and S4_T2N_SQ, and the principle stress angle, S4_T2N_HP. From the static tests, the predicted load range at S5_B3 was 1.90 to 7.90 ksi (13.10 to 54.47 MPa), at S5_B4 was 1.60 to 6.90 ksi (11.03 to 47.57 MPa), at T2_4 was 2.10 to 9.50 ksi (14.48 to 65.50 MPa), and at T1_4 was 2.10 to 9.10 ksi (14.48 to 62.74 MPa). In general, the minimum and maximum stress at these gauges would increase slightly as the test continued, however, the range would remain consistent. For principle stresses, the predicted load range was -2.30 to -0.50 ksi (-15.86 to -3.45 MPa) for S4_T2N_SP, and -17.00 to -3.50 (-117.21 to -24.13 MPa) for S4_T2N_SQ; the principle stress angle, S4_T2N_HP, was predicted to have a maximum of 34.70˚ and a minimum of 35.90˚. During the fatigue test, the recorded values did not coincide with the predicted values.

Initially, the test was controlled by two Amsler machines coupled together in master-slave configuration. During this period, significant difficulty was experienced in maintaining the target loads for the test. The load levels would climb between inspections, i.e the mean load would increase, without application of the static load component. As a result, the maximum load would increase and trip the upper load limit set on the Amsler machine, shutting down the test. Suspecting that the deck was too flexible for two machines to hold the test loads, it was decided to decouple the Amsler machines and use one pulsator for the test instead. The test was restarted on April 24, 2013 using the east Amsler machine (earlier set up as the slave), however, the symptoms persisted and the fatigue test was suspended. The pulsator was then exchanged for the master Amsler machine (to the west) on April 26, and the fatigue test was resumed on May 1, 2013. The problem was solved with this change, as the pulsator was able to stabilize the target constant amplitude loading for the fatigue test.

On May 23, at approximately 8.0 million cycles, the fatigue test was halted as cracks were discovered at several stringer-to-tube connections. These cracks are described in Section 5.1.1, and shown in Figures 60–64.

Since the cracks were of small length that did not affect the structural integrity of the specimen, and the applied load cycles were close to the test target, it was decided to continue fatigue testing of the specimen. The fatigue test was resumed on May 30, and continued for another six days, when the target 10 million cycles at the test load level was reached. During this time the inspection of the specimen continued at every four hours between 7AM and 11PM, however no changes to the number of cracks or length of the cracks were observed. The fatigue test of Specimen #1 was terminated on June 5, 2013.

3.5.3 Fatigue Testing of Specimen #2

The fatigue testing of Specimen #2 began on June 24, 2013, using the master Amsler machine. At every inspection the load levels and the strain gauges S5_B3, S3_B3, T2_4 and T1_4 were monitored and recorded. Principle stresses S7_T2N_SP, S7_T2N_SQ, and the principle stress angle, S7_T2N_HP, were also monitored and recorded. From the static tests, the predicted load range at S5_B3 was 1.75 to 8.15 ksi (12.07 to 56.19 MPa), at S3_B3 was 0.9 to 4.40 ksi (6.21 to 30.34 MPa), at T2_4 was 2.10 to 10.00 ksi (14.48 to 68.95 MPa), and at T1_4 was 2.00 to 9.30 ksi (13.79 to 64.12 MPa). In general, the minimum and maximum stress at these gauges would increase slightly as the test continued, however, the range would remain consistent. For principle stresses, the predicted load range was 2.80 to 13.50 ksi (19.31 to 93.08 MPa) for S7_T2N_SP, and 1.00 to 4.60 (6.89 to 31.72 MPa) for S7_T2N_SQ; the principle stress angle, S7_T2N_HP, was predicted to have a maximum of -53.20˚ and a minimum of -56.70˚. During the fatigue test, the recorded values did not coincide with the predicted values.

The fatigue test continued without pause until July 18, or at approximately 9.0 million cycles, when cracks were discovered at several stringer-to-tube connections. These cracks are described in Section 5.1.2, and shown in Figures Figure 65–Figure 68.

Since the cracks were of small length that did not affect the structural integrity of the specimen, and the applied load cycles were close to the test target, it was decided to continue fatigue testing of the Specimen. The fatigue test resumed on July 22, and continued for another three days, when the target 10 million cycles at the test load level was reached on July 25. During this time the inspection of the specimen continued at

every four hours between 7AM and 11PM. During this time, additional cracking was observed at two stringer-to-tube connections. These cracks are described in Section 5.1.2.

4. RESULTS OF STATIC TEST

The global and local response of the V2 deck under the fatigue limit state load of 22 kips (98 kN) applied at a static loading rate are presented in this section. These static tests were conducted prior to fatigue testing, and the results were analyzed and compared with the analytical predictions. The global response of the deck is discussed with respect to the response of the stringers and the tubes. The local responses under the wheel load are discussed with respect to the response of the deck plate and the stringer-to-tube connections. Measurements at sensors were tabulated and plotted against the load and to determine if the stress response was linear elastic, and if the tests were repeatable.

4.1 Introduction

Static tests were conducted on Specimen #1 between March 22 and April 28, 2013. For Specimen #1, 53 uniaxial strain gauges, 22 biaxial strain gauges, 4 rectangular three-element rosette gauges, and 9 LVDTs were installed on the specimen. In addition, two load cells were used to capture the load applied by the actuators. All tests were conducted within the nominal elastic range of the material. Static testing of Specimen #2 was conducted on June 24, 2013. Specimen #2 was gauged using 18 uniaxial strain gauges, 6 rectangular three-element rosettes gauges, and 9 LVDTs, in addition to the 2 load cells installed at the actuators. The strains measured at the gauges were converted to stresses by the universally accepted modulus of elasticity of 29,000 ksi (200,000 MPa), and Poisson's ratio of 0.3, for steel.

The static test results are presented as plots of individual sensor measurement against the load, or the measurement at sensors along a deck section. In plots of individual senor measurement, the measured quantities are presented on the ordinate, or

y-axis, and on the abscissa, or x-axis, is the load level for individual gauges. In plots of measurements along a deck section, the measured quantities are again presented on the y-axis, and the x-axis shows the distance from the deck end. For plots along sections 1 through 8, the distance is presented from east to west, and for plots along sections A through E, the distance is presented from north to south. The paths, along which the distances were measured, are indicated in the key plan of the deck, as well as the LVDT or strain gauge locations. In the stress plots, the paths are also indicated on the key elevation. The downward displacements are presented as negative, and tensile stresses are presented as positive.

On some plots, the grillage analysis results are included. The grillage analysis results are indicated in the legend as "LARSA", the program used for the grillage analysis. For longitudinal paths, the grillage results are labeled with the stringer or with "CP", an abbreviation of cover plate. In the transverse direction, the grillage results are labeled with the tube, or with the section label.

4.2 Global Response of the V2 Deck

Nine LVDTs were employed on specimens #1 and #2 in coinciding locations, at A-1, A-3, A-7, B-1, B-3, B-7, and D-1, D-3, D-7 (refer to Figure 32 for LVDT layout). The global response of the stringers was assessed by the measurements at the sensors installed on the underside and on top of the stringers. Uniaxial strain gauges were installed at sections A, B, D and E (shown in Figure 26 and Figure 27) aligned with the stringers, and placed at the stringer midline on the bottom flange and the deck plate.

The global response of the tubes was assessed by uniaxial strain gauges installed on the underside of the tube, and/or on the deck plate directly above the tubes, between

the stringers, at sections 2, 4, 6, and 8. The strain gauges were installed at the center of the underside of the tube.

4.2.1 Response of Stringers and Tubes

Figure 38 shows the measurements at CP_DISPL_1 against the applied load for Specimen #1. During the first static test, there was some non-linearity in the results, which can be attributed to residual stresses from the deck welds. Multiple static tests serve to shakedown the residual stresses, and as shown, the displacement was linear following the first static test. The results of multiple static tests of the same specimen show the results were linear and repeatable.

The displacement at S3_DISPL_2 against the applied load is plotted in Figure 39. The results of Specimen #1 and Specimen #2 are shown. In plots that present static tests results from two specimens, the measurements of the fourth static test were used. This was done to prevent the residual deck stresses from influencing the results. The measurements of Specimen #1 and Specimen #2 coincide well; the results are consistently similar at different loads, and the measurements for both specimens were linear. The corresponding displacement from the grillage analysis is also shown. The grillage analysis results at S3_DISPL_2 replicated the measurements at the sensors well. This may be attributed to the distance of the LVDT from the load pad. The static test results of the two specimens show the results were linear and repeatable for multiple specimens.

The vertical displacements of the deck soffit along sections 1 (underside of the cover plate, between stringers S1 and S2), 3 (underside of S3), and 7 (underside of S5) for Specimen #1 and #2 are plotted in Figure 40. The LVDTs were centered under the

stringer bottom flange and under the cover plate, at sections A, B, and D. The displacement from the grillage analysis results along of stringers S5 and S3 are shown as a solid line, where members existed in the grillage model and results were available. No member existed in the grillage model along Section 1, the centerline of the cover plate. The displacements at this section were obtained at the intersections of the transverse grillage members with Section 1, and are therefore presented by discrete symbols

Figure 41 shows the measurements taken at the LVDTs along transverse sections A, B, and D for the two specimens. As in Figure 40, no grillage members correspond to Section A or Section D, and the displacements at these sections were obtained at the intersections of the transverse grillage members with the sections, thus, the results are presented with discrete symbols.

The largest deflections occurred underneath the interior, or the west, load pad (LVDT S5_DISPL_3) at 6 in. (152 mm) from the transverse centerline of the deck. The deflection decreased away from the interior loading pad, with the LVDT at Section A having the second largest deflection, and the deflection at Section D having the smallest deflection, on S5. This pattern was repeated at the two other longitudinal sections, shown in Figure 40, with S3, being closer to the load pads, having larger deflections than Section 1.

Compared to the measurements, the grillage model underestimated the deflection along S5 and overestimated the deflection along Section 1. However, the grillage prediction corresponded well with the displacements along S3. From this, it can be inferred that the grillage model was too stiff in the center of the deck, and too flexible at the deck edges. Also noticeable is the differences in slope between the LVDT and the

grillage deflections. Along S5 in Figure 40, the LVDTs show a sharp dip directly beneath the load pad (at LVDT S5_DISP_2) that was not present in the deflection of the grillage model. This could be the due to localized effects as a result of the loading pad, which the global grillage model would be unable to replicate. The large dip in the measurements can also be seen in Figure 41. As discussed previously, the grillage model appears to be too stiff in the middle of the deck, and too flexible at the edges.

For both specimens, the longitudinal stresses measured by strain gauges along Section 7, on the underside of S5 and on the deck plate above S5, are plotted in Figure 42. Tensile stresses were measured on the bottom flange of the stringer, and compressive stresses were measured on the top of the deck plate, in both specimens. Similar to the deck deflection, the maximum longitudinal stress in the stringer occurred at S5_B3, located at Section B, directly under the interior, or the west, load pad. At S5_B1, directly under the exterior, or the east, load pad, the stress is considerably less than the stress under the interior load pad. Due to the proximity of the transom, most of the load at this location is directly transferred to the support, resulting in a smaller stress response at this section.

The longitudinal stresses measured by strain gauges along Section 7, on the underside of S3 and on the deck plate above S3, for both specimens, are plotted in Figure 43. As with S5, tensile stresses were measured on the bottom flange of the stringer, and compressive stresses were measured on the top of the deck plate. Additionally, the largest stresses were found at Section B. Further from the load pad, it appears that the influence of the load pad is less, and the deck stresses appear to vary less drastically.

The transverse stresses in both specimens, measured by strain gauges along Section B, on the underside of T2 and on the deck plate above T2, are plotted in Figure 44. About the deck centerline, tensile stresses were measured on the bottom of the tube, and compressive stresses were measured on the top of the deck plate. However, close to the deck edge, the opposite occurs. At T2_1, located on the bottom of T2 at Section 2, the compressive stress most likely occurs due to the curvature of the deck. In Figure 41, the grillage displacement along T2 shows a slight negative curvature near the edges of the deck, before the curvature becomes positive at the deck center. If this is true for the deck deflection, it would result in compressive stress at sensor T2_1. Along the top of the deck plate, TDP_T8, located very close to the edge of the load pad, and shows a large compressive stress as it deflects underneath the pad. The compressive stress reverses at TDP_T7, which recorded tensile stresses. This large variation can be attributed to the local effects of the load pad on the deck plate.

The results of the grillage analysis were also plotted in Figures 42 through 44, calculated from the moment along the member that coincides with the section. In Figure 42, the grillage stress path appears to follow the same pattern as the deck stresses, although the results along the underside of the stringer appear to be more accurate than those along the top. The largest discrepancies occur along the top of the stringer, at the gauges directly under the interior load pad. Most likely, the differences are the result of local stresses surrounding the load pad, which the grillage analysis was unable to duplicate. Along the bottom of the stringer, the stress predicted by the grillage was consistently less than that found on the deck, therefore along S5 the grillage was made too stiff.

Figure 43 shows that without the proximity of the load pad influencing the sensor measurement, the grillage model was able to better predict the stress response of the stringer. The grillage was able to approximate the stresses well along the top of the deck plate, and adequately along the bottom. At S3, the stress predicted by the grillage exceeded the stress found in the deck, indicating the grillage was made too flexible.

The grillage model is unable to reproduce localized stresses, therefore the stresses calculated along the top of Section B in Figure 44 do not accurately reflected those found on the specimen. Similarly, along the bottom of Section B, the grillage stresses are consistently less than those measured on the deck. This is mostly likely a result of the localized effects of the load pad, in addition to the grillage model being too stiff at the mid-span.

4.3 Response of Deck Plate

The longitudinal stresses on the top and bottom of the deck plate, measured along Section 8, are plotted in Figure 45. Due to the presence of T2, a gauge could not be installed on the bottom of the deck plate at Section B. The largest stress measured on the bottom of the deck plate occurred at BDP_L9, at the deck mid-span. The largest stress measured on the top of the deck plate occurred at TDP_L13, located at Section B, though all stresses on the top surface of the deck plate were compressive. At Section D, back-to-back gauges TDP_6 and BDP_4 recorded similar compressive stresses; this was due to the deck plate acting as a membrane in this location. For the gauges located under the load pads, there is a large differential between stresses recorded on the top and the bottom of the deck plate. This was due to local flexural deformation of the deck plate, which would deflect downwards between stringers, beneath the load pad.

The transverse stresses on the top and bottom of the deck plate, measured along Section A, are plotted in Figure 46. All gauges located on the underside of the deck plate measured compressive stress. On the top of the deck plate, the two exterior gauges measured tensile stress, and the two interior gauges, showed compressive stress. None of the gauges along this path were positioned beneath the load pad, however, TDP_T13 and TDP_T12 were less than 1 in. (25.4 mm) from the edge of the load pad. At those locations, the deflection was sufficient to cause membrane stresses, while further from the load the stress is due to the flexural bending of the deck plate.

The measured stresses in the biaxial gauge on the top of the deck plate of Specimen #1, under the load pad near the end of the deck, are plotted in Figures 47 and 48. This gauge was located at E-8, beneath the east load pad. The measured stresses in the longitudinal (TDP_L5) and transverse (TDP_T5) directions demonstrated nonlinear elastic response. The effect of nonlinearity was more significant in the transverse direction, as the deck plate underwent flexural deformation as it spanned between stringers. Nonlinear stresses were recorded in many of gauges placed on the top and bottom of the deck plate, due to the non-uniform pressure that developed under the load pad. The non-uniform pressure resulted from the non-uniform contact that occurred between the flexible deck plate and the deformable rubber pad. Similar nonlinearity in the measured stress response was also noted at the biaxial gauge on the top surface of the deck plate of Specimen #1 under the load pad near the center of the deck, as shown in Figures 49 and 50.

The stresses measured in gauges TDP_5 of Specimen #1 are plotted in Figure 51. Uniaxial gauge TDP_5 was placed on the top of the deck plate, equidistant from stringers

S5 and S6. The gauge was oriented in the longitudinal direction, and as expected, the stresses were compressive at the top of the deck plate. Gauge BDP_4, shown in Figure 52, was located on the underside of the deck plate, directly beneath TDP_5. The stresses measured at this gauge were also compressive, due to the deck plate acting as a membrane with equal stress throughout.

The measurements of S5_DW2, a uniaxial gauge installed in line with the stringer-to-deck intermittent welds, are shown in Figure 53. This gauge was placed at the toe of the weld in the longitudinal direction of the deck, and measured linear elastic stress.

4.4 Response of Stringer-to-Tube Connections

Testing of the V1 deck confirmed that the most critical location of the bridge deck was the welded stringer-to-tube connections. Under load, out-of-plane deformation of the stringer web occurs as the stringer web maintains compatibility with the flexural deformation of the transverse tube. All cracking that occurred during fatigue tests of the V1 deck occurred from the weld toe or weld root of this connection. In order to closely monitor this occurrence in the V2 deck, the instrumentation layout included rectangular rosettes and uniaxial gauges at these connections.

The stresses found at the northern, or the welded side, of the connection between stringer S4 and tube T2 show the out-of-plane deformation. Table 3 compares the stresses measured at the north side of the web at the S4-T2 during static tests of Specimen #1 and #2. In Table 3, principal stress P refers to the stress in the primary stress direction, and principal stress Q refers to the stress orthogonal to the primary stress direction. It can be seen that the rosette measures compressive stresses close to the weld. However, the stress

found by uniaxial gauges surrounding the rosettes are both positive. The stress reverses between S4_T2R1, the vertical rosette strain gauge, and S4_T2W1, the vertical uniaxial gauge placed less than $^1/_2$ in. (12.7 mm) away.

In Table 3, Specimen #1 and #2 had similar values for principle stress P and Q, however, there is nearly a 60˚ difference in the principle stress angle, which represents the direction of application of principle stress P. The variation can be attributed to differences in the welds at the stringer-to-tube connections. A comparison of the weld length and placement at the gauged stringer-to-tube connections on specimens #1 and #2 is presented in Table 4. When compared to the weld layout indicated by the deck plans, all stringer-to-tube connections had a smaller bottom gap, which resulted in the welds being lower, and closer together at the bottom of the tube, than anticipated. At some connections, the welds were noticeably different in length. This occurred at the S4-T2 connection on Specimen #2, where the west weld was found to be $^1/_2$ in. (12.7 mm) longer than the east weld.

During the FEA of the V1 deck, the stringer-to-tube connection was identified as an area with a high gradient stress field. This high gradient stress field was also expected in the V2 deck. Therefore, a small change in the connection detail can result in significant changes to the measured stress values. The variation of weld length and placement could significantly affect the stress gradient. Also of note is that the location of the strain gauges at the stringer-to-tube connections were based on the weld location. Rosette gauges were placed a specified distance from the weld toe, either from the top of the weld or the bottom of the weld. In the high gradient stress field that was predicted at this location, a small change in the location of the strain gauge could cause significant

variation in the measured stresses. In this case, the weld location and the strain gauge location varied between connections. This made it difficult to compare the measured stresses at the stringer-to-tube connections between the specimens.

On the web of S7, which is a mirror to S4, the opposite stress reversal occurs. Table 5 shows the stresses in the north rosette and surrounding uniaxial gauges at the S7-T2 connection in Specimen #2. As before, the weld is on the northern side of the stringer, however, the load placement results in the rosette measuring tensile stress close to the weld. Again, these values are completely reversed prior to the connection to the top flange of the stringer, as can be seen in the compressive uniaxial gauge measurements.

For the two center stringers, S5 and S6, rosettes were placed on the bottom of the connection, on the welded side of the web. A second rosette was also placed adjacent to the first, on the tube. The stress found in the web of the S5-T2 connection of Specimen #1, for the rosette placed on the stringer web, is shown in Table 6. The primary principle stress was found to be roughly in line with the vertical rosette arm. Away from the weld, the longitudinally aligned uniaxial gauge measured a stress close to the principle stress, implying the primary stress direction shifts from vertical to horizontal as it moves away from the weld.

Table 7, which shows the stresses found in gauge S5_T2T, placed on the tube adjacent to S5_T2W, indicates that the principal stress direction is not in-line with the tube, but across it, as a hoop stress. Further from the weld, however, the stress becomes more oriented with the tube, as indicated by the readings on S5_T2W2, the uniaxial gauge placed in line with the tube. Away from the stringer-to-tube connection, the stress found in the tube is the result of flexural bending of the tube.

4.5 Deck V1 versus Deck V2

Comparisons between the V1 and V2 decks were made using Specimen #1 for both decks. For the V1 deck, the results of the third static test, conducted on August 25, 2009, were used. The V2 deck measurements were from the fourth static test, conducted on March 25, 2013. This was done to prevent the residual deck stresses from influencing the results. The static test results are labeled as "V1" or "V2".

In Figure 54, the vertical deck displacements along the bottom of S5 are shown for the V1 and V2 decks. Additionally, Figure 55 presents the vertical deck displacements along the soffit of S3 for the V1 and V2 decks. In both plots, the LVDTs at Section D (located 30 in. (762 mm) from the edge of the deck) found larger displacements in the V2 deck than in the V1 deck, while the two LVDTs in the middle of the deck (sections A and B) clearly show a smaller mid-span deflection in the V2 deck. The plot shows that the overall deck curvature along S5 and S3 is much smoother in the V2 deck than the V1 deck. The addition of thicker tubes and a thicker deck plate reduced the mid-span deflection of the deck, and reduced the curvature of the deflected shape as well.

Figure 56 plots the vertical deflection along T2 for the V1 and V2 decks. The transverse deflection remained similar in curvature between the V1 and V2 decks. As with the longitudinal deflection, V2 deflected less than V1 for the two LVDTs closest to the middle of the deck. The V1 deck had no LVDTs placed beneath the cover plate, so a comparison at that location could not be made.

In Figure 57 the longitudinal stresses along the soffit of the stringer and the top of the deck plate above the centerline of S5, for the V1 and V2 decks are compared. The

plot shows that the stresses found in V2 echo the results of V1. Similarly, Figure 58 presents the longitudinal stresses along the soffit of S3 and the top of the deck plate along the centerline of S3, for the V1 and V2 decks. Along S3, the stresses measured in the V2 deck were closer to zero than the stresses measured on the V1 deck. While some strain gauges measured a large reduction in the stress between the V1 and V2 decks, these results were not consistent across both decks, and rarely consistent along the same stringer. Along S5 and S3, largest difference was a stress reduction of approximately 30% of the value, and the smallest difference was a stress reduction of less than 1%.

Figure 59 presents the transverse stresses measured along the soffit of the transverse tube, and the top of the deck plate along the centerline of T2, for the V1 and V2 decks. The stresses in the V2 deck echo the trend of the stresses in the V1 deck, and are, in general, the stresses measured in the V2 deck are closer to zero than those measured in the V1 deck. As before, however, the magnitude of the stress decrease was inconsistent.

Overall, a comparison between the measurements in the strain gauges of the V1 and V2 decks showed a slight, but not significant, reduction in the measured stresses. A tabulated comparison of the third static test of Specimen #1 of the V1 deck, and the fourth static test of Specimen #1 of the V2 deck, can be found in Appendix A.

5. RESULTS OF FATIGUE TEST

An evaluation of the fatigue tests, and the performance of the stringer-to-deck connection, is discussed in this chapter. Fatigue testing was conducted at minimum and maximum load levels of 2 and 9 kip (9 and 40 kN), respectively. Each specimen was tested 24 hours a day, until the discovery of fatigue cracks. Following crack data collection, the fatigue test continued until the specimens sustained 10 million cycles.

5.1 Stringer-to-Tube Weld Cracks

5.1.1 Specimen #1

Fatigue testing of Specimen #1 was initiated on April 22, 2013, and was suspended on May 23 after approximately 8.0 million cycles, when multiple fatigue cracks were discovered at several stringer-to-tube connections. With dye penetrant testing, cracks were found at the west welds of S4-T1 and S4-T3, the east weld of S8-T2, and at both welds of S4-T2, S5-T2, S7-T1, S7-T2, S7-T3, S9-T1, S9-T2, S9-T3 and S9-T4. All cracks originated at the top termination of the stringer-to-tube fillet, and propagated into the stringer web. In some instances, cracks would immediately progress into the web after initiating at the weld toe. In other instances, the cracks propagated along the weld toe for a short distance before branching into the stringer web.

Cracks propagating from the top of the weld termination would propagate into the stringer web horizontally, diagonally downwards, or diagonally upwards. The east crack at S5-T2, shown in Figure 60, extended into the web horizontally. The majority of the cracks that originated from the top of the weld termination would propagate into the web

horizontally, or diagonally upwards, such as at the west crack at S5-T2, shown in Figure 61.

The remaining cracks would originate from the top weld termination, and propagate along the weld toe for up to $^{1}/_{2}$ in. (12.7 mm) before propagating into the stringer web. Typically, these cracks would propagate into the web horizontally, such as in the east crack at S7-T3, shown in Figure 62, or they would travel diagonally downwards, such as in the west crack of S9-T4, shown in Figure 63.

Three cracks in Specimen #1 split to have two separate branches. One example is the west crack of S7-T1, which can be seen in Figure 64. All three branched cracks originated from the top weld termination, and propagated about the weld toe for $^{1}/_{8}$ in. (3.18 mm) to $^{3}/_{8}$ in. (9.53 mm). The top branch would propagate into the web horizontally or would extend diagonally upwards. The bottom branch would typically propagate down the weld toe for another $^{1}/_{8}$ in. (3.18 mm), before propagating into the web horizontally or diagonally downwards.

Fatigue cracks propagate normal to the primary stress direction, so the crack path can lend information to the stress field in the stringer web. In general, cracks that propagated horizontally were located at the east or west side of the T2 connections. This implies that the principle stress was mainly vertical at this location. Four of the seven cracks that propagated upwards were found on stringer S9, from the west weld of tube T1 and T2, and the east weld of T3 and T4, which indicates how the stress field changed direction from one half of the span to the other. Two of the three branched cracks occurred on S7, at the west weld of T1 and T2. As mentioned earlier, S7-T2 was the most critical stringer-to-tube connection, due to the tensile stress around the weld toe. The

branched cracks imply that the stress field was complicated around the T1 and T2 connection.

The fatigue test resumed on May 30, and continued for another six days, until 10 million cycles was reached. No additional fatigue cracking was found during this period. After completion of the fatigue test, the deck plate was removed to allow for closer examination of the fatigue cracks at the stringer-to-tube connections. It also allowed for pictures of the east and west cracks at a connection, as can be seen in Figures 62 through 64.

5.1.2 Specimen #2

Fatigue testing of Specimen #2 was initiated on June 24, and was continued 24 hours a day until July 18, when fatigue cracks were discovered at S7-T2 at approximately 9.0 million cycles. The fatigue test was suspended for further investigation with dye penetrant test, which revealed additional cracks at the west weld of S7-T1, and at both welds of S7-T2, S7-T3, S8-T1, S8-T2, S8-T3, S9-T1, S9-T2, and S9-T3. Similar to Specimen #1, all cracks in Specimen #2 occurred at the stringer-to-tube connections.

All cracks initiated from the top weld termination. Three cracks initiated from the top of the weld and propagated into the stringer web. Crack growth occurred horizontally, or the crack curved upwards, as can be seen in Figure 65, which shows the west crack at S9-T1.

The majority of the cracks in Specimen #2 originated at the top of the weld termination, and would propagate along the weld toe for $^1/_4$ in. (6.35 mm) to $^1/_2$ in. (12.7 mm), before propagating into the stringer web. These cracks would typically grow

horizontally in the stringer web, or diagonally downwards, as can be seen Figure 66, the east crack at S9-T1.

Three cracks were also observed to initiate from the top weld termination, propagate downward through the weld metal, and then propagate into the stringer web. This can be seen in Figure 67, which shows the west crack at S7-T1. All cracks of this type extended into the web diagonally downwards.

Specimen #2 also had two cracks that split into two separate branches. The S8-T1 east crack, shown in Figure 68, had a top branch that propagated from the weld toe, and a bottom branch that continue down the weld for $^{1}/_{8}$ in. (3.18 mm) before it propagated into the web. Unlike in Specimen #1, where the branches were typically equal in length, the top branch of this crack was $^{1}/_{8}$ in. (3.18 mm), and the bottom branch was $^{3}/_{8}$ in. (9.53 mm).

The fatigue test resumed on July 22, and continued until 10 million cycles was reached on July 25. At this time, additional cracking was observed at the east weld of S7-T1, and at both welds of S9-T4. The crack at the east weld of S7-T1 was visible only through dye penetrant testing, as the crack had traveled around the weld toe and had yet to grow into the web. The cracks at the S9-T4 connection were less than $^{1}/_{8}$ in. (3.18 mm) long, and the crack that occurred at the west weld at S9-T4 had two branches.

5.2 Postmortem Evaluation

A post mortem evaluation of several fatigue cracks was conducted to characterize the origins and growth of those cracks. By exposing the fracture surface, fractography can be used to determine the site of initiation, the cause of the crack growth, and the

mode of failure. Metallographic techniques were used to examine the welded connection at the side of the crack initiation.

Four typical fatigue fracture surfaces in Specimen #1 were exposed. The deck plate was separated from the stringers by air-arcing the intermittent welds between the deck plate and the stringers. The stringer-to-tube connections at S9-T2 and S5-T2 were selected for fractographic examination, so portions of the stringers and tubes that contained fatigue cracks were flame cut. S5-T2 was selected due to the length of the cracks, which the longest cracks found in Specimen #1, and were shown previously in Figures 60 and 61. The connection S9-T2 was selected due to the unexpected presence of fatigue cracking at that location. Stringer S9 was close to the edge of the deck, and as a result, experienced less deflection than the stringers in the middle of the deck. A smaller deflection is typically indicative of a smaller stress range, thus cracking was not anticipated at the S9 connections as it was for S4, S5, S6 and S7 connections, which experienced larger deflections.

The cut S5-T2 and S9-T2 connections were trimmed with a band saw, and the remaining ligaments of the stringer webs were saw cut to break the pieces apart and expose the fracture surface. The exposed surface was cleaned and photographed before it was examined under a microscope to investigate the origin point of initiation.

A plan view of the connection at S5-T2 is shown in Figure 69. The weld reinforcements on both sides had inconsistent size and length. As per the fabrication drawings, each weld was intended to be 2 in. (50.8 mm) long and deposited symmetrically about the horizontal midpoint of the tube. An example of this can be seen in Figure 31, which shows the plan view of the S5-T2 connection. Figure 69 shows that

the as-fabricated welds were of different lengths and non-symmetric with respect to the horizontal axis of the tube. Both welds were shifted closer to the bottom of the tube, increasing the unwelded section at the top.

From the cut pieces, the east and west weld cross sections were cut, polished, and etched to examine the weld profile at the stringer-to-tube connections. Visual examination of the weld sections suggested that the quality of the weld fabrication was inadequate. The cross section of the east weld at S5-T2 is shown in Figure 70. The weld was uneven, with the length of the tube leg exceeding the length of the stringer leg. The profile also shows excessive penetration into the base metal of the tube. There is a clear lack of penetration (LOP) between the stringer and the tube, however, this is natural for fillet welds. At this connection, the LOP was exacerbated by the gap between the stringer and the tube.

Similar inadequate fabrication quality, with inconsistent weld length and placement, was noted at S9-T2. Figure 71 shows the west weld at S9-T2, where a tack weld left on the south side of the connection can be seen. The weld section, shown in Figure 72, had a better profile than S5-T2 (Figure 70).

Visual inspection of the remaining 38 welded connections showed signs of significant weld fabrication defects. Common issues were inconsistent length deposition and asymmetry, which can also be seen Figure 73 for the S4-T4 connection. Weld metal drips were apparent in some of the stringer-to-tube welds, shown in Figure 74, which shows a large drip at the top of the west weld at S8-T2. Significant weld spatter along the weld toe was also an occurrence, as shown in Figure 75, which shows spatter at the bottom of the east weld at S8-T3.

The fatigue cracks at S5-T2 on both sides originated at the top weld termination, from the weld toe. The east crack, shown in Figure 60, was $^{3}/_{4}$ in. (6.4 mm) long and horizontally grew into the stringer web. Figure 61 shows the west crack, which grew into the weld diagonally upwards at about 30˚ for 1.0 in. (25 mm). Figure 76 shows the bottom part of the exposed east fatigue fracture. The east crack planes at the S5-T2 connection were flat and smooth, which is characteristic of fatigue cracking. Figure 77 shows the S5-T2 west crack plane to be similarly smooth.

The S9-T2 connection also developed fatigue cracking on both sides. The east crack, shown in Figure 78 (a), originated from the top termination of the weld toe, and grew into the web horizontally for $^{1}/_{2}$ in. (13 mm). Figure 78 (b) shows the west crack also originated from the toe of the weld termination at the top, but propagated in two branches. The upper branch followed the edge of the weld toe for $^{1}/_{4}$ in. (6.4 mm) before growing horizontally $^{1}/_{8}$ in. (3.2 mm) into the stringer web. The other branch continued down the weld toe for another $^{1}/_{8}$ in. (3.2 mm) before extended outwards at a downward diagonal of about 10˚ for $^{5}/_{16}$ in. (7.9 mm).

The exposed fracture surface of the west crack at S9-T2 is shown in Figure 79. Upon cutting the west crack open, it was apparent that the crack that ran through the stringer web diagonally. The east crack fracture surface, shown in Figure 80, was similar, as it also ran through the web diagonally. Both fracture surfaces had a smooth texture typical of fatigue fracture.

The four exposed fracture surfaces were examined under a scanning electron microscope (SEM) by Dr. Eric Kaufman, a metallurgical consultant with expertise in forensic evaluation to identify the origins of the fatigue cracking. There was no evidence

of beach marks on the fracture surface that would indicate the origin or propagation of the fatigue cracks. However, the cracks appeared to initiate from a weld crater at the weld termination that was evident by incomplete fusion along the weld toe. A weld crater results when the welding arc extinguishes before the base metal is fully fused (ASM International 2012). This is often referred to as cold lap, and it is a common weld crater defect.

The east and west crack fracture surfaces at S5-T2 were similar in appearance. At the weld toe on the stringer, the SEM showed evidence of incomplete fusion. The east crack fracture surface, shown in Figure 81, showed evidence of incomplete fusion along the weld toe on the stringer. The fracture surface of the S5-T2 west weld crack, shown in Figure 82, had evidence of incomplete fusion at the weld toe on the stringer, and the weld toe on the tube.

The S9-T2 west crack fracture surface, shown in Figure 83, was similar to the fractures surfaces at the S5-T2 connection. The incomplete weld toe fusion on the stringer found in this crack was larger than those observed at the S5-T2 crack surfaces. The fracture surface was also discolored by heat. The fracture surface for the east weld of S9-T2, shown in Figure 84, had no distinct fracture morphology to identify the crack initiation mechanism, though a small thumbnail discoloration along the weld toe was seen on both sides of the fracture.

5.3 Assessment of Fatigue Performance

The results of the fatigue test are plotted in Figures 85−96. The plots present the maximum and minimum stresses at a specified gauge found over a 30 second interval during inspection, in addition to the stress range, over the course of the fatigue test. The

cycle count, in millions of cycles, is shown on the abscissa, or x-axis, and on the ordinate, or y-axis, is the measured stress. The location of the gauge is shown on the plot key. For a gauge located near the stringer-to-tube connections, a diagram of the gauge layout is also shown for clarity. Principle stresses on the stringer web were determined from the rectangular rosette stress measurements.

Figure 85 shows the transverse stress at gauge T2_4, at Location B8. As shown, the maximum and minimum stresses at this gauge remained consistent for most of the test. The initial inconsistencies that are shown between zero and 0.3 million cycles were due to difficulties in sustaining the test load at the start of the test, as discussed previously in Section 3.5.2. In general, the minimum and maximum gauge values remained fairly consistent, and any small changes that occurred were undergone by both, so the range remained constant. This was typical of all uniaxial and biaxial gauges not subject to localized forces (placed at the stringer-to-tube connections).

This was confirmed in Specimen #2. Throughout the test, the stresses recorded by S5_B3 at Location B7, shown in Figure 86, remained steady. Any changes in the stress values could be found in both the minimum and maximum, thus the range remained the same during the course of the test.

Gauges subject to local forces were prone to variable readings. This was most obvious in the measurement recorded by the rosettes, especially at locations where cracks were discovered. The S7-T2 intersection was identified as the connection most disposed to cracking, due to the out-of-plane distortion in the web, which caused tension at the weld. The principal stresses recorded in Specimen #2 at the northern face of this location can be seen in Figures 87 and 88. Principal stress P refers to the stress in the primary

stress direction, while principal stress Q refers to the stress orthogonal to the primary stress direction. As can be seen on both plots, the principal stress values found at this rosette remained consistent until approximately 2.25 million cycles, at which point the minimum and maximum stress values in both plots descend very quickly. Drastic changes in the stress values found at uniaxial gauges are usually indicative of the formation of cracks. The same holds true for rosette gauges. It can be assumed that, in Specimen #2, a crack at the S7-T2 stringer-to-tube connection began forming around 2.25 million cycles. This crack remained undetected until it propagated enough that it became visible during inspection.

The plots on the opposite face of the S7-T2 stringer-to-tube connection echo this result. Figure 89 and 90 show the principal stresses recorded in the south-facing rosette gauge. This gauge was placed back-to-back with the north-facing rosette on the other side of the stringer web. As can be seen, the principal stresses in the southern rosette show a large increase at approximately 2.25 million cycles, indicating that the presence of the crack was perceived on both sides of the web.

The uniaxial gauges on the stringer web are subject to local forces, just as the rosettes are, so the pattern can also be found in the uniaxial gauges that surround the rosette. This can be seen in Figure 91, which shows gauge S7T2_W1, and Figure 92, which plots gauge S7T2_W2. As in the north and south rosettes, the sudden changes in the stresses found in the web occur at approximately 2.25 million cycles. Also of significance is the magnitude of the change. Gauge S7T2_W2 experienced a decrease of over 20 ksi (140 MPa) as the crack initiated. S7T2_W1 experienced a drop of about 10 ksi (69 MPa). This was due to S7T2_W2 being significantly closer to weld, and only $^{3}/_{16}$

in. (4.8 mm) away from the rosette. S7T2_W1, however, is located as close as possible to the top stringer flange, and is therefore considerably further away from the stress field. Comparatively, the stress in gauge S7T2_R1, the rosette gauge aligned with S7T2_W1, follows the same pattern, but has a stress drop that is much larger at 2.25 million cycles. This can be seen in Figure 93.

Rosettes at different locations experienced this change at different times. For instance, the rosette on the north side of the web at the S9-T2 stringer-to-tube connection recorded a sudden decrease in stress at about 1.75 million cycles, implying that the crack at this connection initiated more quickly than the crack at the S7-T2 connection. The plot of the principal stress P at this rosette can be found at Figure 94; principal stress Q is shown in Figure 95. As with the S7-T2 connection, the pattern of the stress values recorded over the course of the test was echoed in the surrounding uniaxial gauges. This can be seen in Figure 96, which plots gauge S9T2_W1.

5.3.1 Performance of Stringer-to-Tube Connection

Fatigue test results of the temporary bridge deck specimens are plotted in Figure 97 on the fatigue design curves of the AASHTO LRFD BDS. The fatigue design curves are presented in terms of applied nominal stress range versus life endured before cracking (S-N) on a log-log (with respect to base 10) base. Fatigue performance of typical welded connections in highways bridges are classified in decreasing order in seven detail categories: A, B, B′, C′, C, D, E, and E′. The fatigue design curves were developed based on fatigue test results of full scale beam specimens under constant amplitude loading, and represent 95% confidence on 95% probability of survival fatigue life.

Due to complex geometry and distribution of stresses in the deck, nominal stresses for the stringer-to-tube connection detail could not be easily determined. In view of the high local stresses associated with the local bending of the tubes, a hot spot stress was determined at the weld toe as per International Institute of Welding recommendations (IIW 2005) as discussed in Section 3.3.3. For accurate determination of the demand, the hot spot stress was linearly extrapolated from the strain gauge measurements ahead of the stringer-to-tube welded connections. The extrapolation process is illustrated in Figure 98. Consistent with the IIW recommendations, the strain gauges at the stringer-to-tube connection were placed 0.4*t* and 1.0*t* ahead of the weld toe in the plane of the section, where *t* was the thickness of the tube or the stringer web. With the hot spot stress method, the fatigue test results are presented in terms of the local stress range, though the AASHTO fatigue design curves are defined in terms of the nominal stress range. The fatigue life of the stringer-to-tube connection detail in the temporary bridge deck specimens, when plotted with respect to the local stress range, fell on the design curve of AASHTO Category D in the finite life regime.

The hot spot stress calculations are shown in Table 8. Though cracks were found at 12 connections in Specimen #1 and 10 connections in Specimen #2, calculation of the hotspot stress was only available at those locations where the appropriate gauges had been installed. This included two locations at S4-T2 and two locations at S5-T2 in Specimen #1, and two locations at S4-T2, two at S6-T2, two at S7-T2 and one at S9-T2 in Specimen #2. Table 8 shows that there were large differences in the hot spot stress calculated at each connection. This is especially noticeable when comparing the S4-T2 hot spot stress, which should have been similar for both specimens. On the north face of

the stringer, the hot spot stress calculated on Specimen #1 is over eight times the hot spot stress calculated on Specimen #2. On the south stringer face, the hot spot stress on Specimen #1 was nearly triple the hot spot stress calculated on Specimen #2. As discussed previously in Section 4.4, these differences may be attributed to variations in the stringer-to-tube fillet weld size and placement, which would influence both the strain gauge location, and the high gradient stress field at this connection.

The stringer-to-tube connections, which had been previously identified in the study of the V1 deck as susceptible to fatigue damage, were made more susceptible to fatigue cracking by the weld fabrication deficiencies described in Section 5.2. The manually deposited welds introduced cold lap at the weld toe, from which fatigue cracks initiated. Incomplete fusion was found to be the crack origin for three of the four crack surfaces examined, suggesting that it was a common defect throughout the deck. The spatters and drops found at the stringer-to-tube welds were also evidence of inadequate weld fabrication.

Due to inherent variability, welded connections are expected to exhibit scatter in their fatigue performance. The limited test data for the subject deck was inadequate to evaluate the scatter and draw any significant conclusion. In that respect, the fatigue test results from this study should be considered as indicative.

6. CONCLUSIONS AND RECOMMENDATIONS

6.1 Conclusions

This study investigated the performance of an enhanced orthotropic bridge deck designed for temporary use under simulated AASHTO loading, through experimental and analytical studies. The fatigue performance of the V2 deck was evaluated by testing two full-size specimens on a set up that included full-size transoms supporting the deck at both ends. The applied loading, simulating the AASHTO fatigue design truck, was replicated with hydraulic actuators. The load disposition was decided based on studies of the V1 deck as the load case that produced the most critical stresses in the deck, primarily at the fatigue critical stringer-to-tube connections. For both specimens, the fatigue test was conducted up to 10 million cycles at the load range for finite fatigue life, or 7 kip (31 kN). This replicated the estimated deck lifespan of seven years in the field under interstate traffic operating within legal load limits.

Use of thicker deck plate and thicker transverse tubes for the V2 deck resulted in reduced displacement and stress responses compared to the V1 deck. The magnitude of the stress reduction between the V1 and V2 decks was found to be variable throughout the deck. At mid-span, the vertical displacement of the V2 deck was approximately 20% less than the V1 deck, and the deflection along the stringers and tubes appeared to have less curvature/was smoother in V2 than in V1. The stress responses measured in V2 was, in general, less than in V1. The percent difference in the stresses measured in decks V1 and V2 varied.

The magnitude of the stress reduction between the V1 and V2 decks was found to be variable throughout the deck. Small stress reductions were typically measured on the

underside of the stringers. Along the soffit of the transverse tube, the largest stress reductions were seen under the load pads. Variable stress reductions were found on top of the deck plate.

In the previous study performed on the V1 deck, the stringer-to-tube connection was identified as an area with a high stress concentration, as out of plane distortion of the stringer web due to the flexural bending of the tube resulted in a tensile stress at the fillet welded connection. To alleviate this stress concentration in the V2 deck, the tube thickness was increased and the stringer-to-deck plate welds above the tubes were eliminated (to allow more flexibility of the stringer). Therefore, instrumentation was concentrated around this detail to monitor the behavior of the fatigue critical connection. The fatigue resistance of the stringer-to-tube connection was assessed using a local stress based approach (hot spot stress approach). Compared to the fatigue performance of the previous study (using the hot spot stresses determined from the FEA), the performance of the V2 deck achieved a lesser AASHTO fatigue design curve rating.

Grillage analyses of the V1 and V2 decks were performed to validate the modeling technique against the previous FEA and measurements, and to assess and compare the global response of the deck under the wheel load. Compared to the more computationally expensive FEA, the grillage analysis had some agreement with the displacement and stress responses of the decks, as determined from the experiments, particularly at locations where the deck geometry coincided with the grillage members. Along the longitudinal grillage members (coinciding with stringers) the grillage analysis results were the most accurate away from direct loading. It must be noted that the grillage analysis cannot estimate the local response, such as those at the stringer-to-tube

connections, or on the deck plate under the load pad, for which a detailed FEA using continuum model is necessary.

The study demonstrated that the response of the orthotropic bridge deck was characterized by global longitudinal and transverse flexure of the entire deck. The results of multiple static tests of a specimen were repeatable, and the static tests of different specimens produced consistent behavior. Under the maximum static load, the measurements at the strain gauges were in the linear-elastic range. The measurements indicated local distortion at the stringer-to-tube connections and on the deck plate, under the load pads.

6.1.1 Performance of Stringer-to-Tube Welded Connections

The stringer-to-tube welded connection consisted of a fillet weld that connected approximately half of the circumference of the tube to one side of the stringer web. In the laboratory tests, fatigue cracks occurred at the stringer-to-tube welded connections, initiating from the weld toe to progress through the stringer web before the target 10 million cycles was reached. All cracks found during the fatigue testing of the V2 deck initiated at the top of the weld termination. The premature cracking was due to incomplete fusion at the weld toe, which was a result of the poor quality manually deposited welds used in the deck fabrication.

Due to the complex geometry and distribution of stresses in the deck, the nominal stresses for the stringer-to-tube connection detail cannot be easily computed. When plotted with respect to the local stress range, as recommended by IIW (2005), the fatigue life of the connection detail fell on the AASHTO Category D design curve, in the finite life regime. The categorization of this detail based on the nominal stress would be much

lower. No fatigue limit of this detail could be established from the fatigue tests. Due to inherent variability, the welded connections are expected to exhibit scatter in their fatigue performance. The limited test data was inadequate to evaluate this scatter and draw any statistically significant conclusions.

Using the hot spot stress approach, this connection was categorized as AASHTO Category D in the finite life regime. This was a lower rating than the V1 deck, which was rated at AASHTO Category C in the finite fatigue life regime. However, it is difficult to directly compare the fatigue performance of the V1 and V2 decks, due to the differences in their fabrication. The V1 deck specimens were fabricated using robotic welds, but the V2 deck was fabricated using manually deposited welds. The manually deposited welds were of lesser quality, containing several fabrication defects such as incomplete fusion, lack of penetration, and excessive penetration into the base metal, which resulted in the premature fatigue cracking in the V2 decks.

6.2 Recommendations

Testing of the enhanced temporary bridge deck provided critical information on issues related to deck fabrication, the extent of design improvement, and the expected response of the deck in service. As the stringer-to-tube welded connections were the site of all fatigue cracking, enhancing or eliminating this welded connection would be the most rational approach to improve the fatigue performance of the deck.

In the temporary bridge deck, the transverse tubes exist to improve the load distribution in the transverse direction. The tubes also provide the option of interlocking adjacent decks in the transverse direction for continuity and additional edge restraint. Thus the welded connection between the tube and the stringers cannot be eliminated. One

method of reducing the out-of-plane distortion induced stresses at this welded connection would be to increase the stringer flexibility by reducing the length of this weld (increasing the web gap) and/or making this weld asymmetric about the horizontal axis of the stringer. The increase in the web gap is necessary only adjacent to the deck plate.

As discussed in Section 4.4, the fillet welds at the stringer-to-tube connections were asymmetric, in that they were placed on one side of the stringer web. Under the test load, the out-of-plane bending of the stringer web would cause the weld toe to undergo tensile stress if the weld faced the load pad, and compressive stress if the weld faced away from the load pad. Since fatigue cracks are less likely to occur in an area of compressive stress, one possible method to improve the fatigue performance of the deck would be to reflect the placement of the stringer-to-tube fillet welds about the longitudinal centerline of the deck, and have them all face away from the deck centerline. In the case of the V2 deck, this would position the stringer-to-tube welds at S1 through S5 on the north face of the stringer web, and the stringer-to-tube welds at S6 through S10 on the south face of the stringer web. Of course, the load position is not fixed for a deck in-service. However, rearrangement of the welds would reduce the maximum possible welds subject to tension at the weld toe from ten to five.

6.3 Future Studies

The changes in the deck plate thickness and transverse tube thickness from the V1 deck to the V2 deck helped reduce the vertical deck deflection and reduce the deck stress response. However, the fatigue performance of the V2 deck was impeded by the manually deposited welds used in the specimen fabrication. The manually deposited welds were of inconsistent quality, which allowed for the initiation of numerous cracks.

For a more accurate assessment of the V2 deck enhancement, the fatigue tests would need to be repeated with specimens assembled using the robotic fabrication process. The effects of altering of the weld placement on the string-to-tube connections, as described in Section 6.2, would also be of interest and should be studied further.

Table 1. Summary of Calculated Section Properties for V1 Deck Grillage Members

Member Description	A (in.^{2})	$\bar{y}$ (in.)	I_y (in.^{4})	$\ddot{x}$ (in.)	I_x (in.^{4})	J (in.^{4})	C_w (in.^{6})	J_{eq} (in.^{4}) fx-fx	J_{eq} (in.^{4}) fx-fr
L1 w/o CP	3.20	3.27	13.43	2.18	4.38	0.05	19.54	27.09	6.82
L1 - w/ CP	4.20	2.46	22.20	2.55	7.59	0.07	N/A	N/A	N/A
L2 w/o CP	3.53	3.42	14.27	3.71	7.26	0.05	2.09	2.95	0.79
L2 w/ CP	4.53	2.64	24.08	3.33	10.86	0.08	N/A	N/A	N/A
L1 + L2 - Box Beam	8.73	2.55	58.74	5.56	212.22	N/A	N/A	26.05	26.05
L3, L4, L5	3.54	3.43	14.30	3.80	7.46	0.05	1.74	2.47	0.67
Tr1, Tr2 & Tr3 w/o CP	2.25	0.09	0.01	6.00	27.00	0.03	0.00	0.03	0.03
Tr2 w/ CP	5.00	2.88	31.69	6.28	55.04	0.08	415.59	500.01	1302.15
Tr3 w/ CP	5.25	2.98	32.92	6.00	63.00	0.09	394.83	475.05	1237.12
Tr4 & Tr5 w/o CP	3.84	1.14	7.36	6.00	28.45	0.03	0.11	0.16	0.36
Tr4 & Tr5 w/ CP	6.84	2.90	34.55	6.00	64.45	2.98	422.46	511.75	1327.15

Table 2. Summary of Calculated Section Properties for V2 Deck Grillage Members

Member Desc.	A (in.^{2})	$\bar{y}$ (in.)	I_y (in.^{4})	$\ddot{x}$ (in.)	I_x (in.^{4})	J (in.^{4})	C_w (in.^{6})	J_{eq} (in.^{4}) fx-fx	J_{eq} (in.^{4}) fx-fr
L1 w/o CP	4.28	3.73	16.21	2.35	7.74	0.14	21.60	30.04	7.64
L1 - w/ CP	5.28	3.00	28.29	2.62	10.65	0.16	N/A	N/A	N/A
L2 w/o CP	4.94	3.91	17.17	3.72	13.90	0.17	3.16	4.57	1.30
L2 w/ CP	5.94	3.23	30.70	3.43	17.69	0.19	N/A	N/A	N/A
L1 + L2 - Box Beam	11.21	3.12	70.50	6.09	313.36	N/A	N/A	37.83	37.83
L3, L4, L5	4.97	3.91	17.21	3.80	14.31	0.17	3.00	4.36	1.24
Tr1, Tr2 & Tr3 w/o CP	4.50	0.19	0.05	6.00	54.00	0.21	0.00	0.21	0.21
Tr2 w/ CP	7.25	2.14	45.38	6.19	82.16	0.27	573.01	689.60	1795.57
Tr3 w/ CP	7.50	2.25	47.86	6.00	90.00	0.27	573.44	690.12	1796.93
Tr4 & Tr5 w/o CP	6.61	1.02	11.67	6.00	55.83	3.87	0.08	4.27	4.56
Tr4 & Tr5 w/ CP	9.61	2.37	50.18	6.00	91.83	3.93	629.11	761.48	1975.73

Table 3. Comparison of Stresses at North S4-T2 Connection

	Measurements		Calculated Principle Stress[a] and Direction[b]			
Face	Gauge	Stress[a] (ksi)	σ_P (ksi)	σ_Q (ksi)	Direction φ (degrees)	Illustration
Specimen #1, Static Test 3/25/2013						
North	S4_T2R1	-41.18	-20.12	-43.50	18.37	
	S4_T2R2	-38.81				
	S4_T2R3	-22.44				
	S4_T2W1	45.48	N/A			
	S4_T2W2	4.68	N/A			
Specimen #2, Static Test 6/17/2013						
North	S4_T2R1	-39.23	-18.98	-55.02	-41.45	
	S4_T2R2	-19.12				
	S4_T2R3	-34.78				
	S4_T2W1	40.91	N/A			
	S4_T2W2	1.37	N/A			

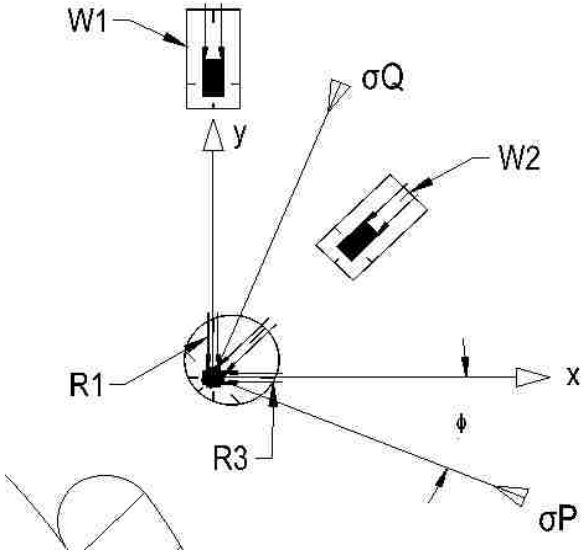

Notes: [a] Tensile stresses are positive

[b] Counter-clockwise angles are positive

Stresses due to applied load of 22 kips

Table 4. Comparison of Weld Layouts at Gauged Stringer-to-Tube Connections

Location	Lweast (in.)	Lwwest (in.)	Lbottom (in.)	Ltop (in.)	Comments	Illustration
Plans	2.00	2.00	2.52	2.52	Welds and gaps are symmetrical.	
Specimen #1						
S4-T2	2.00	2.00	2.00	3.03	Welds lower than plans indicate.	
S5-T2	2.13	2.13	1.75	3.03	Welds lower than plans indicate.	
Specimen #2						
S4-T2	2.00	2.50	2.00	2.53	Welds lower than plans indicate. West weld extends higher than east weld.	
S6-T2	2.13	2.38	1.75	2.78	Welds lower than plans indicate. Large weld toe on bottom west weld.	
S7-T2	2.00	2.00	1.88	3.16	Welds lower than plans indicate.	
S9-T2	2.00	2.13	1.88	3.03	Welds lower than plans indicate. West weld starts higher than east weld.	

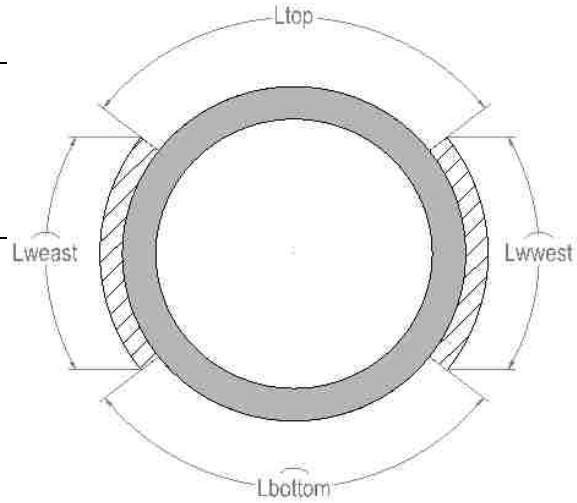

Notes: All welds on north face of stringer

All gauges placed adjacent to west weld

Table 5. Comparison of Stresses at North S7-T2 Connection

	Measurements		Calculated Principle Stress[a] and Direction[b]			
Face	Gauge	Stress[a] (ksi)	σ_P (ksi)	σ_Q (ksi)	Direction φ (degrees)	Illustration
Specimen #2, Static Test 6/17/2013						
North	S7_T2R1	20.27	33.70	11.42	-39.08	
	S7_T2R2	11.65				
	S7_T2R3	24.84				
	S7_T2W1	-35.26	N/A			
	S7_T2W2	-11.52	N/A			

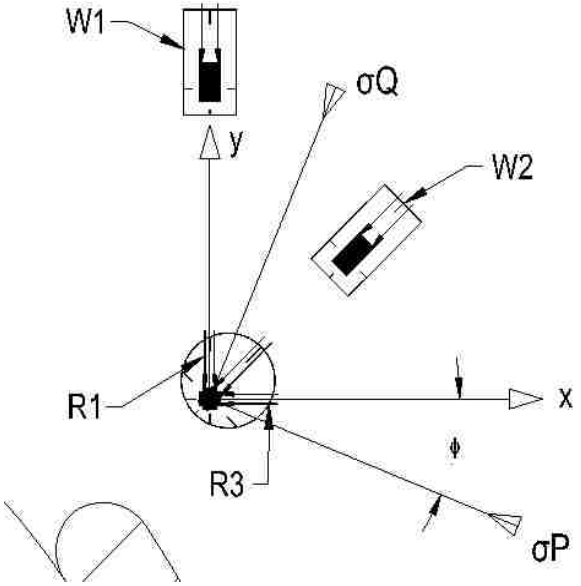

Notes: [a] Tensile stresses are positive

[b] Counter-clockwise angles are positive

Stresses due to applied load of 22 kips

Table 6. Comparison of Stresses at the Web of the S5-T2 Connection

	Measurements		Calculated Principle Stress[a] and Direction[b]			
Face	Gauge	Stress[a] (ksi)	σ_P (ksi)	σ_Q (ksi)	Direction φ (degrees)	Illustration
Specimen #1, Static Test 3/25/2013						
North	S5_T2R1	21.56	21.60	5.73	2.98	
	S5_T2R2	12.84				
	S5_T2R3	5.78				
	S5_T2W1	18.02	N/A			
Specimen #1, Static Test 4/29/2013						
North	S5_T2R1	21.32	21.32	6.40	0.78	
	S5_T2R2	13.66				
	S5_T2R3	6.40				
	S5_T2W1	18.19	N/A			

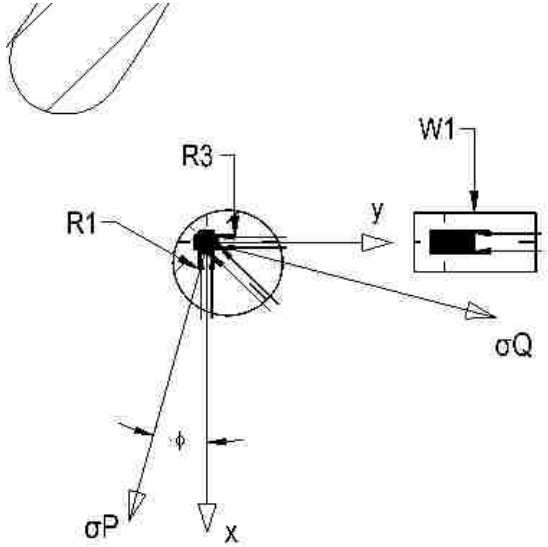

Notes: [a] Tensile stresses are positive

[b] Counter-clockwise angles are positive

Stresses due to applied load of 22 kips

Table 7. Comparison of Stresses at the Tube of the S5-T2 Connection

	Measurements		Calculated Principle Stress[a] and Direction[b]			
Face	Gauge	Stress[a] (ksi)	σ_P (ksi)	σ_Q (ksi)	Direction φ (degrees)	Illustration
Specimen #1, Static Test 3/25/2013						
North	S5_T2R4	4.66	17.38	4.64	-87.80	
	S5_T2R5	11.50				
	S5_T2R6	17.36				
	S5_T2W2	13.06	N/A			
Specimen #1, Static Test 4/29/2013						
North	S5_T2R4	4.14	16.87	4.11	-87.50	
	S5_T2R5	11.05				
	S5_T2R6	16.85				
	S5_T2W2	12.93	N/A			

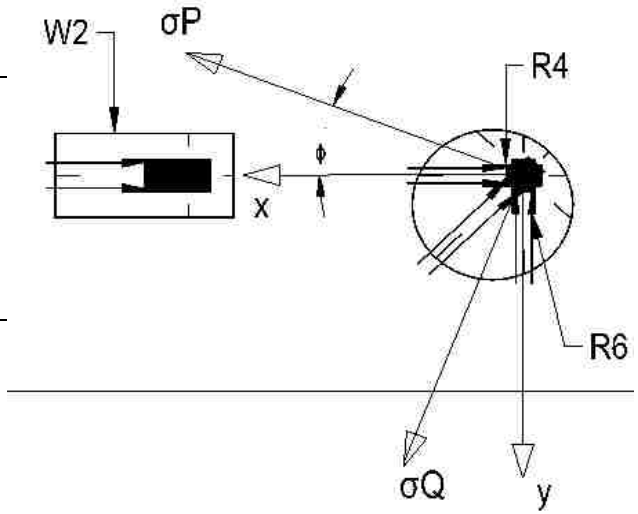

Notes: [a] Tensile stresses are positive

[b] Counter-clockwise angles are positive

Stresses due to applied load of 22 kips

Table 8. Hot Spot Stress at Stringer-to-Tube Connections

Location	Face	Measurements				Calculated Hot Spot Stress[a]
		Gauge	σ_{max} (ksi)	σ_{min} (ksi)	σ_{range} (ksi)	σ_{ht} (ksi)
Specimen #1						
Web	North	S4_T2R2	-5.40	-10.81	5.41	5.56
		S4_T2W2	0.64	-4.54	5.18	
Web	South	S4_T2R5	1.97	-5.60	7.57	8.52
		S4_T2W4	-0.18	-6.33	6.15	
Web	North	S5_T2R3	0.37	-0.82	1.19	-2.45
		S5_T2W1	7.60	0.97	6.63	
Tube	North	S5_T2R4	7.20	1.57	5.63	5.97
		S5_T2W2	5.95	0.83	5.12	
Specimen #2						
Web	North	S4_T2R2	-0.26	-0.82	0.56	0.69
		S4_T2W2	0.84	0.47	0.37	
Web	South	S4_T2R5	-0.17	-3.85	3.68	2.58
		S4_T2W4	-0.48	-5.81	5.32	
Web	North	S6_T2R3	6.97	1.69	5.28	4.81
		S6_T2W1	7.95	1.96	5.99	
Tube	North	S6_T2R4	8.46	2.23	6.23	6.56
		S6_T2W2	7.94	2.20	5.74	
Web	North	S7_T2R2	1.94	1.47	0.47	-2.02
		S7_T2W2	0.27	-3.91	4.18	
Web	South	S7_T2R5	2.09	-0.83	2.92	1.12
		S7_T2W4	6.57	0.96	5.61	
Web	North	S9_T2R2	4.39	0.88	3.50	4.52
		S9_T2W2	0.03	-1.97	2.00	

Notes: [a] Tensile stresses are positive

Maximum stress due to load of 9 kip

Minimum stress due to load of 2 kip

Hot spot stress calculated for load range of 7 kip

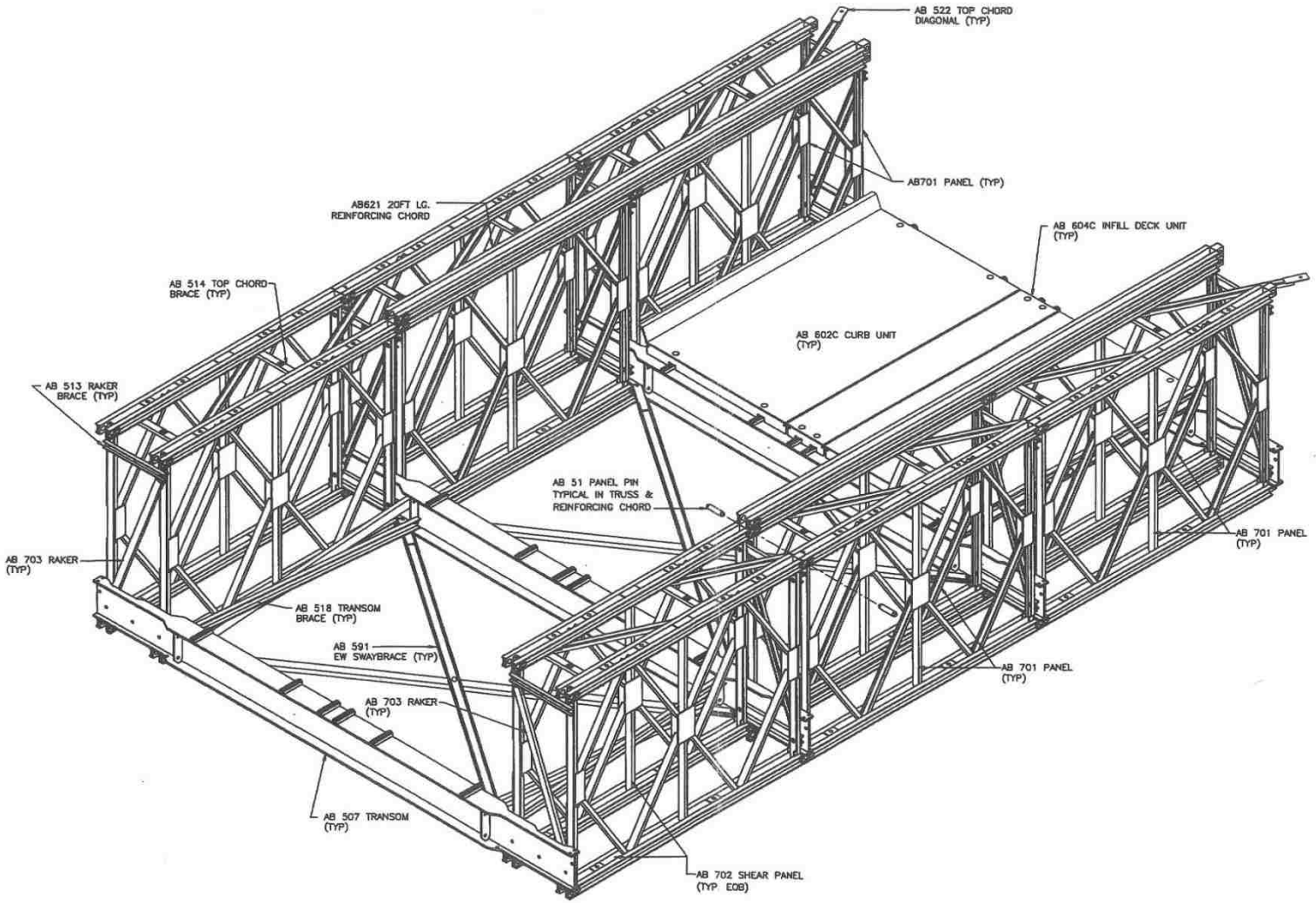

Figure 1. Isometric view of temporary bridge showing arrangement of components

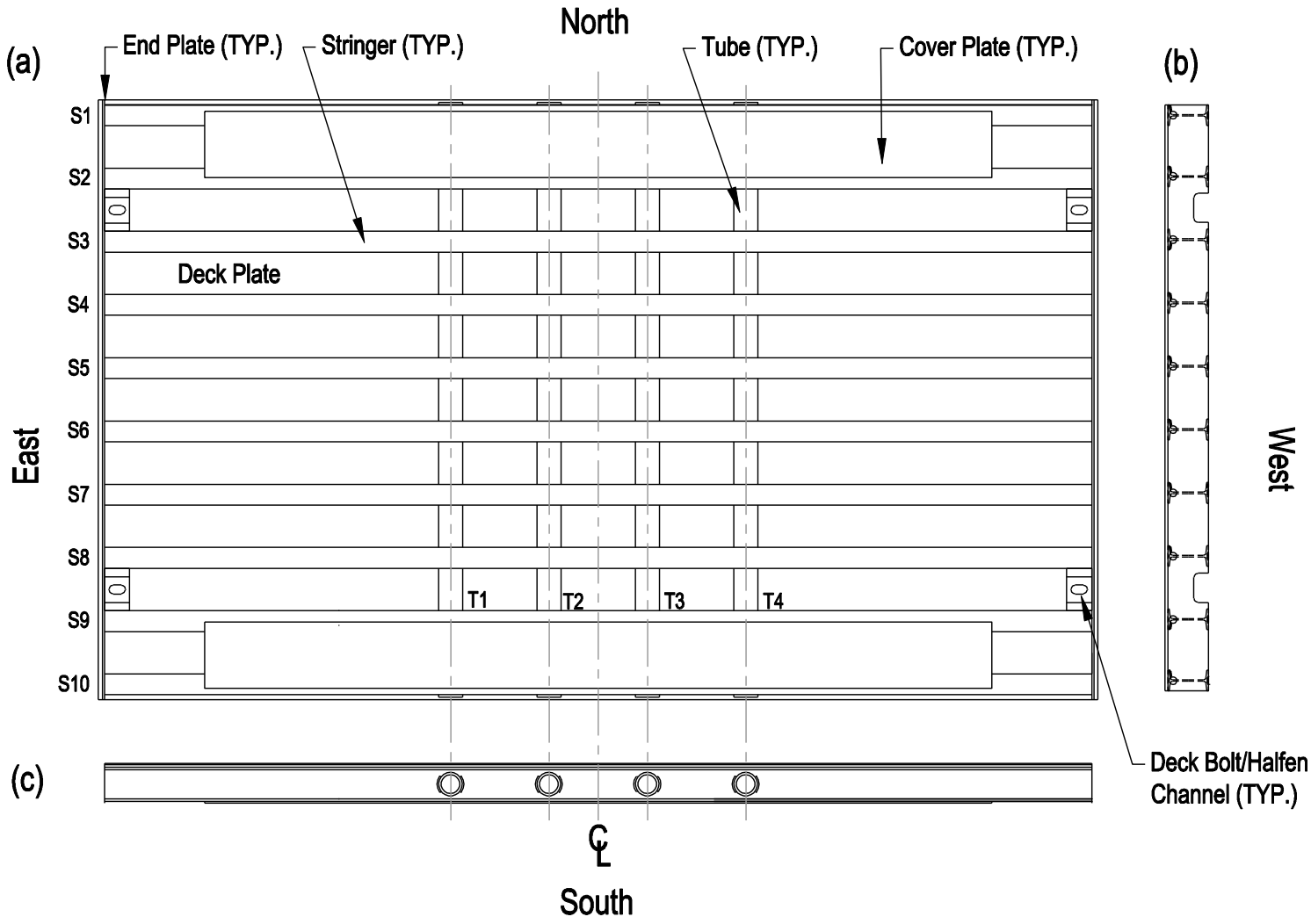

Figure 2. General Schematics of the V1 and V2 decks, (a) Underside view, (b) East/West end view, (c) North/South edge view

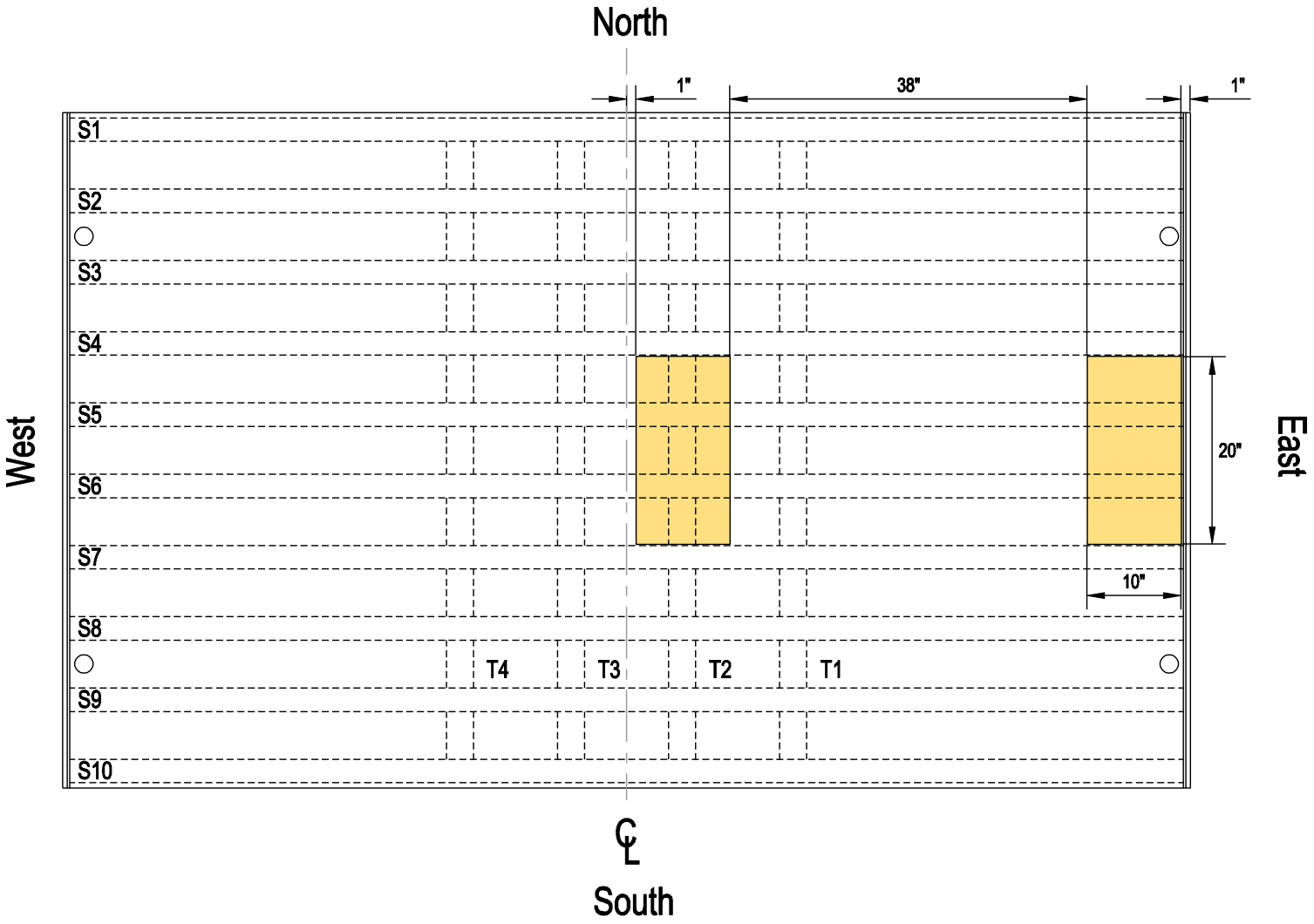

Figure 3 LC-5, position of load pads on the top of the deck plate

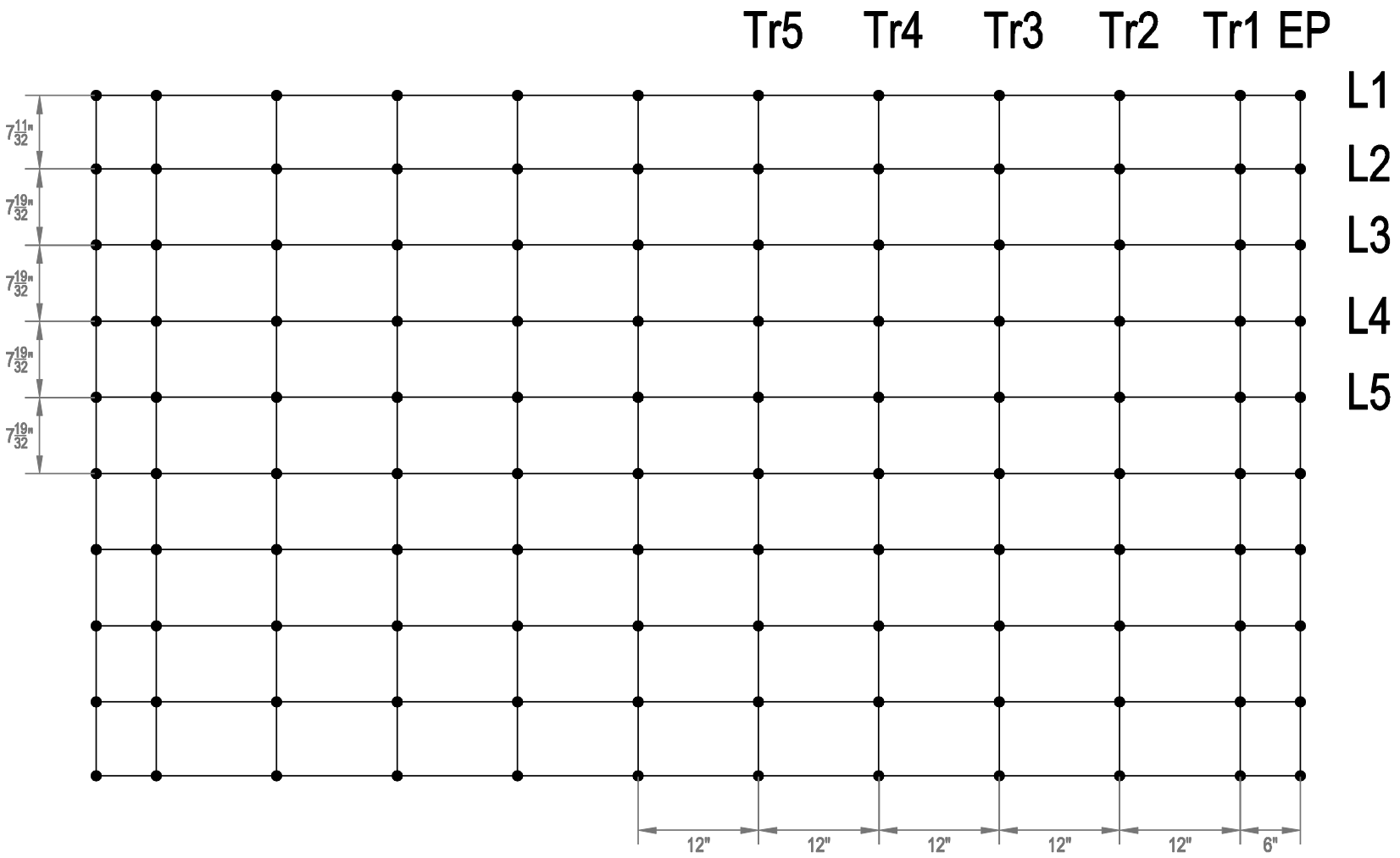

Figure 4. Grillage model of the V2 deck

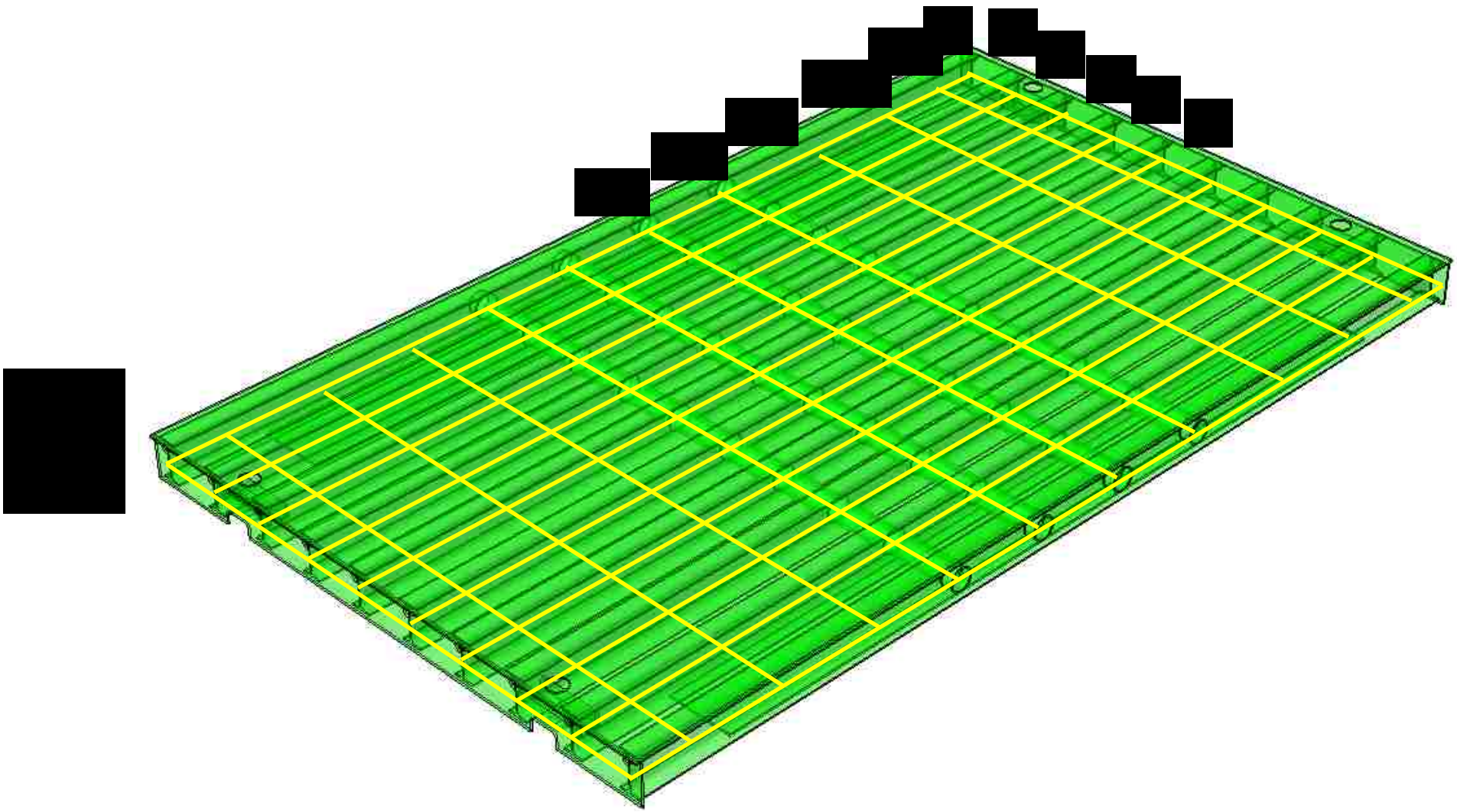

Figure 5. Grillage layout overlaid on temporary bridge deck

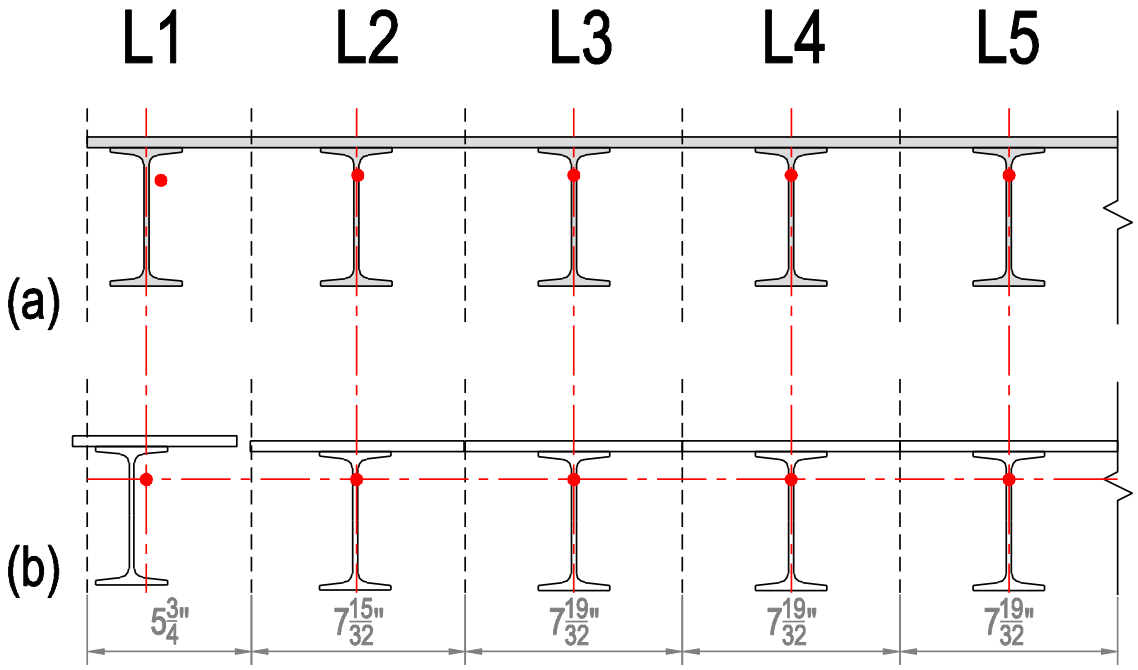

Figure 6. Division of bridge deck into longitudinal members (a) Longitudinal members without cover plate (b) Placement of sections in grillage layout

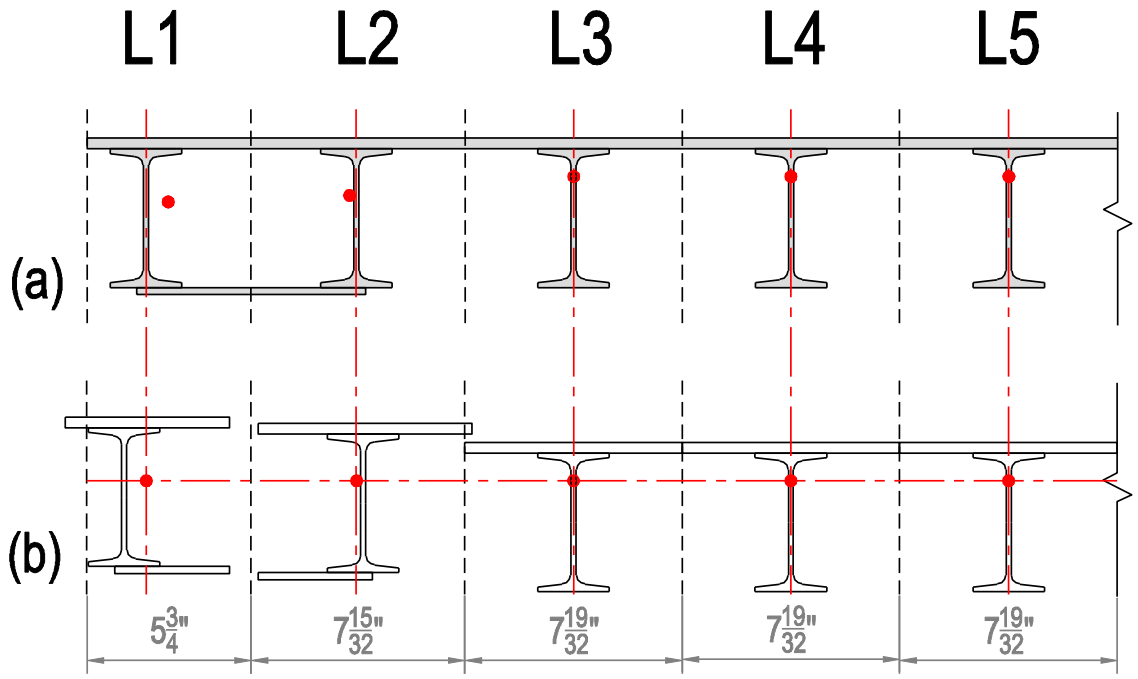

Figure 7. Division of bridge deck into longitudinal members (a) Longitudinal members with cover plate (b) Placement of sections in grillage layout

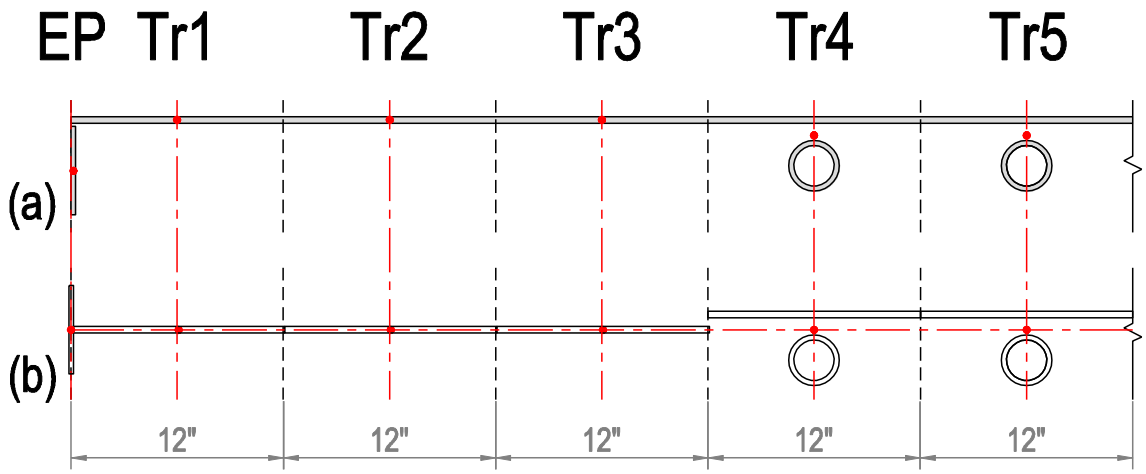

Figure 8. Division of bridge deck into transverse members (a) Transverse members without cover plate (b) Placement of sections in grillage layout

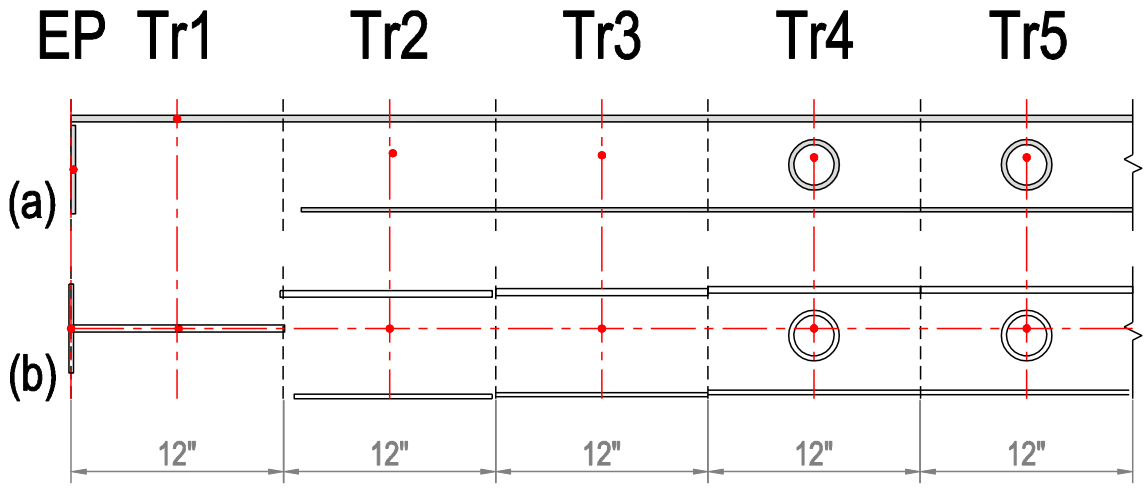

Figure 9. Division of bridge deck into transverse members (a) Transverse members with cover plate (b) Placement of sections in grillage layout

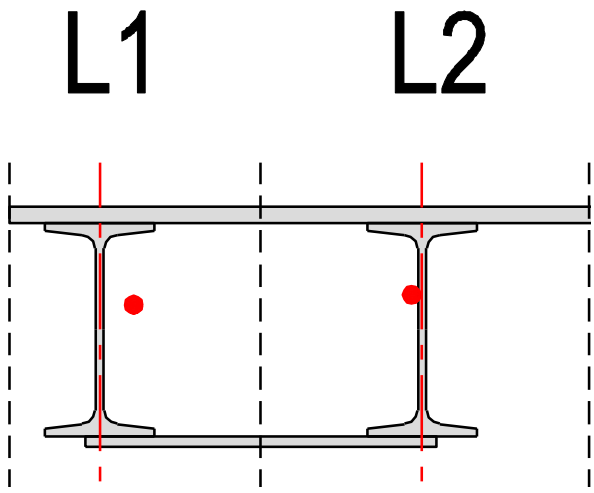

Figure 10. Closed beam section due to cover plate connection L1 and L2

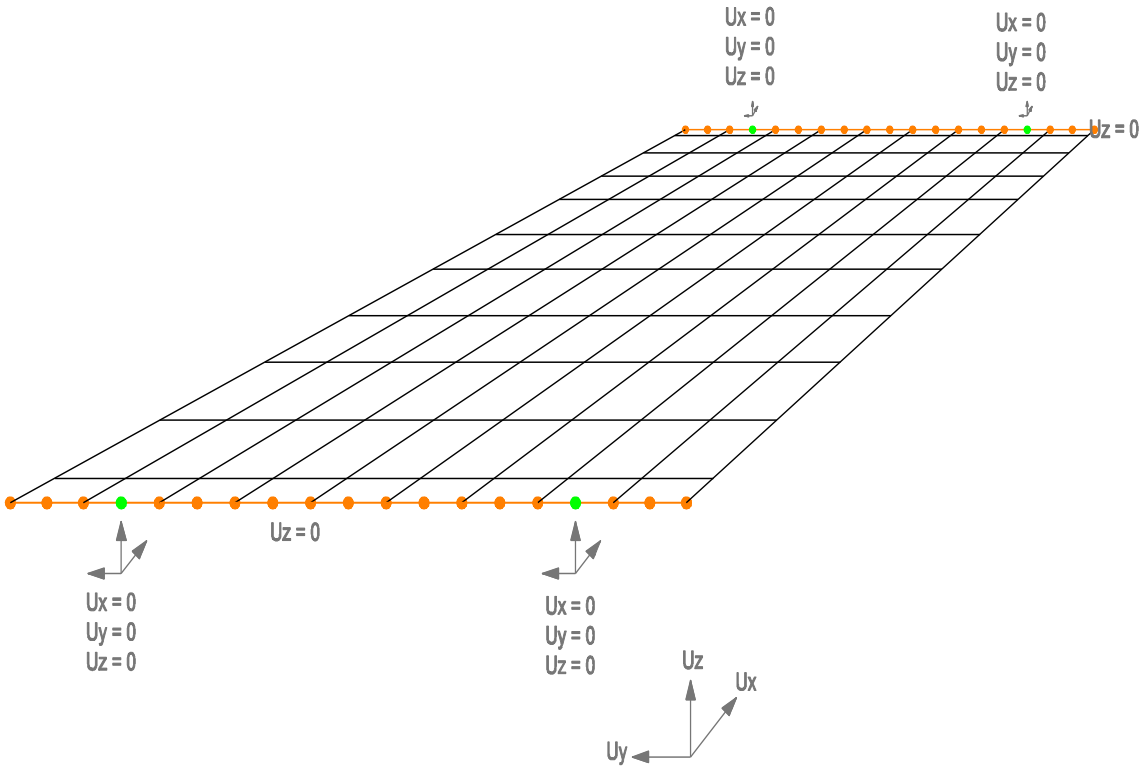

Figure 11. Boundary conditions on the grillage model

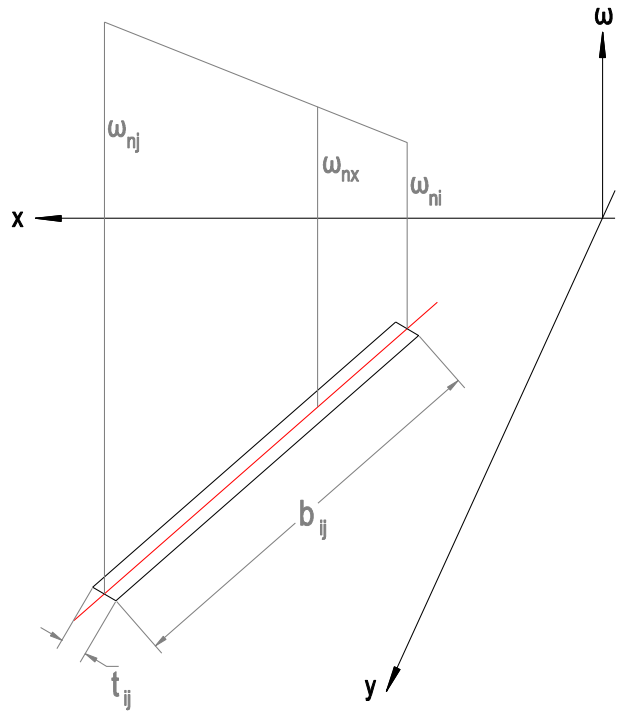

Figure 12. Variations of unit warping for a single plate

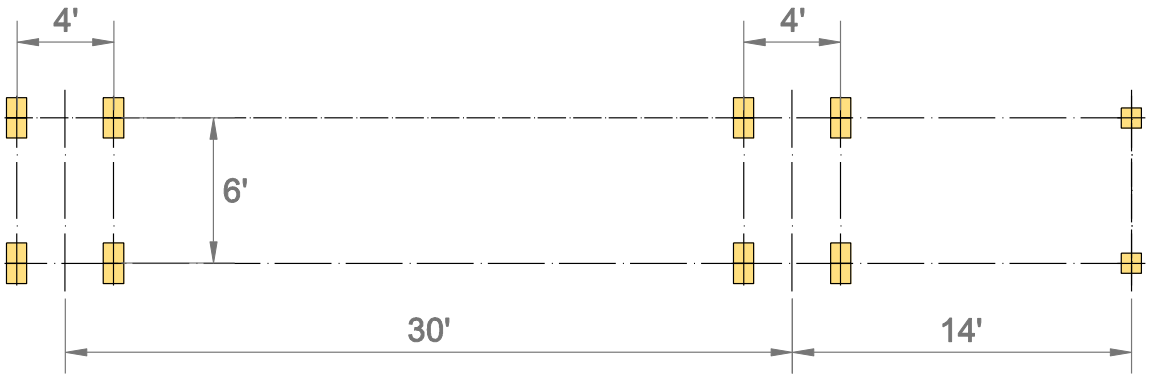

Figure 13. AASHTO LRFD BDS refined design truck footprint

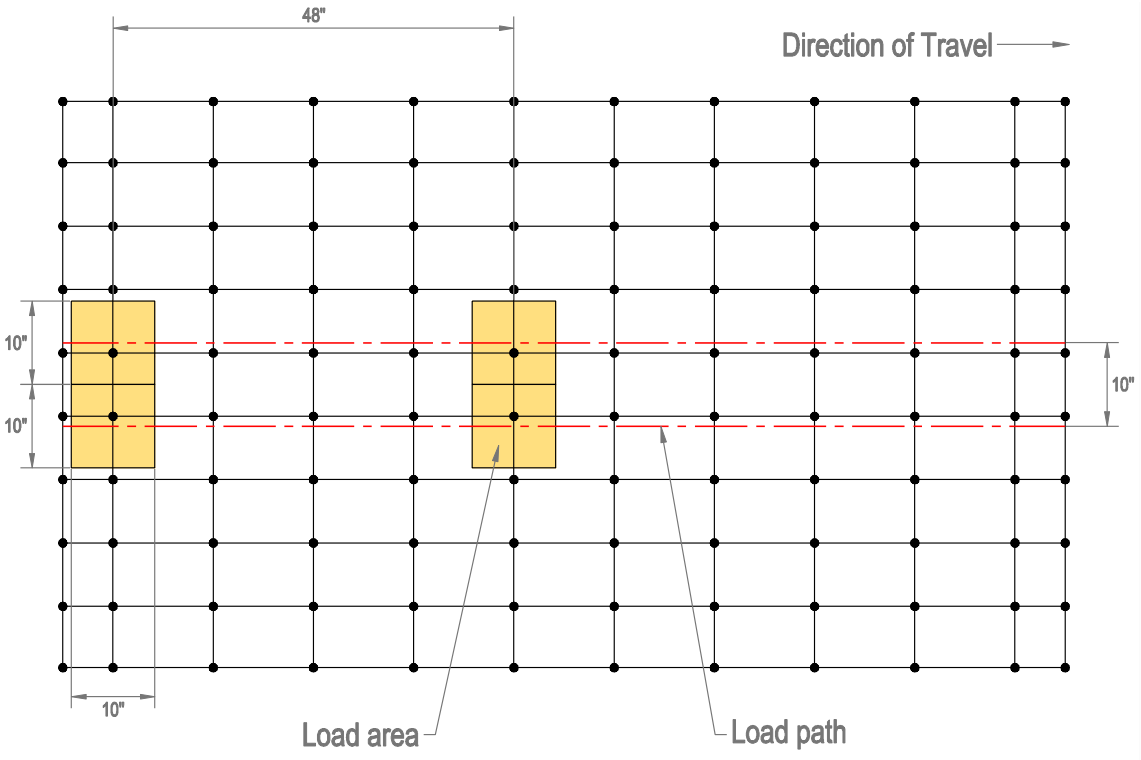

Figure 14. Load paths and load areas used in grillage model

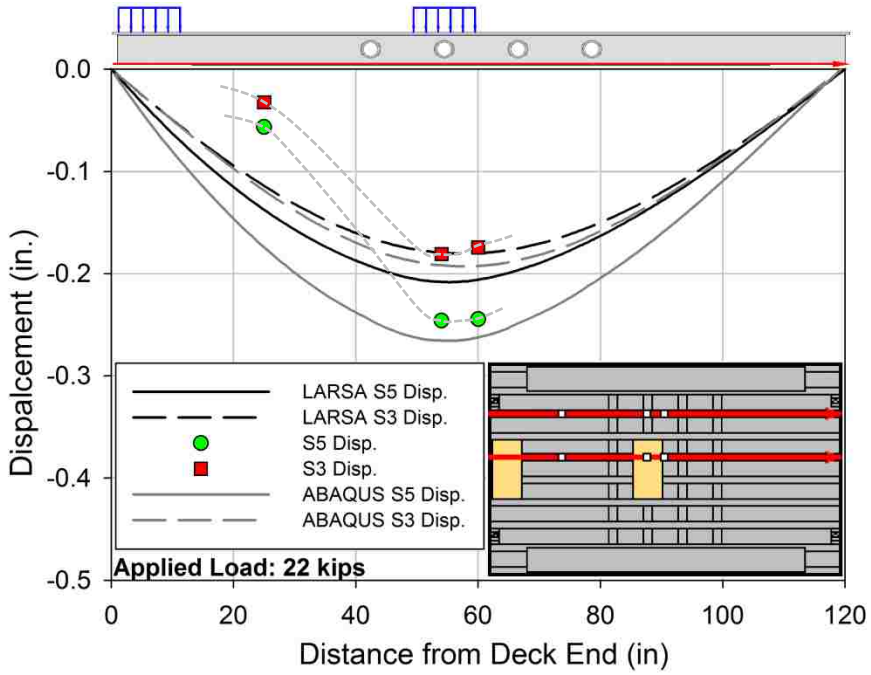

Figure 15. V1 Deck, grillage, and FEA displacement along stringers S5 and S3

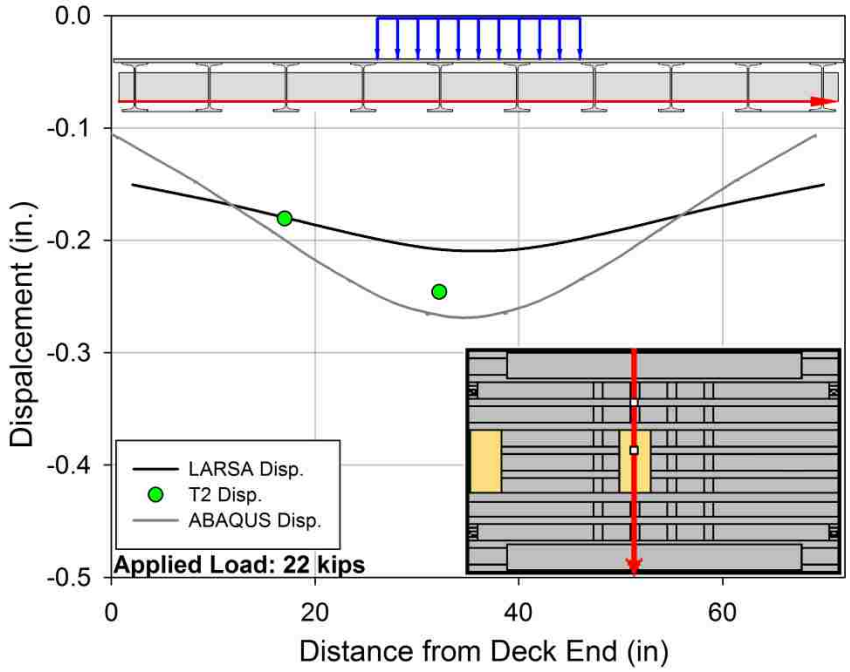

Figure 16. V1 Deck, grillage, and FEA displacement along tube T2

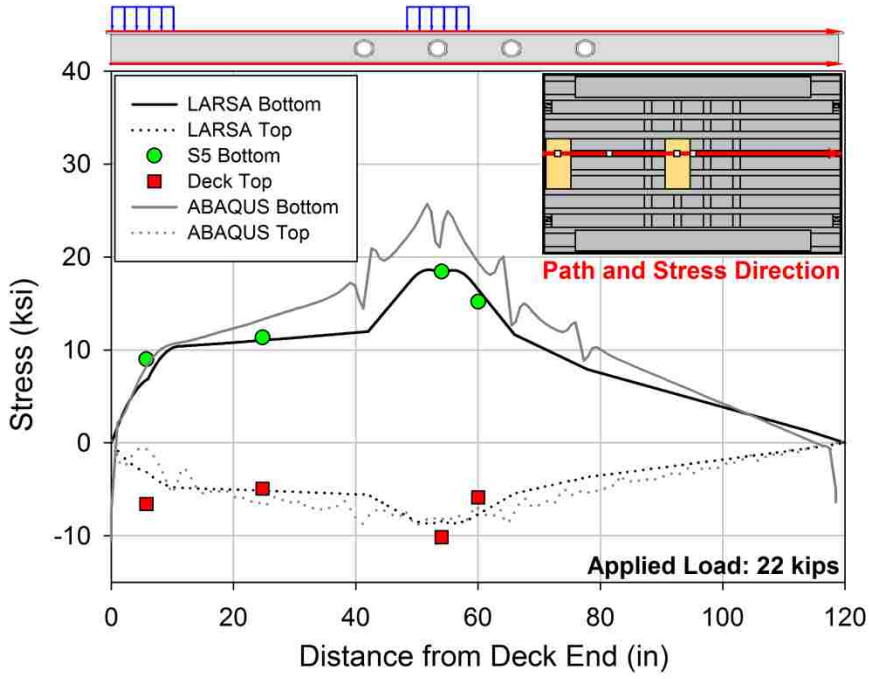

Figure 17. V1 Deck, grillage, and FEA stress along top and bottom of S5

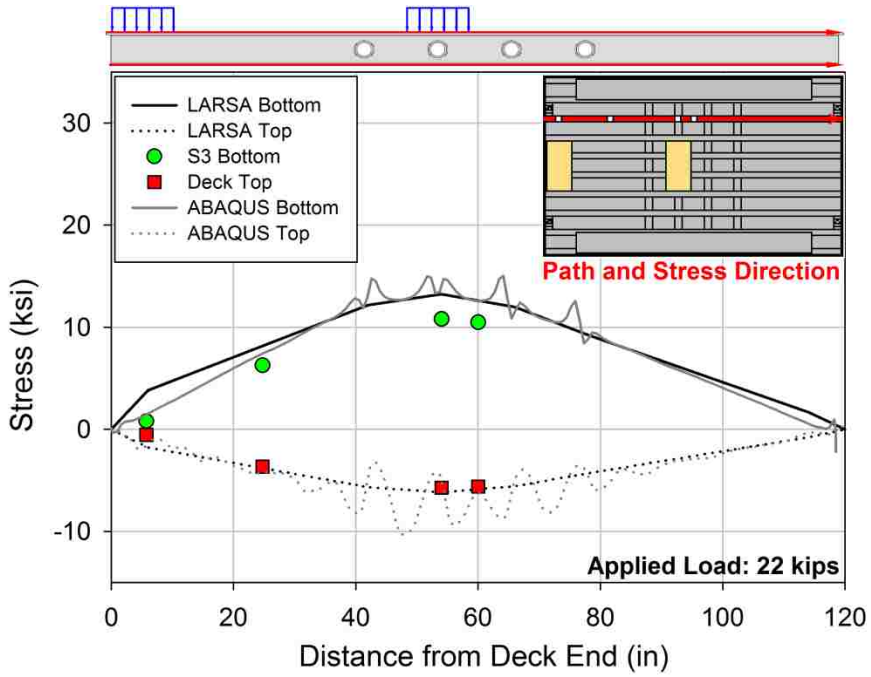

Figure 18. V1 Deck, grillage, and FEA stress along top and bottom of S3

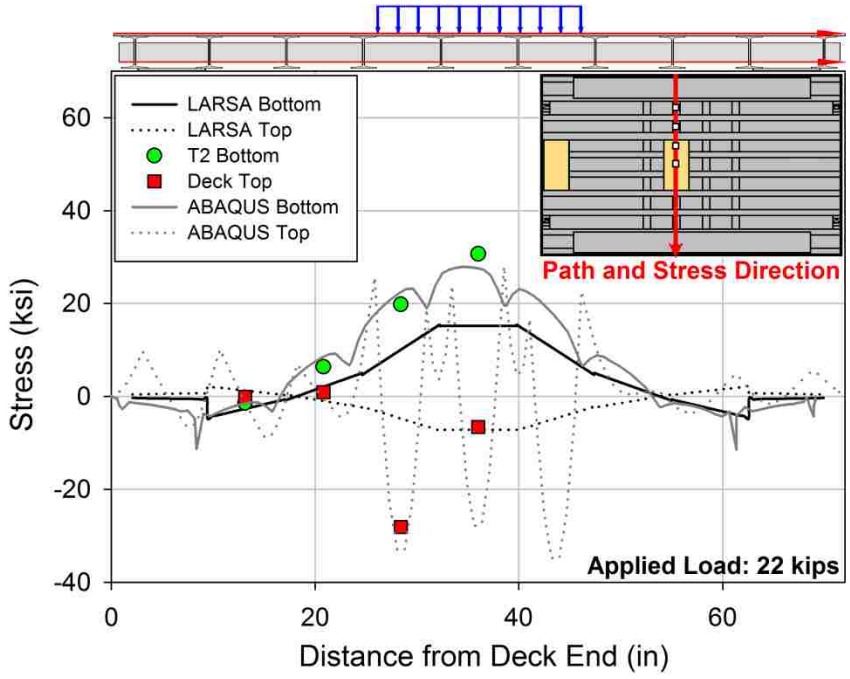

Figure 19. V1 Deck, grillage, and FEA stress along top and bottom of T2

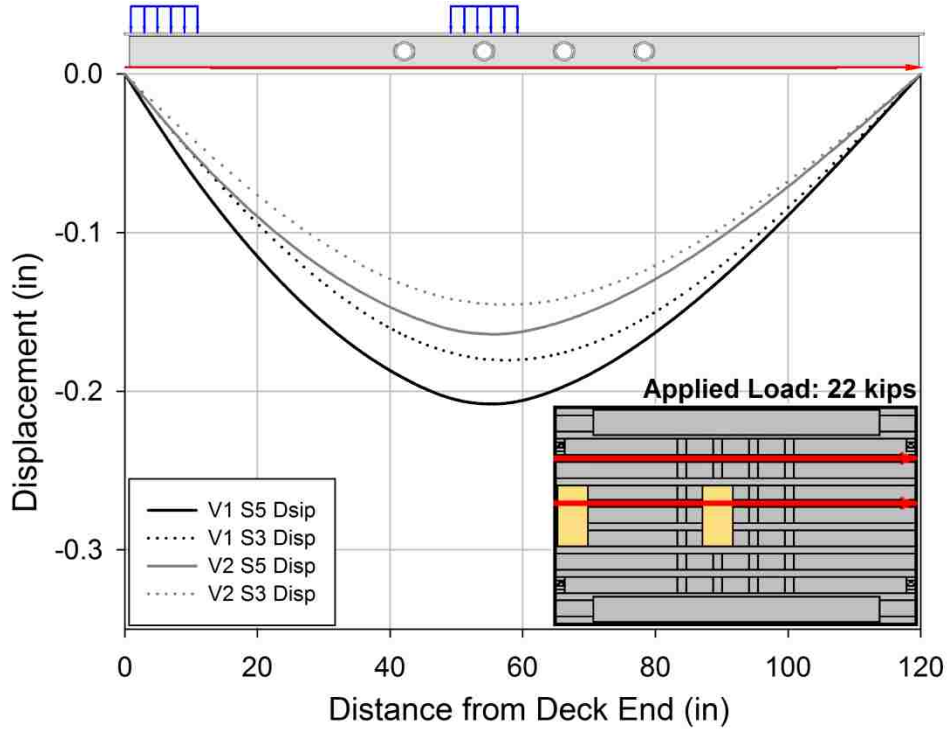

Figure 20. V1 and V2 grillage displacement along S5 and S3

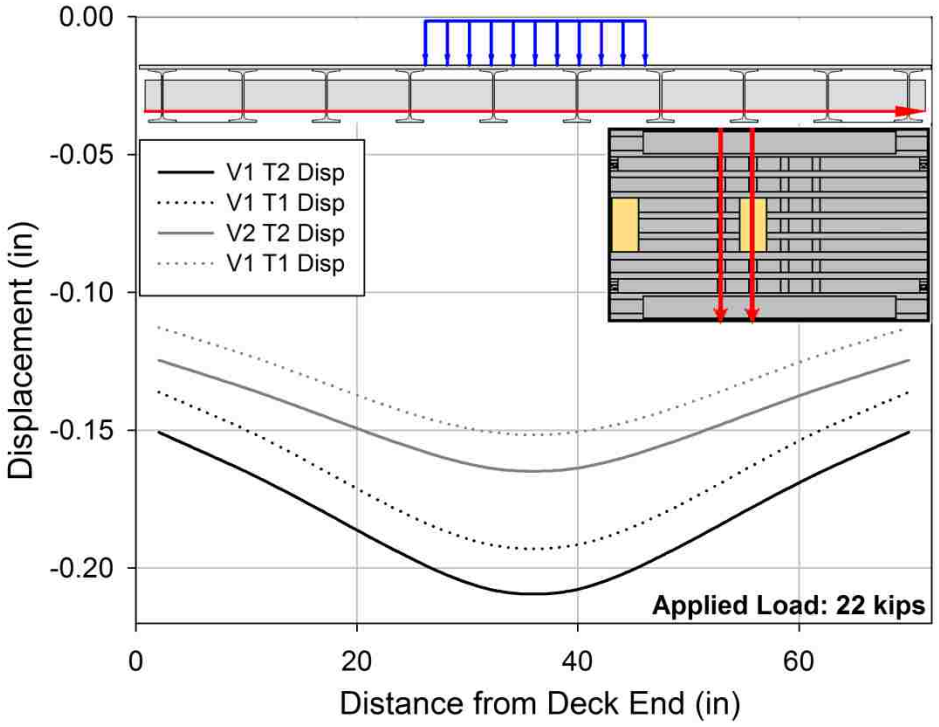

Figure 21. V1 and V2 grillage displacements along T2 and T1

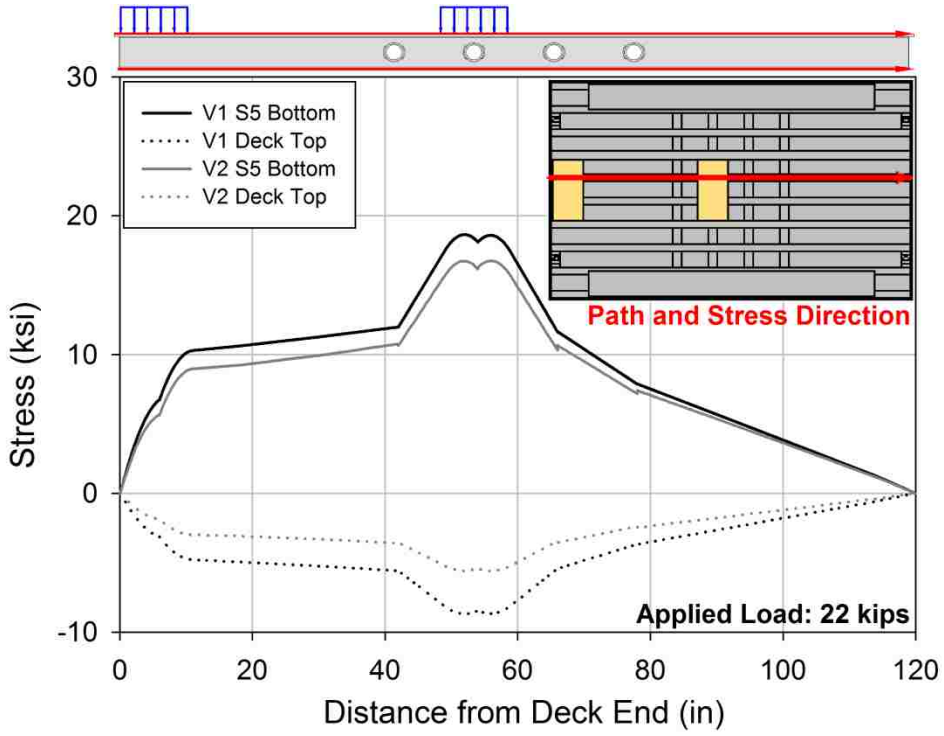

Figure 22. V1 and V2 grillage stress along top and bottom of S5

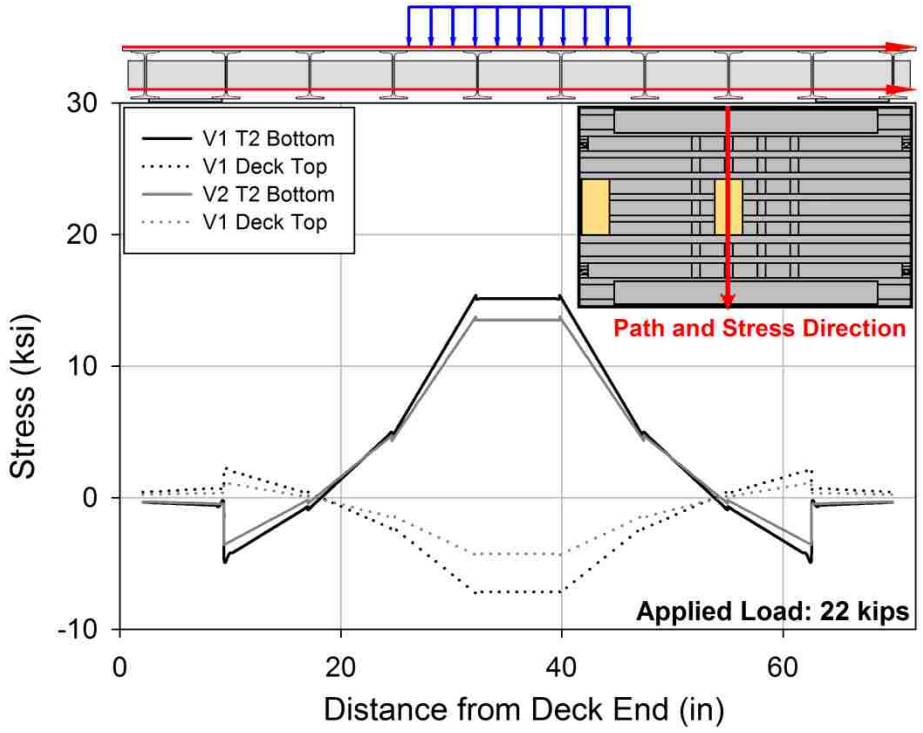

Figure 23. V1 and V2 grillage stress along top and bottom of T2

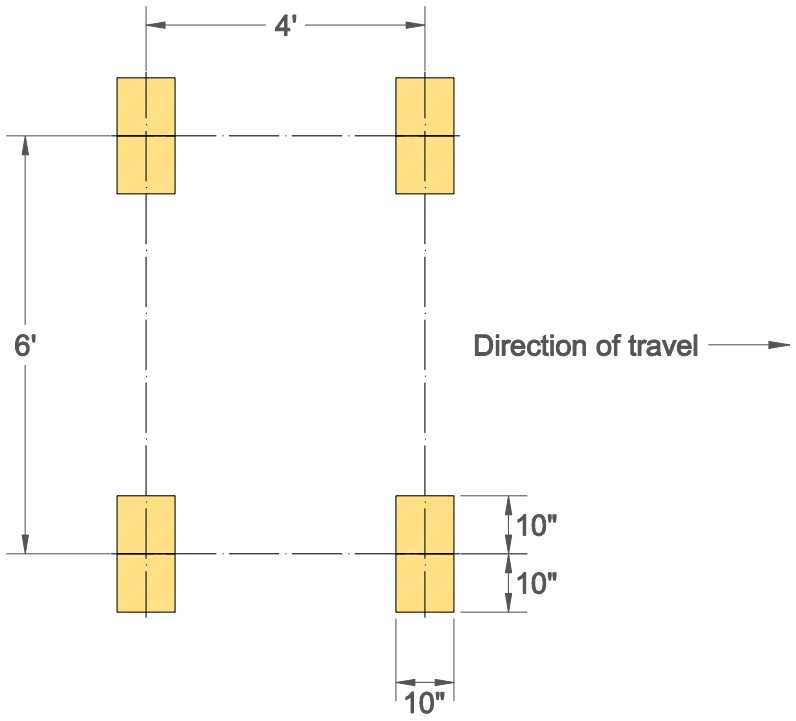

Figure 24. Footprint of the design truck tandem axel as per the AASHTO LRFD BDS

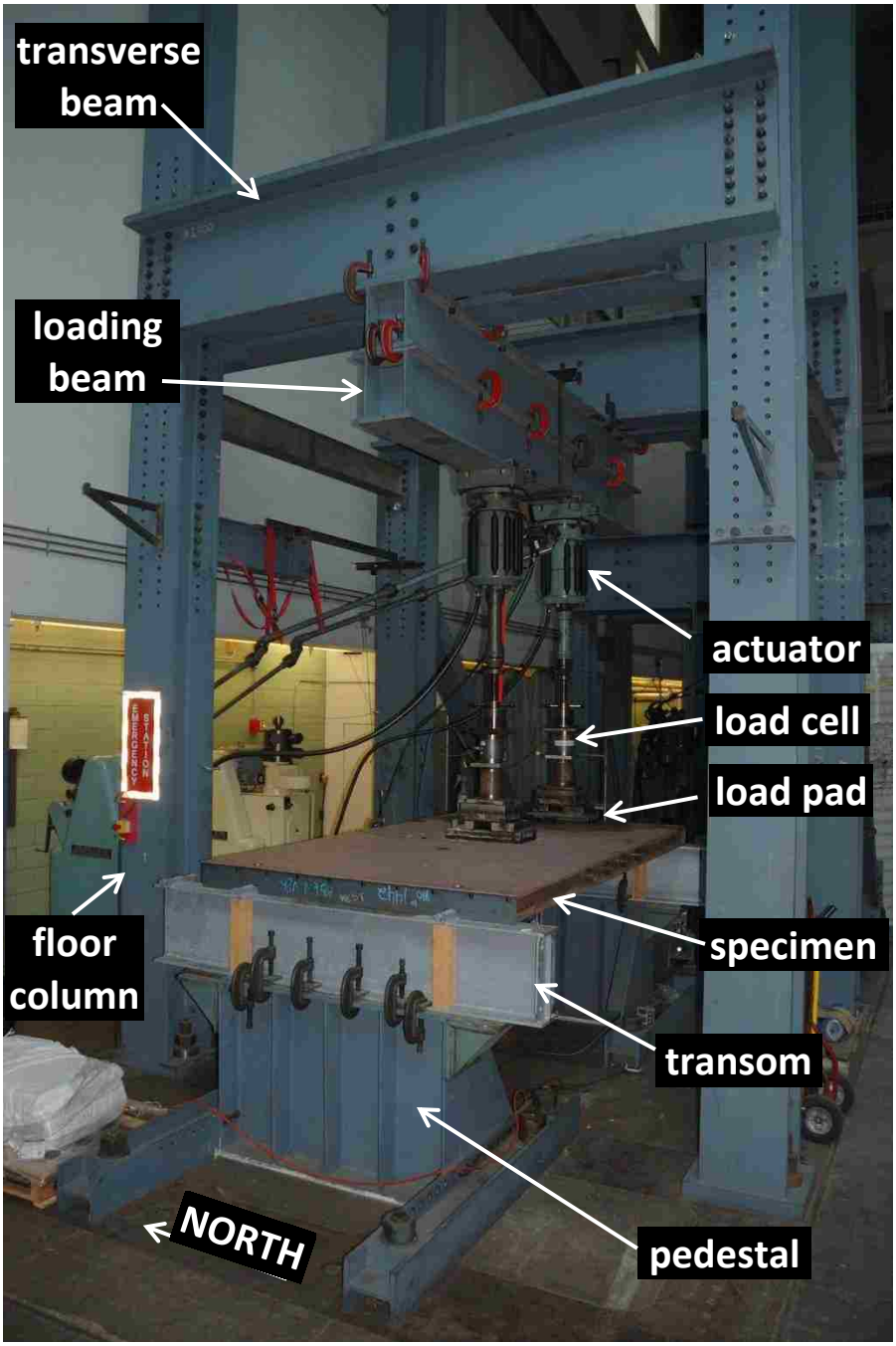

Figure 25. Test setup in the Fritz Laboratory, looking south-west to north-east

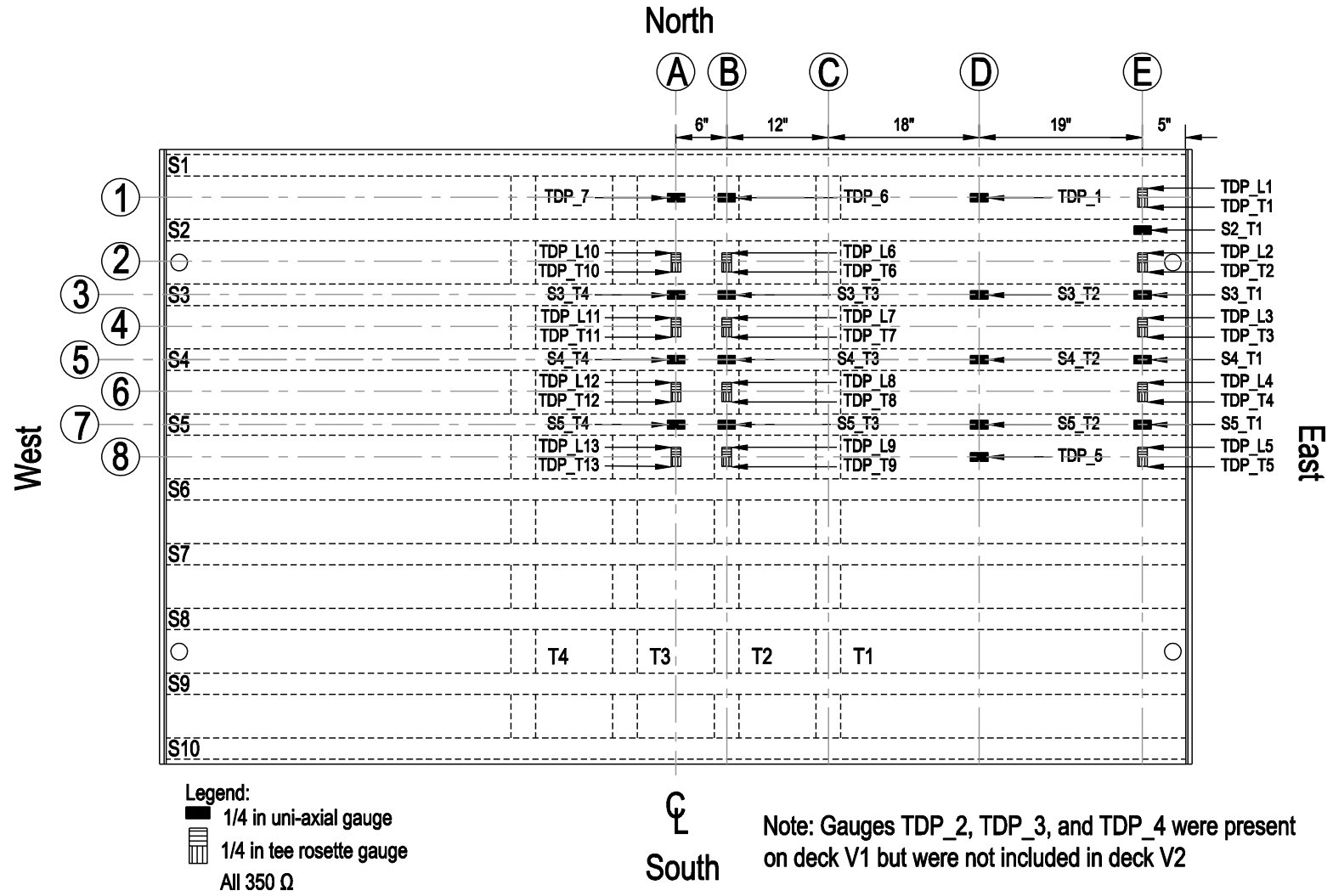

Figure 26. Strain gauge layout for Specimen #1 on top of deck plate

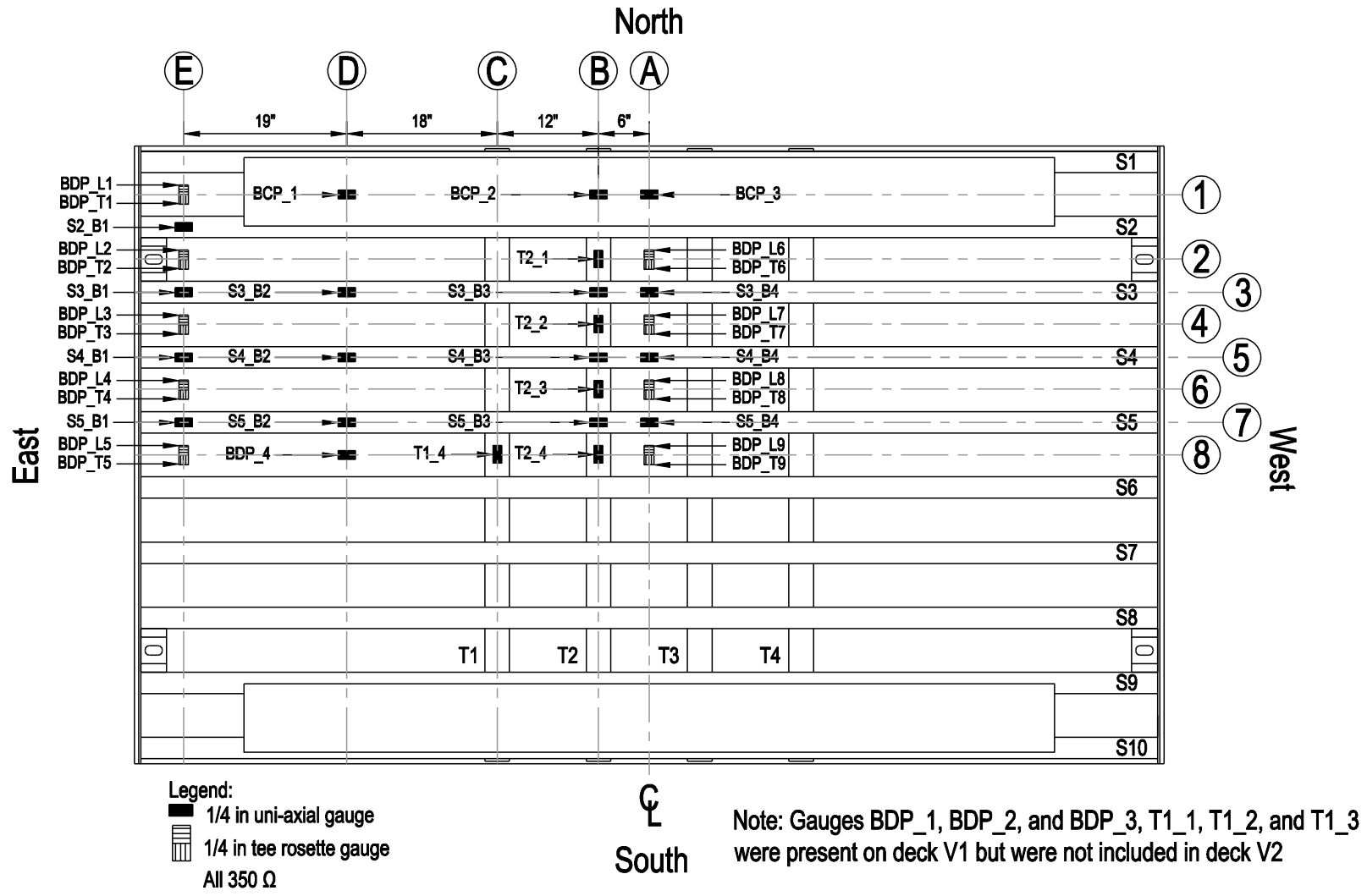

Figure 27. Strain gauge layout for Specimen #1 on underside of deck

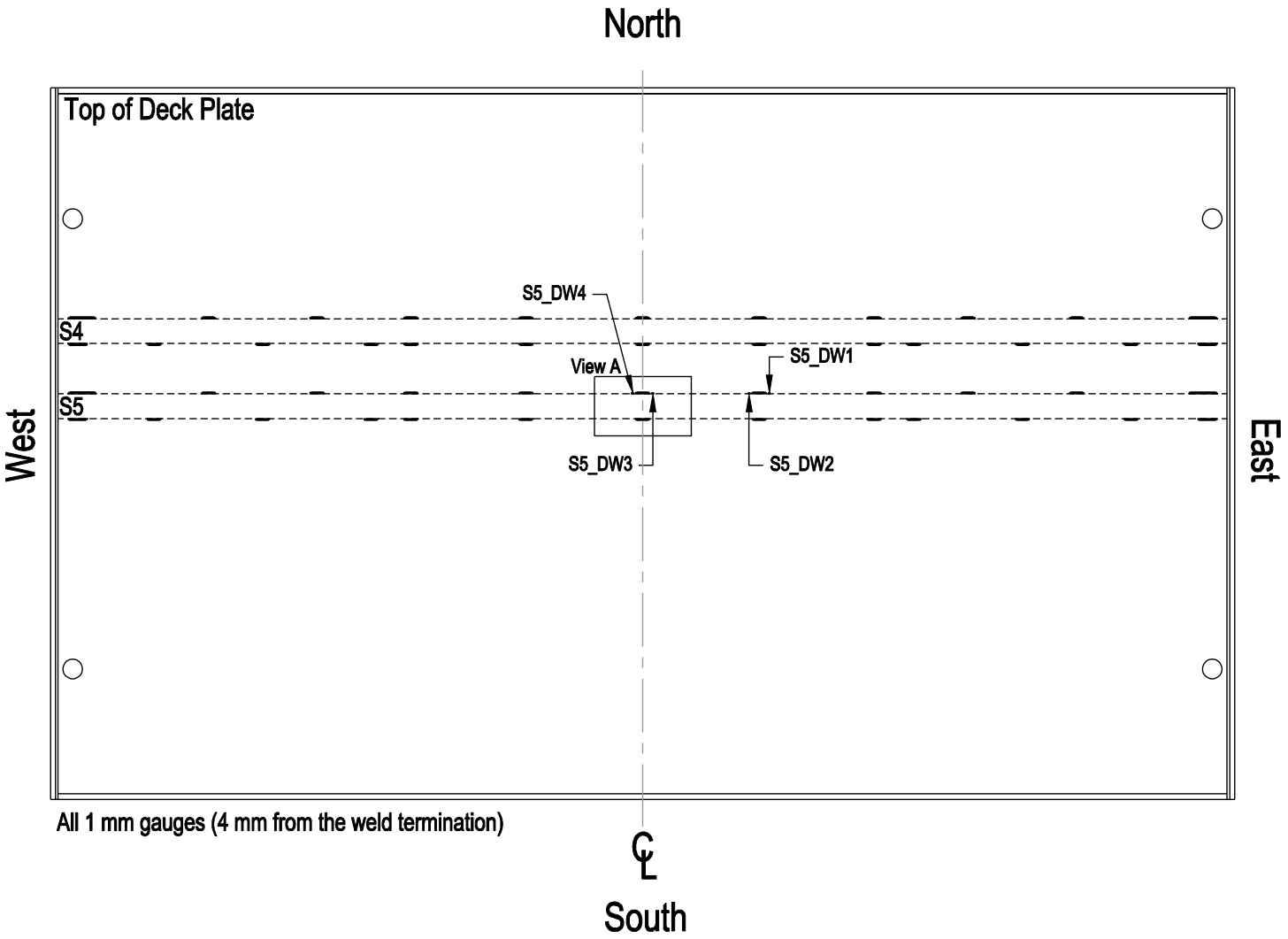

Figure 28. Strain gauge layout for Specimen #1 of stringer-to-deck welds

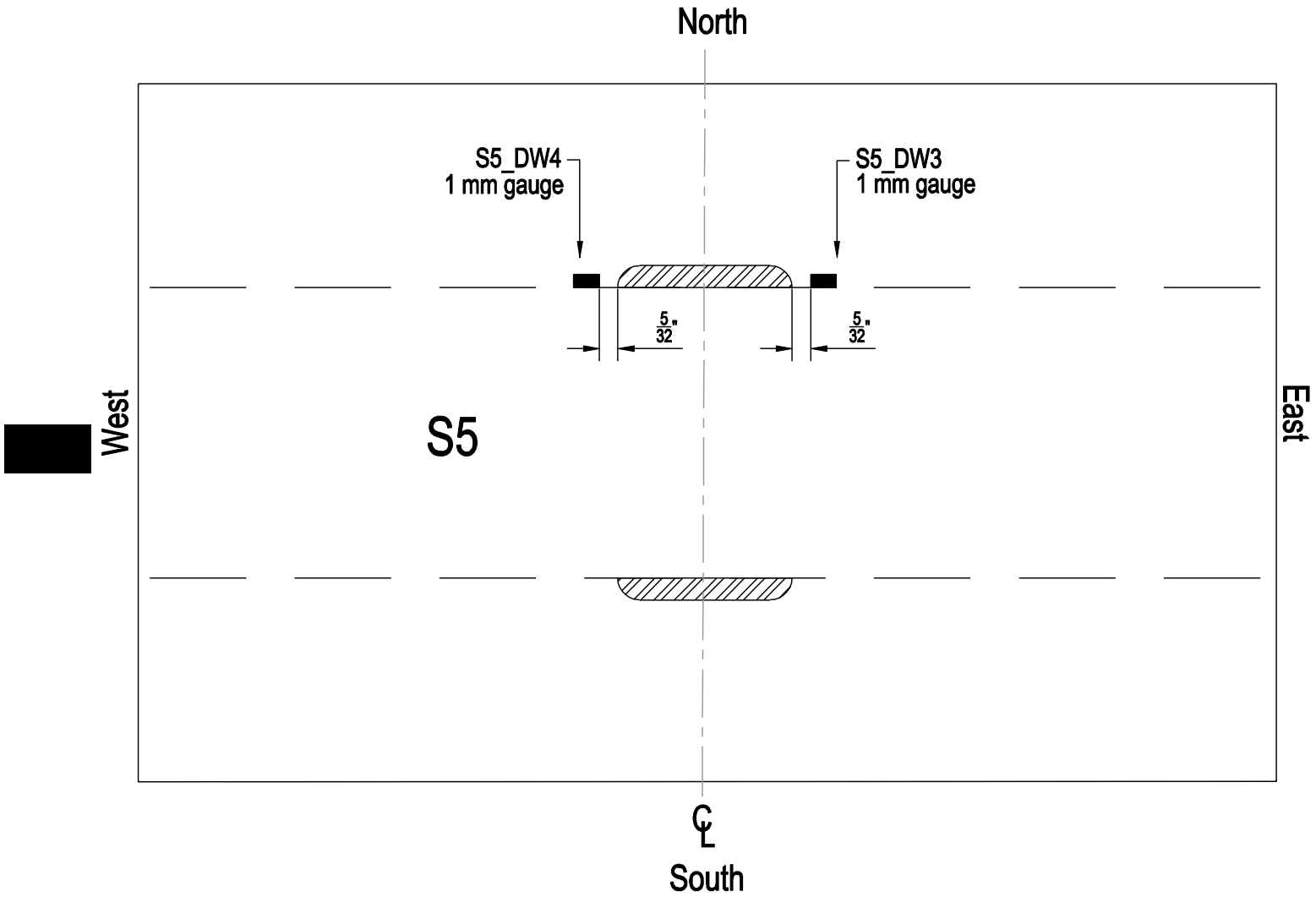

Figure 29. Enlarged view A of Figure 5, strain gauge layout for Specimen #1 of stringer-to-deck welds

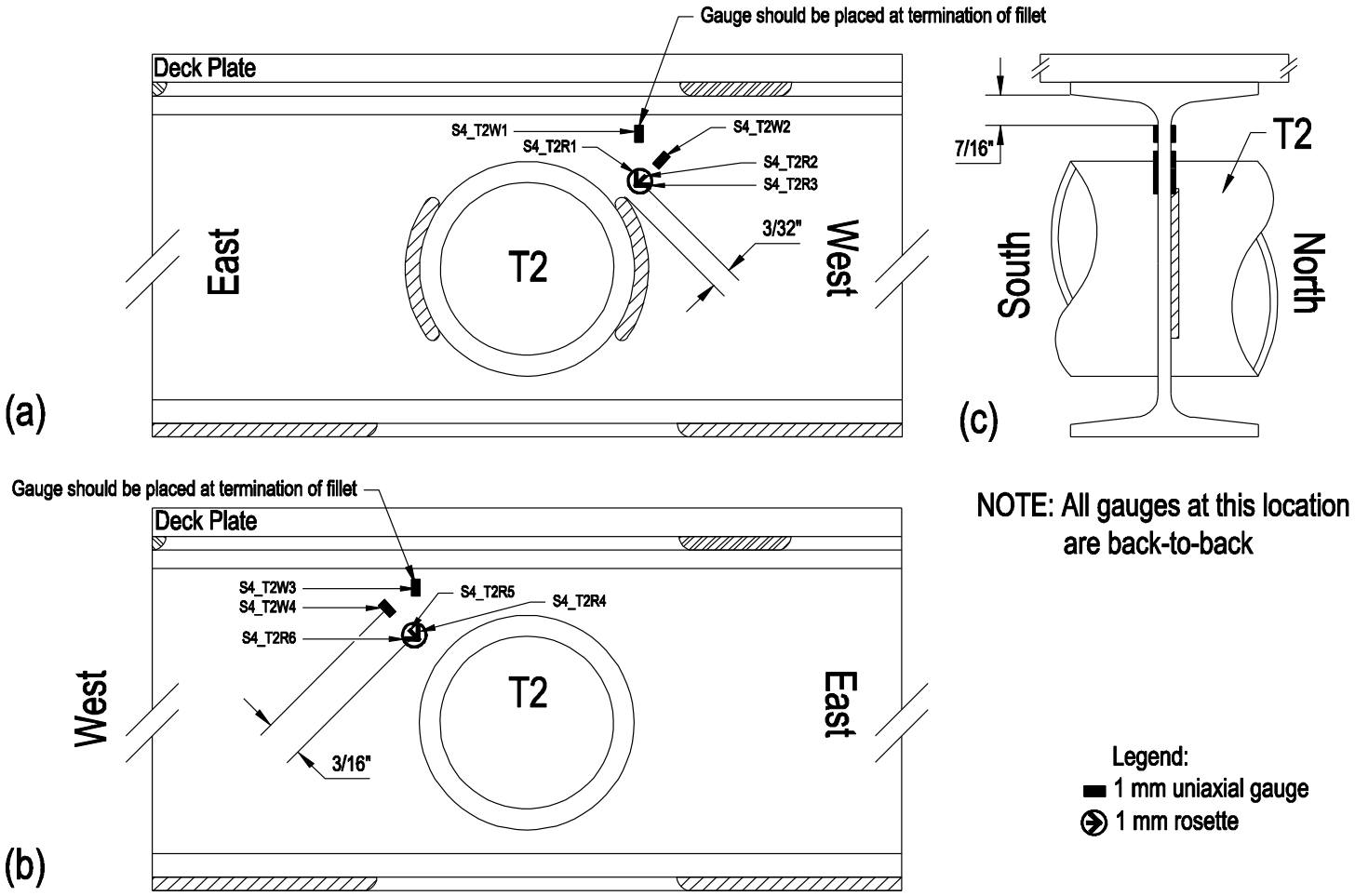

Figure 30. Strain gauge layout at S4-to-T2 connection for specimens #1 and #2: (a) part north elevation, (b) part south elevation, (c) section view

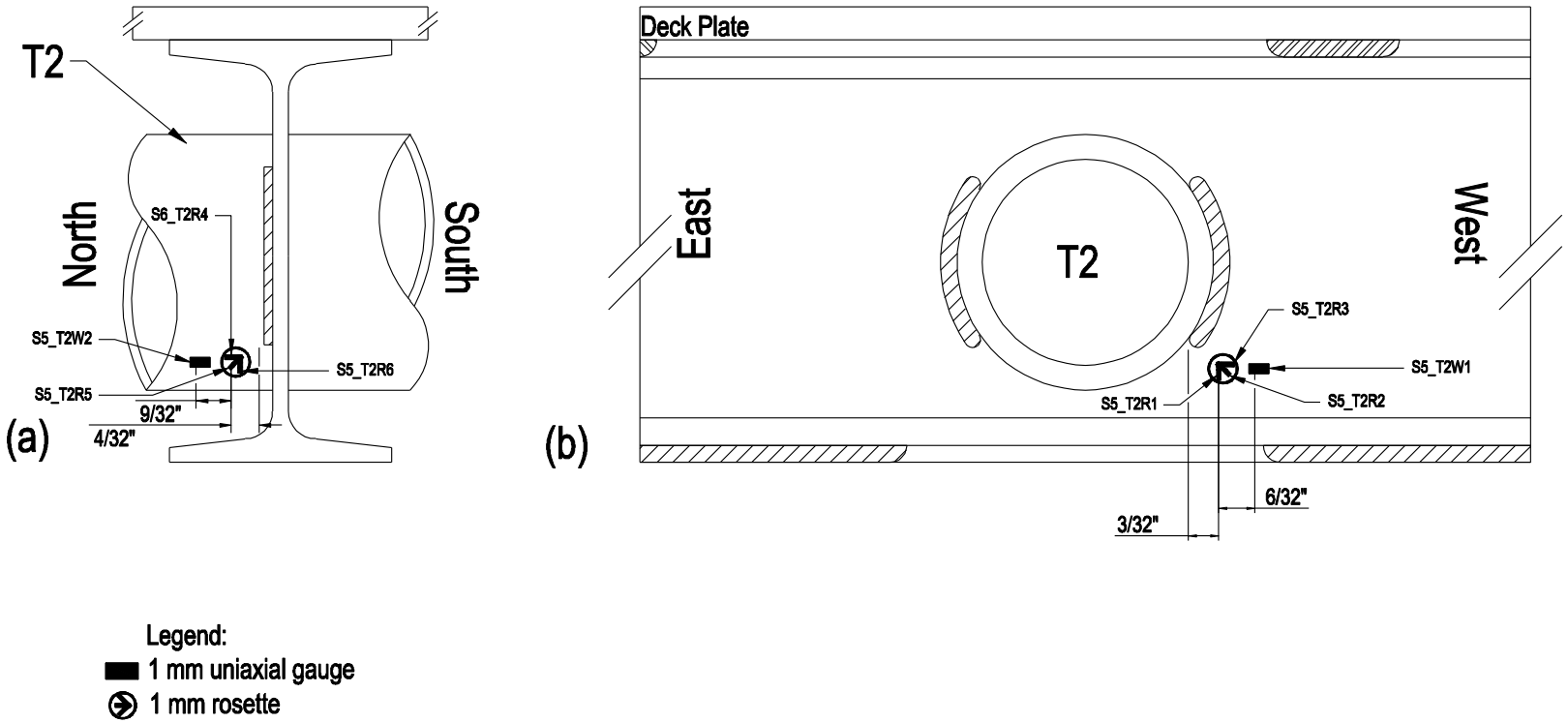

Figure 31. Strain gauge layout at S5-to-T2 connection for Specimen #1: (a) section view, (b) part north elevation

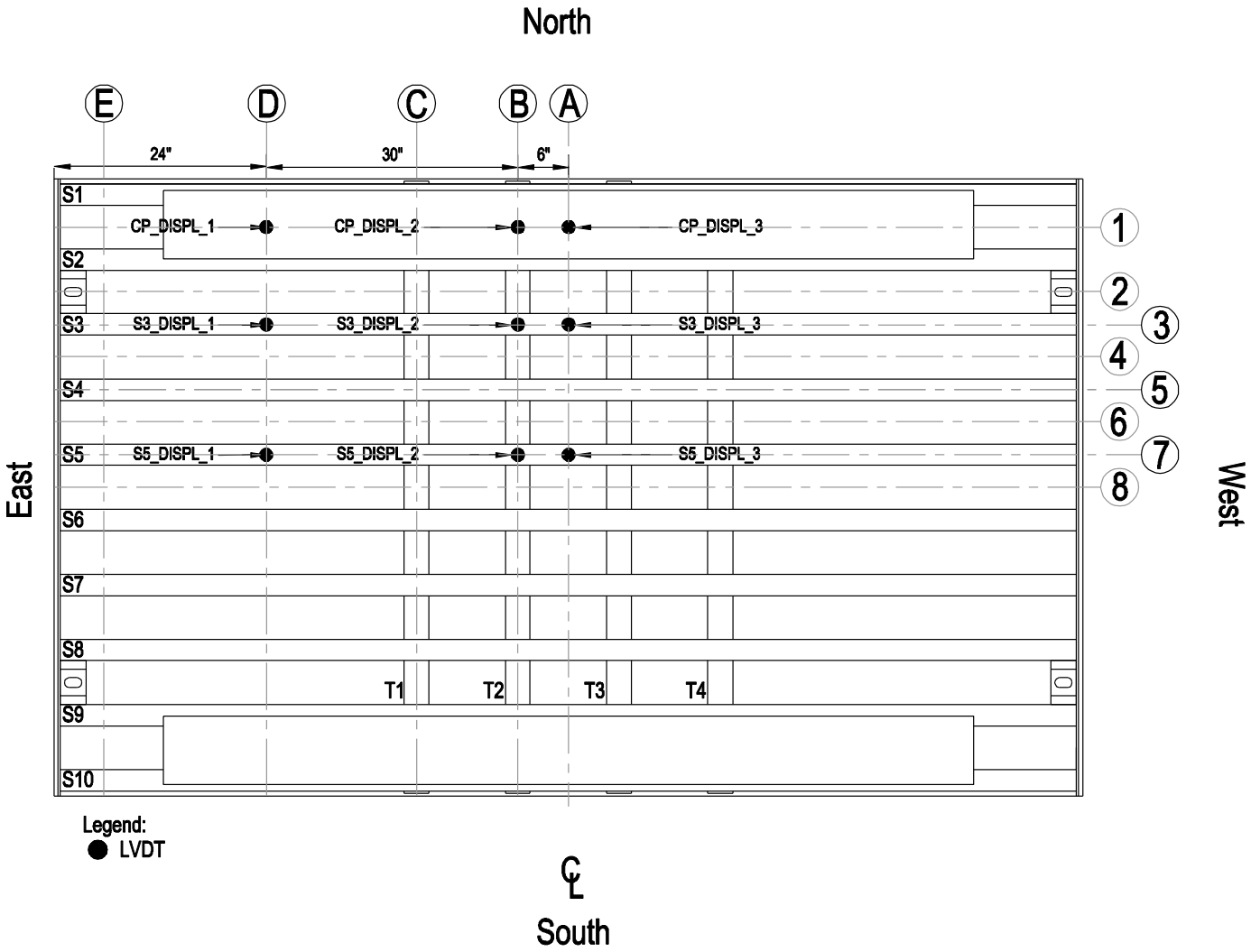

Figure 32. LVDT layout of specimens #1 and #2

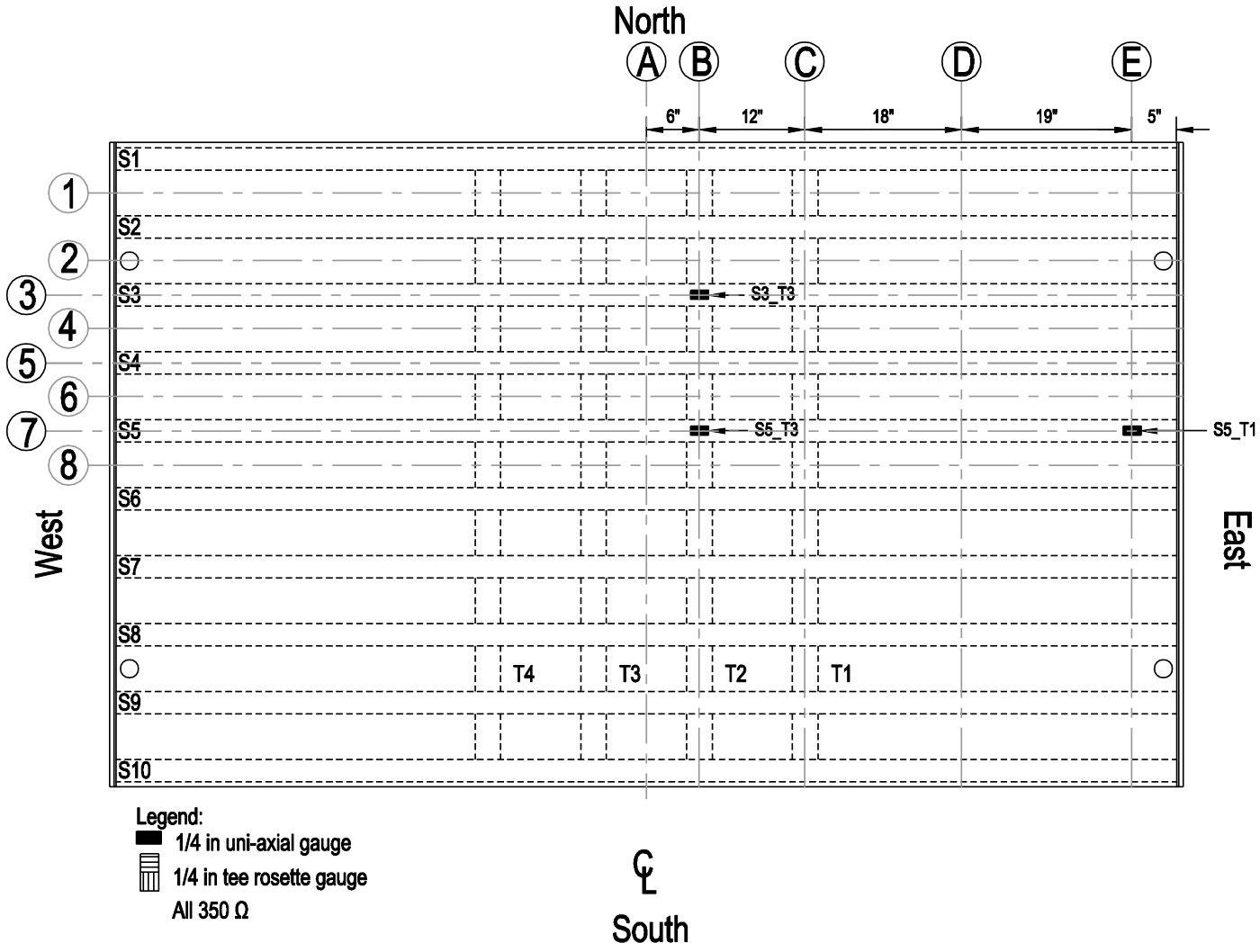

Figure 33. Strain gauge layout for Specimen #2 on top of deck plate

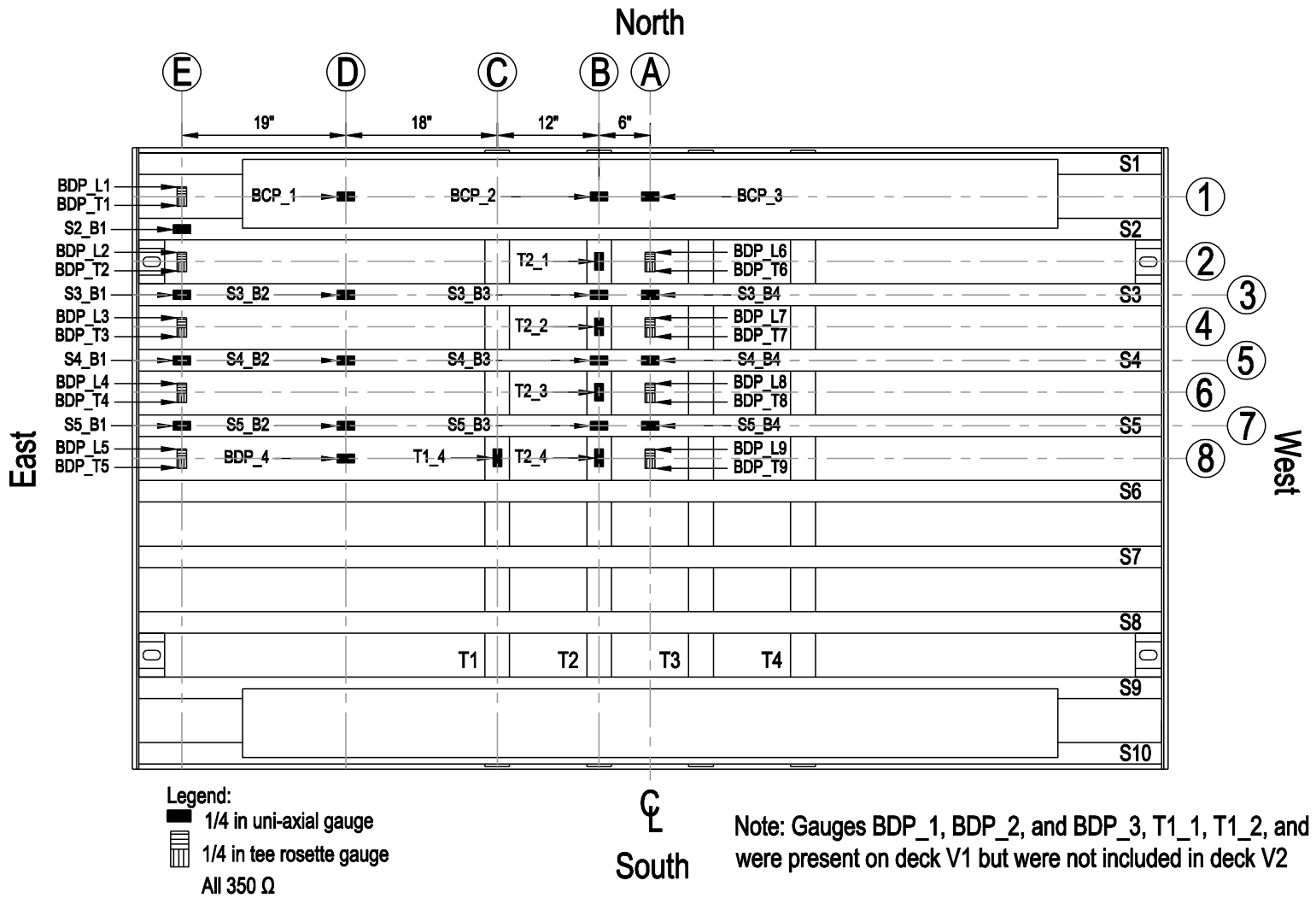

Figure 34. Strain gauge layout for Specimen #2 on bottom of deck plate

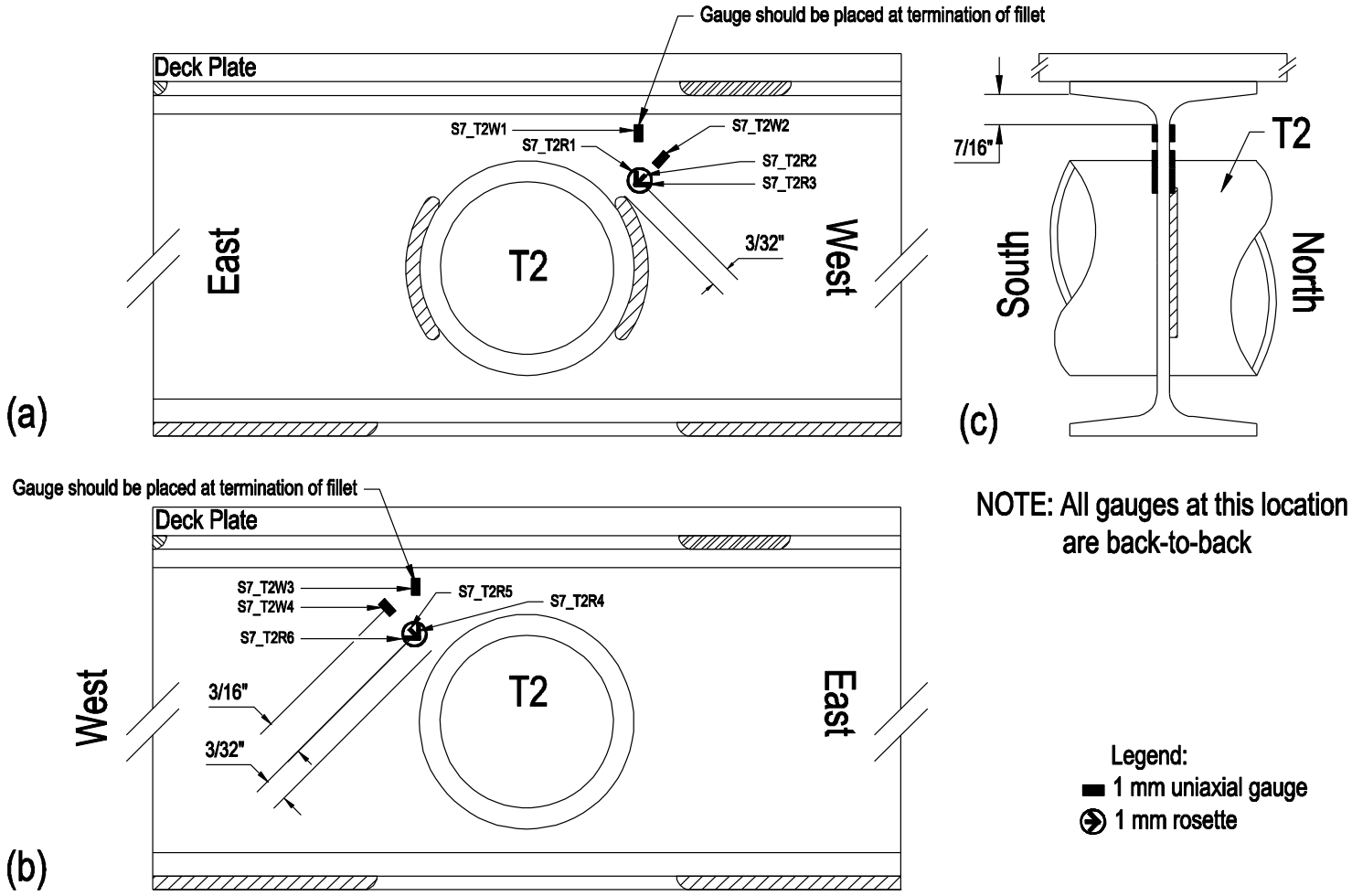

Figure 35. Strain gauge layout of at S7-to-T2 connection for Specimen #2: (a) part north elevation, (b) part south elevation, (c) section view

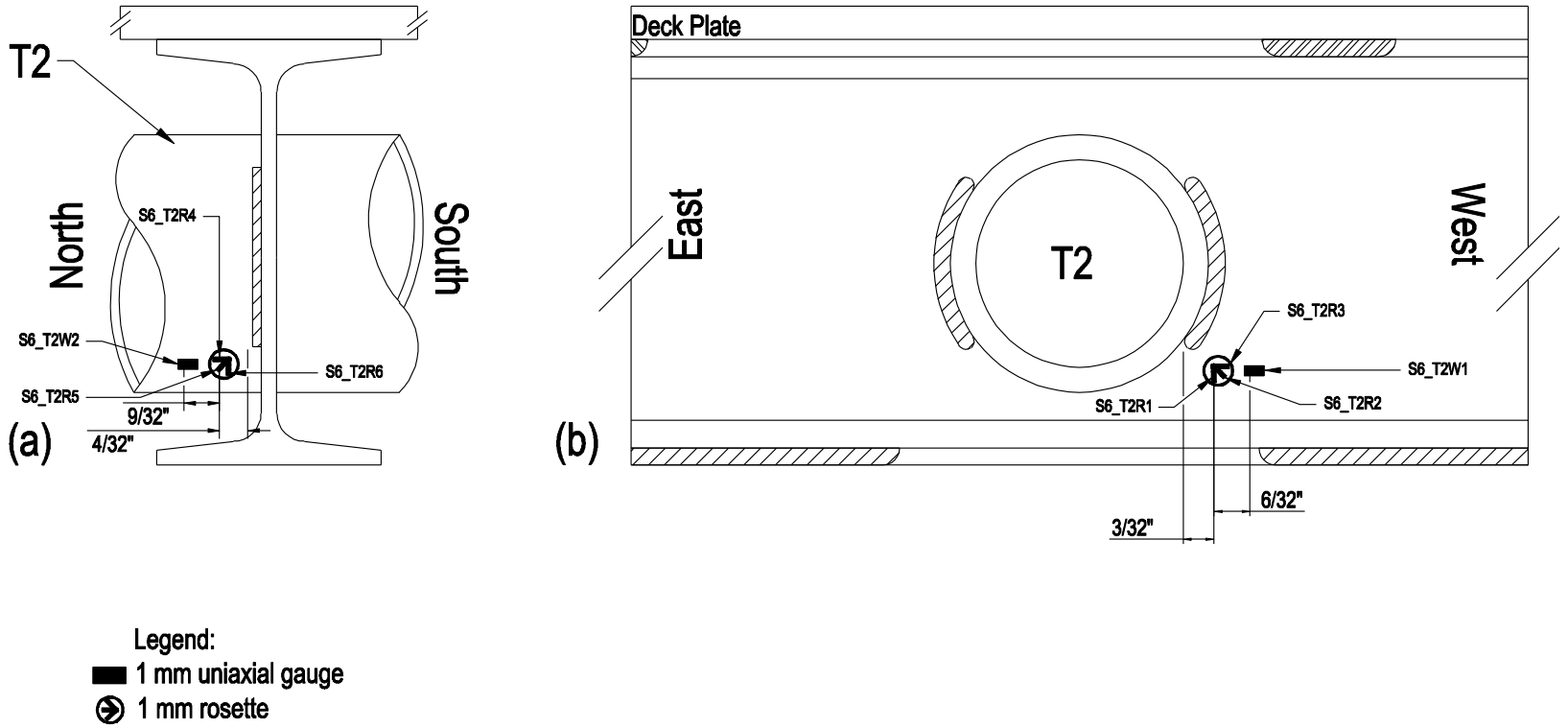

Figure 36. Strain gauge layout at S6-to-T2 connection for Specimen #2: (a) section view, (b) part north elevation

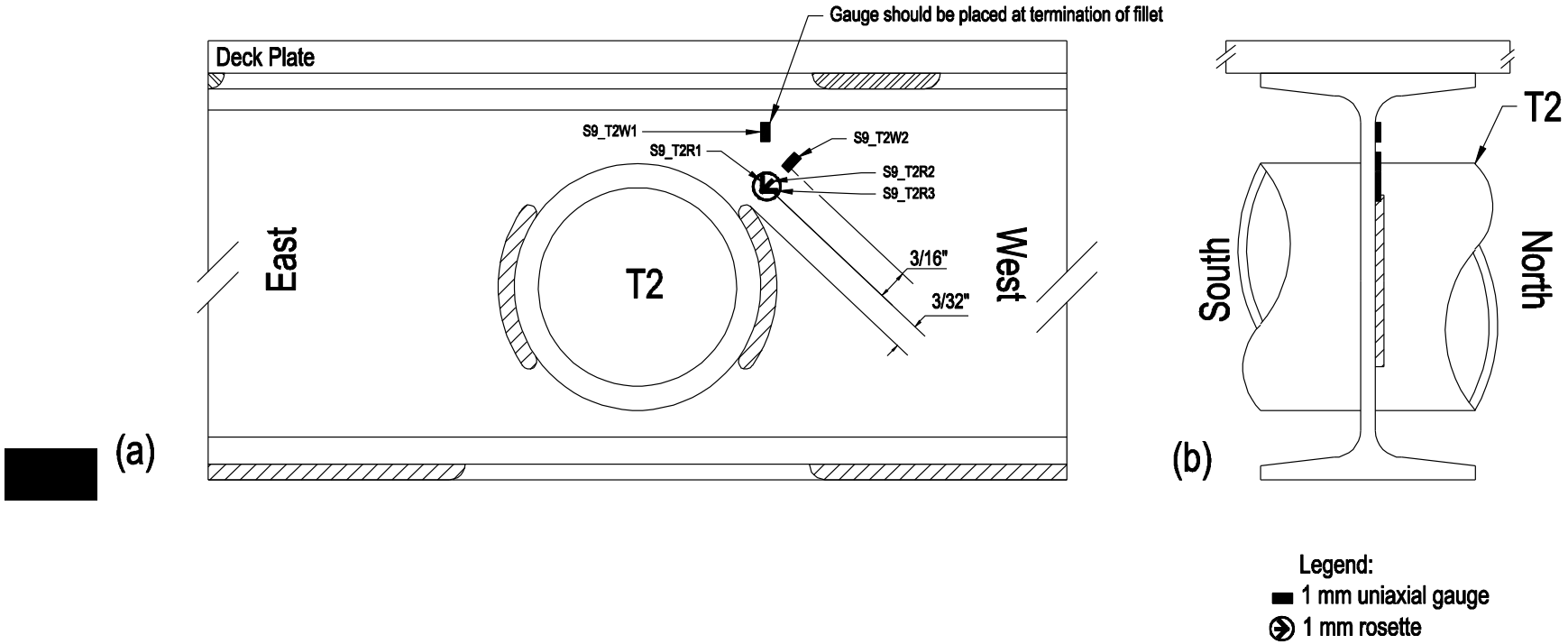

Figure 37. Strain gauge layout of at S9-to-T2 connection for Specimen #2: (a) part north elevation, (b) section view

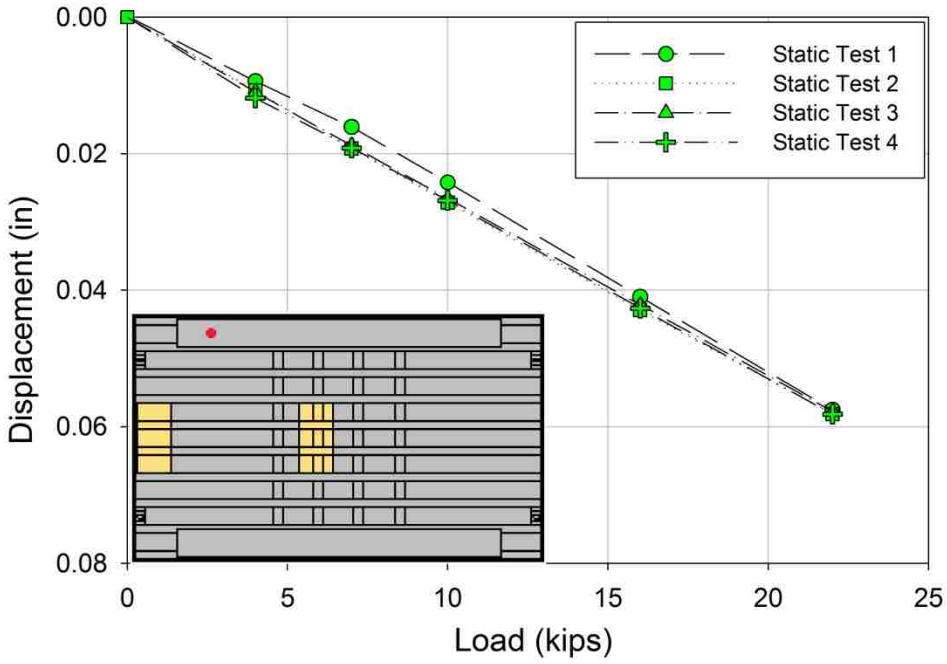

Figure 38. Specimen #1, measurements at LVDT CP_DISPL_1

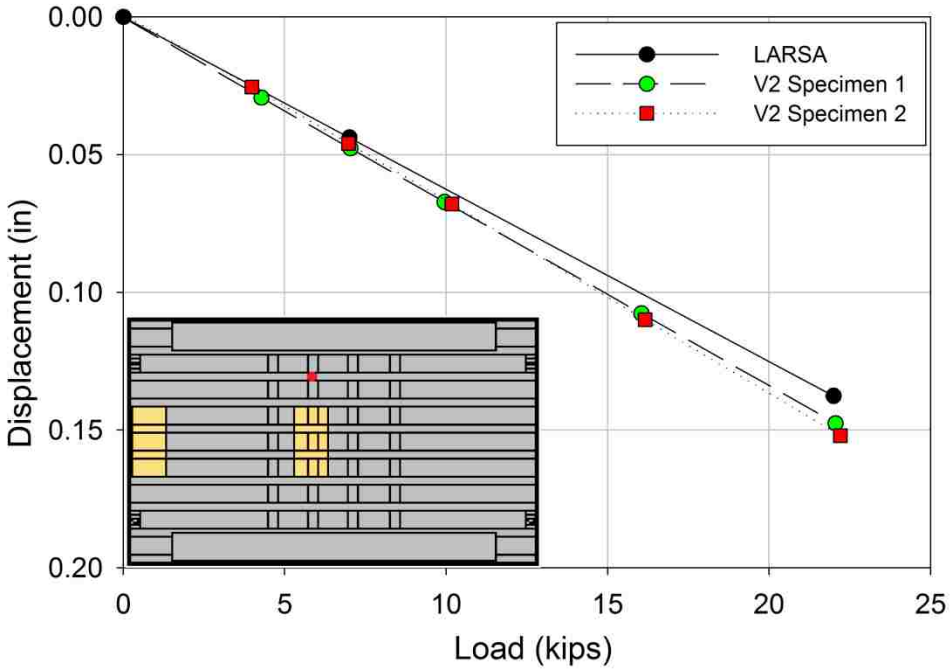

Figure 39. All specimens, measurements at LVDT S3_DISPL_2

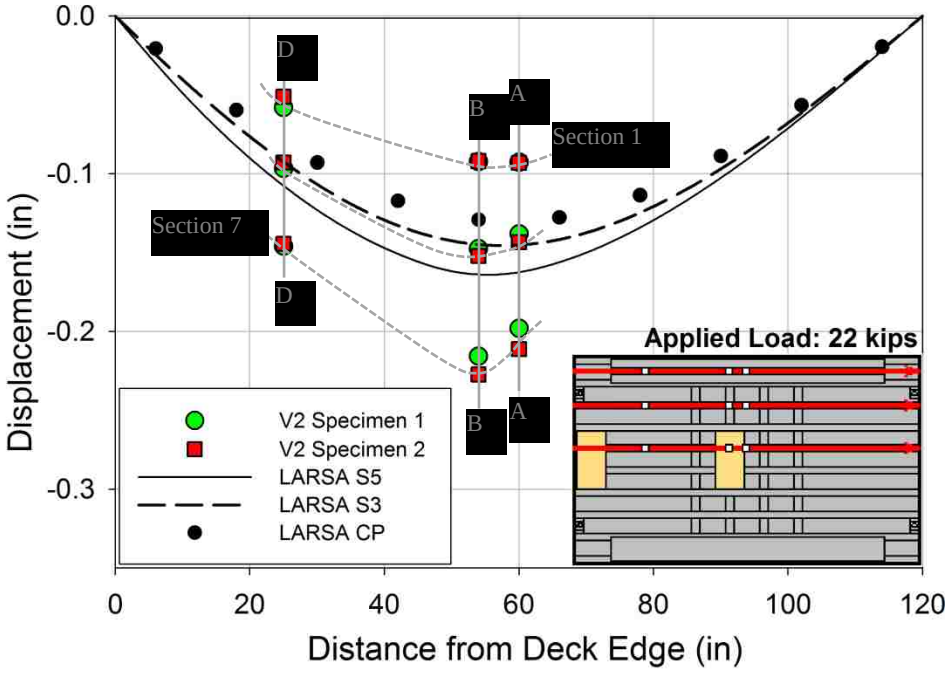

Figure 40. Displacement along longitudinal sections 1, 3 and 7

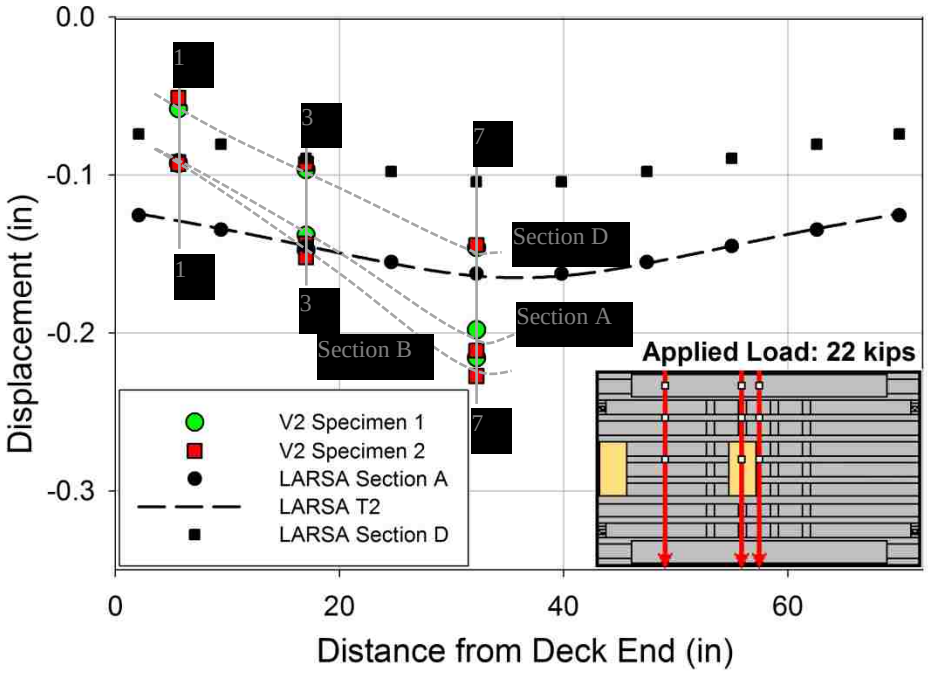

Figure 41. Displacement along transverse sections A, B and D

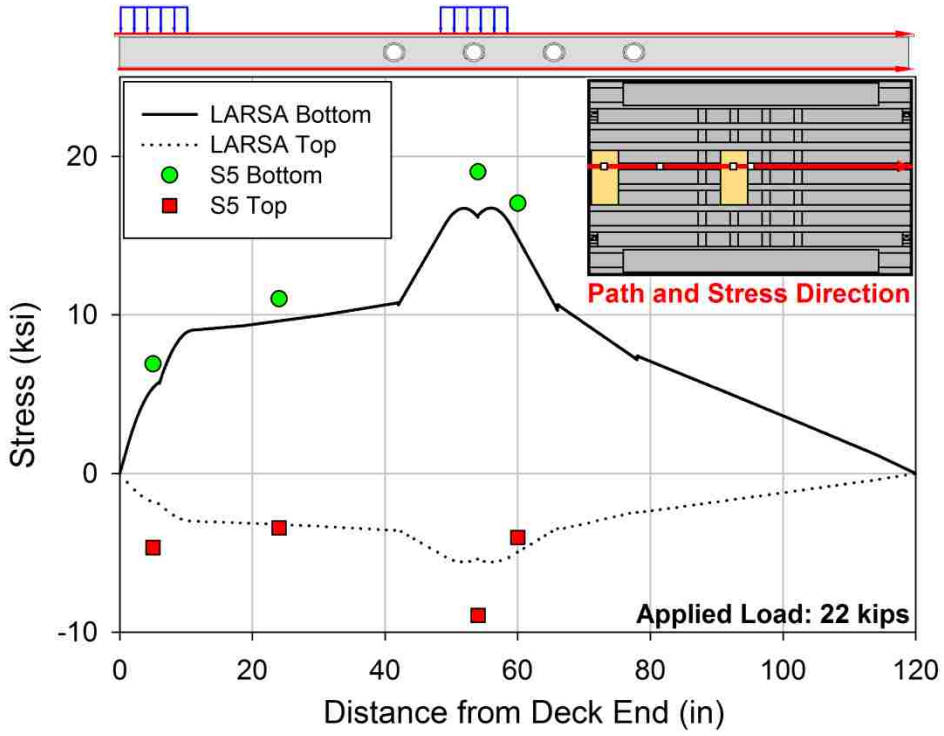

Figure 42. Specimen #1, longitudinal stress along S5

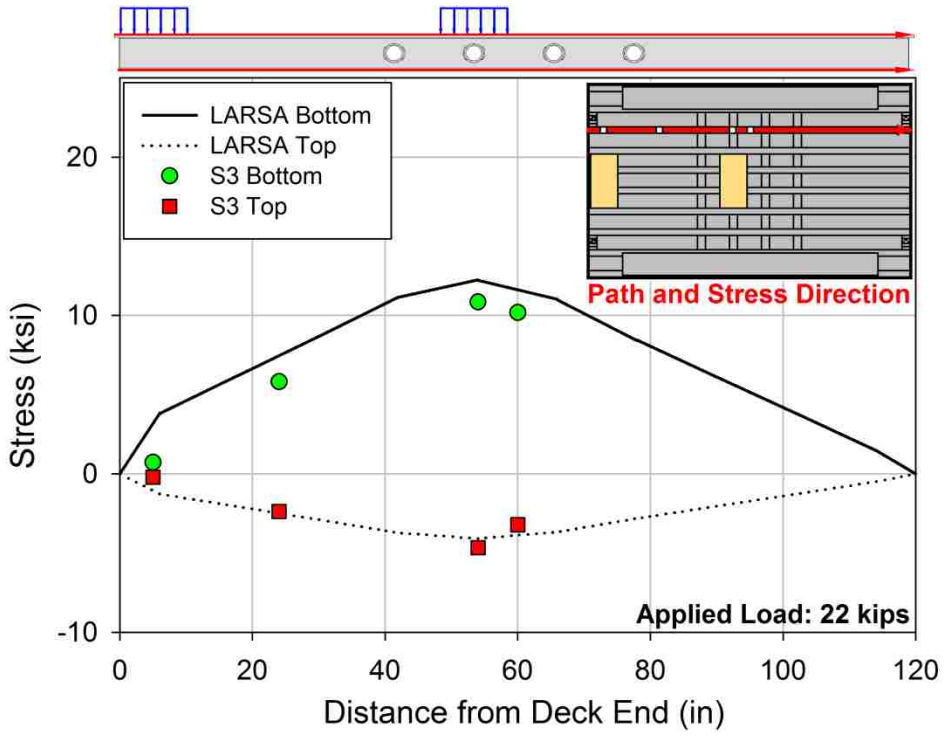

Figure 43. Specimen #1, longitudinal stress along S3

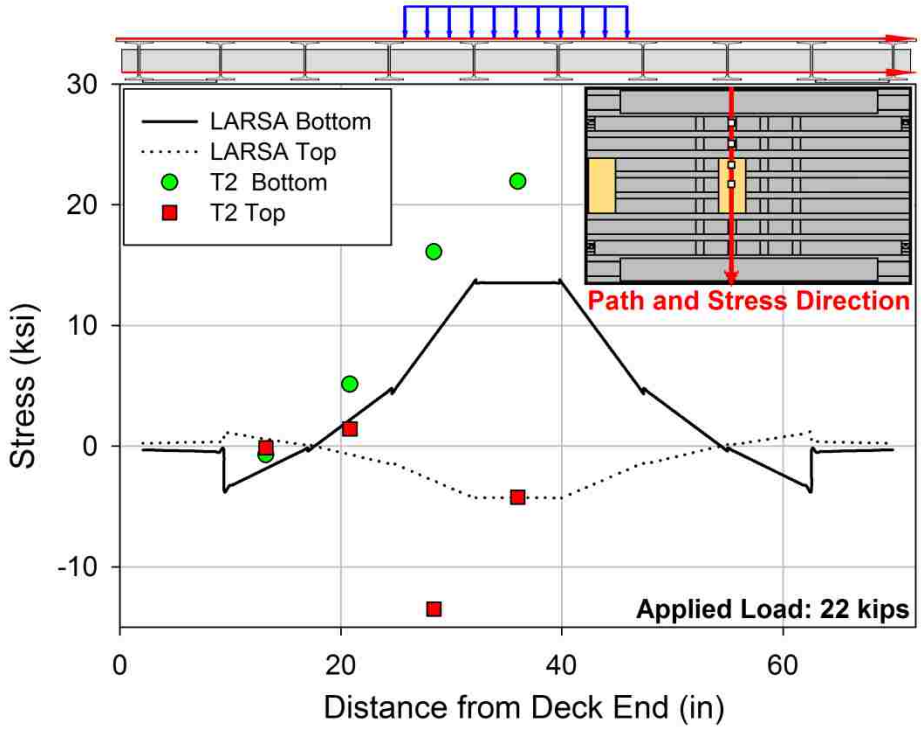

Figure 44. Specimen #1, transverse stress along T2

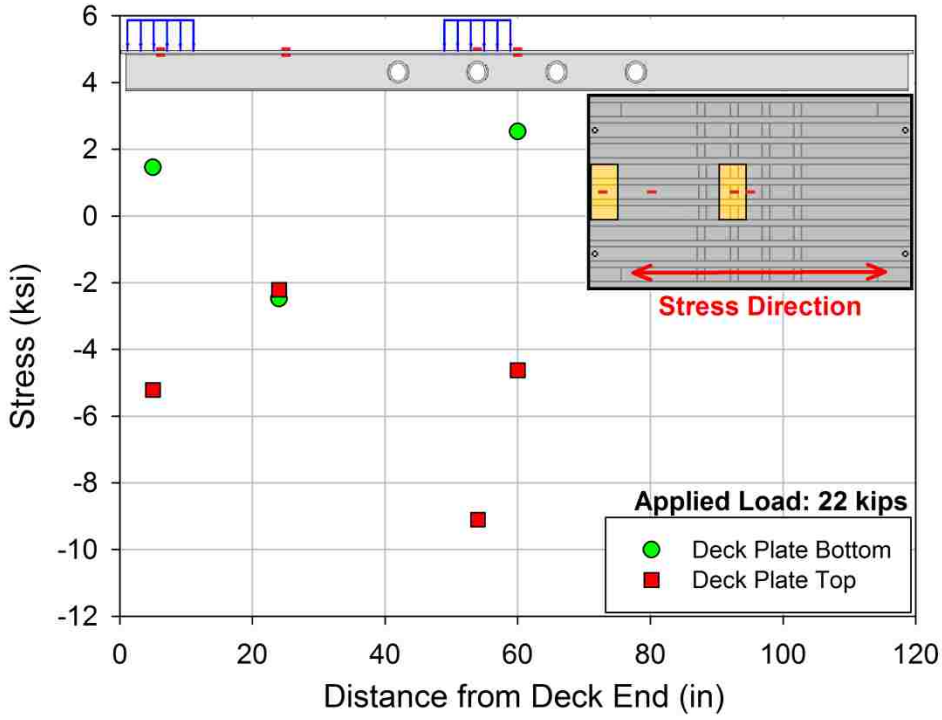

Figure 45. Specimen #1, longitudinal stress on top and bottom of deck plate between S5 and S6

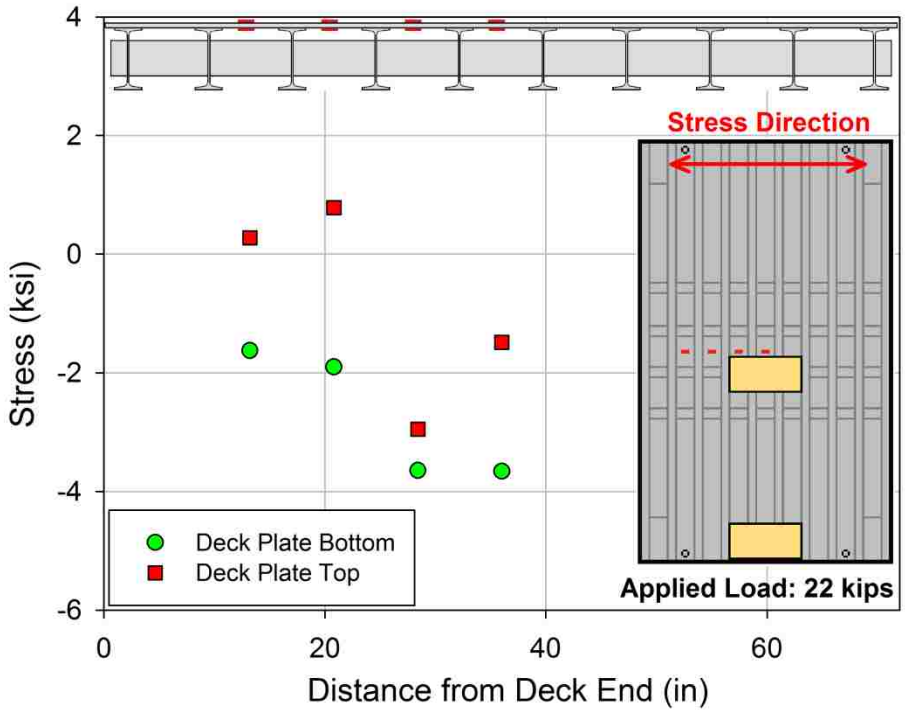

Figure 46. Specimen #1, transverse stress on top and bottom of deck plate, along deck centerline

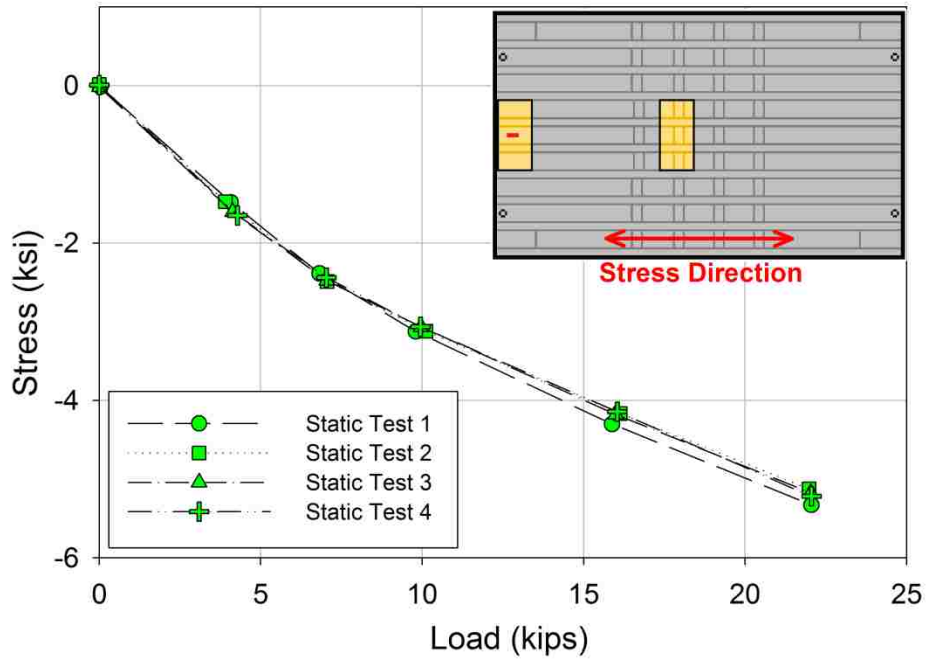

Figure 47. Specimen #1, measurements at strain gauge TDP_L5

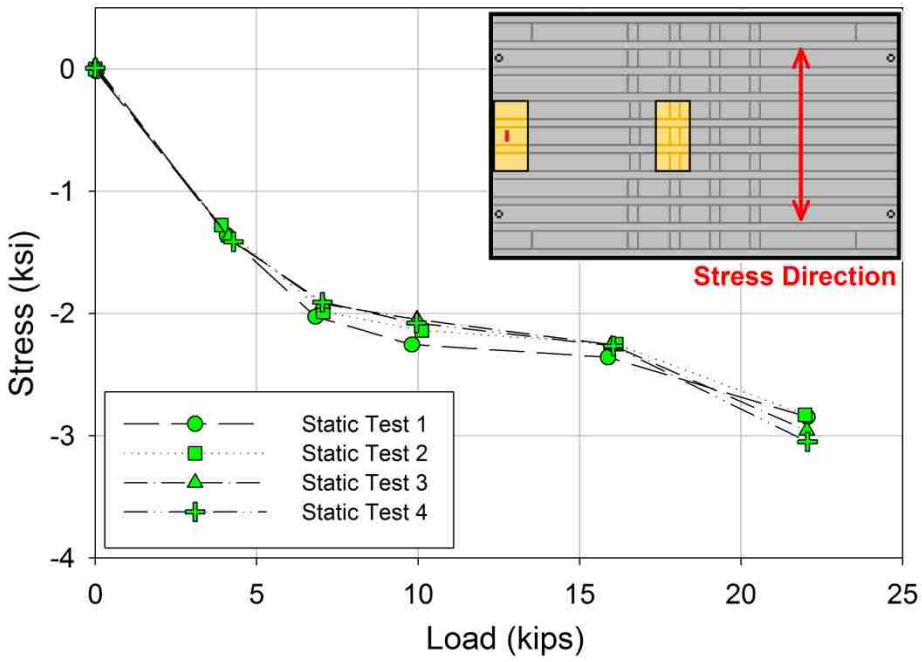

Figure 48. Specimen #1, measurements at strain gauge TDP_T5

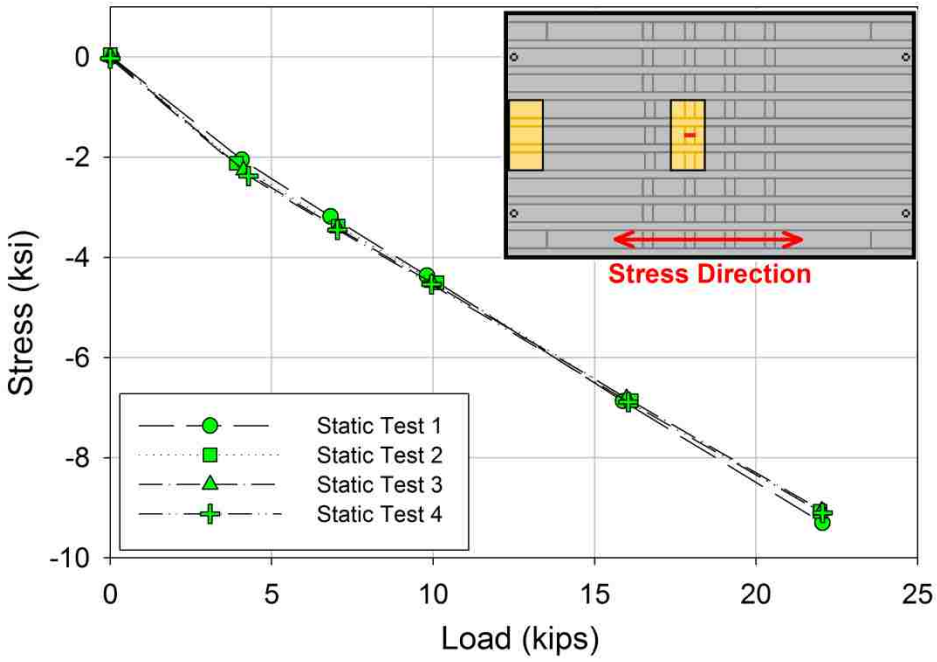

Figure 49. Specimen #1, measurements at strain gauge TDP_L9

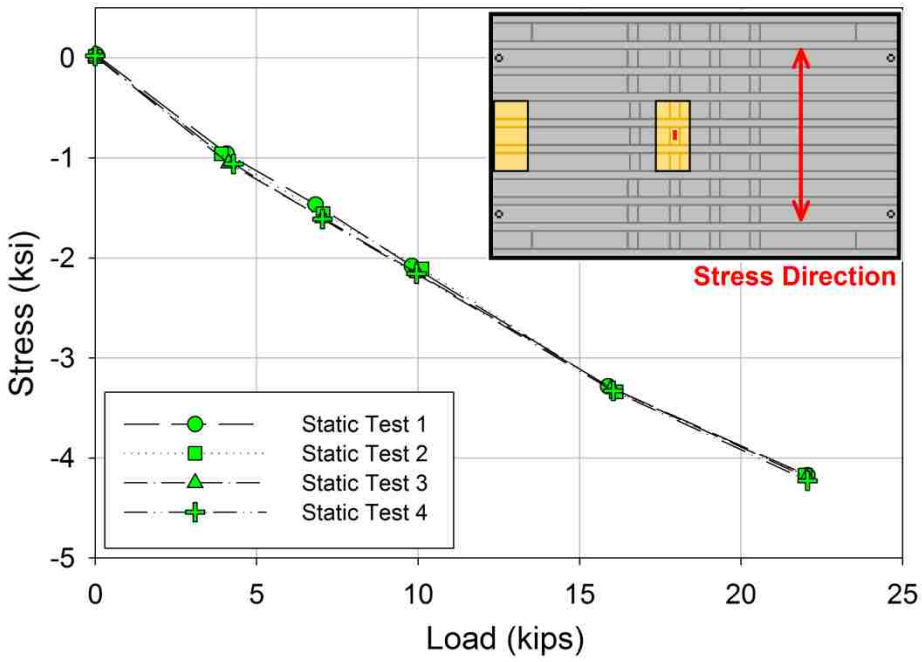

Figure 50. Specimen #1, measurements at strain gauge TDP_T9

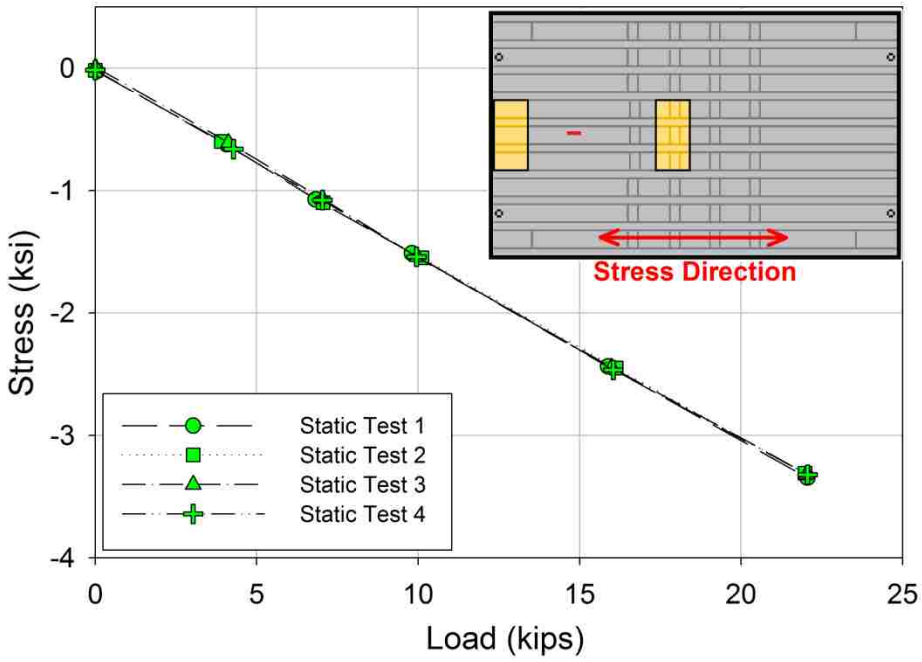

Figure 51. Specimen #1, measurements at strain gauge TDP_5

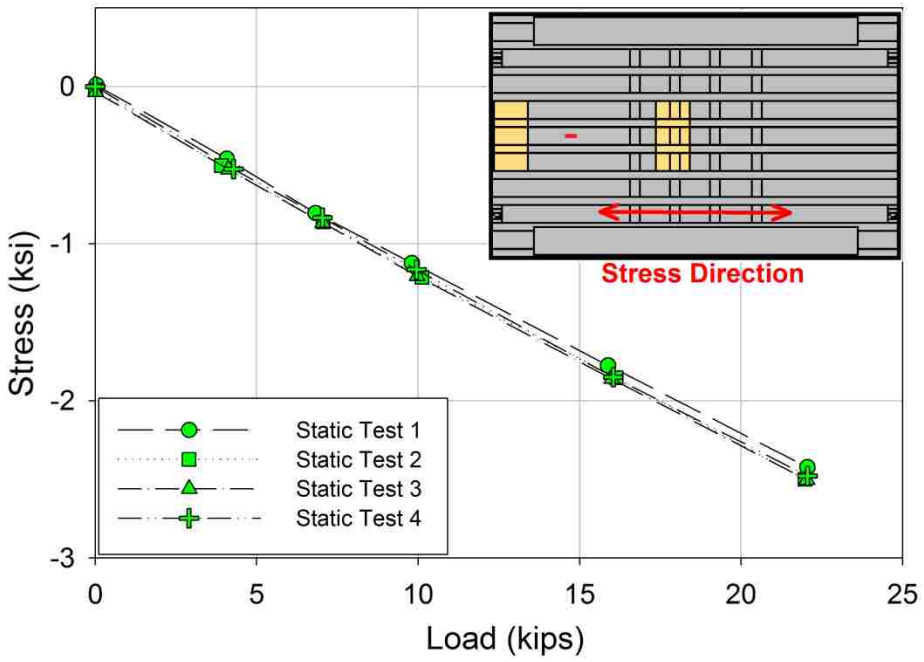

Figure 52. Specimen #1, measurements at strain gauge BDP_4

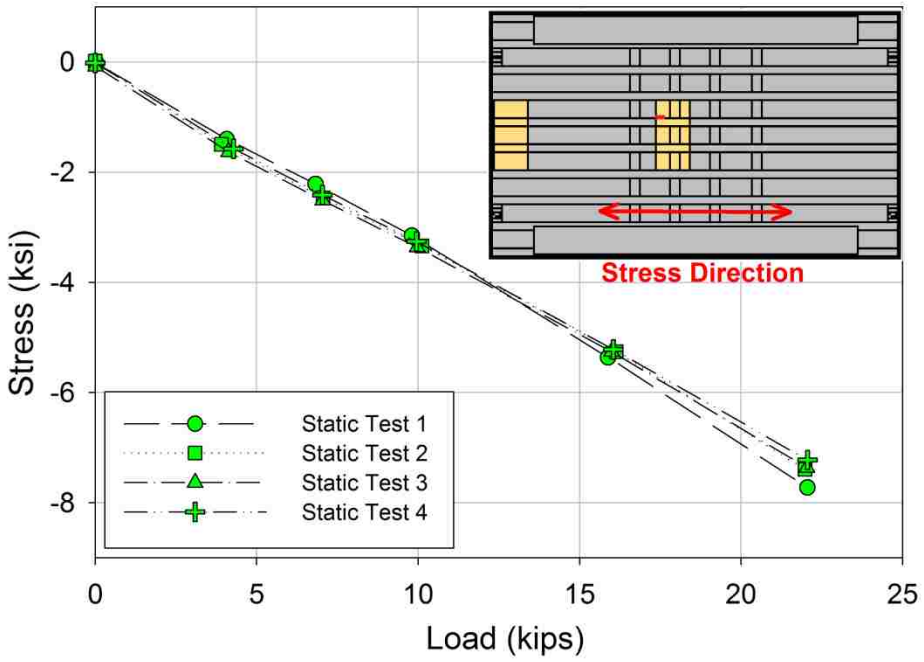

Figure 53. Specimen #1, measurements at strain gauge S5_DW2

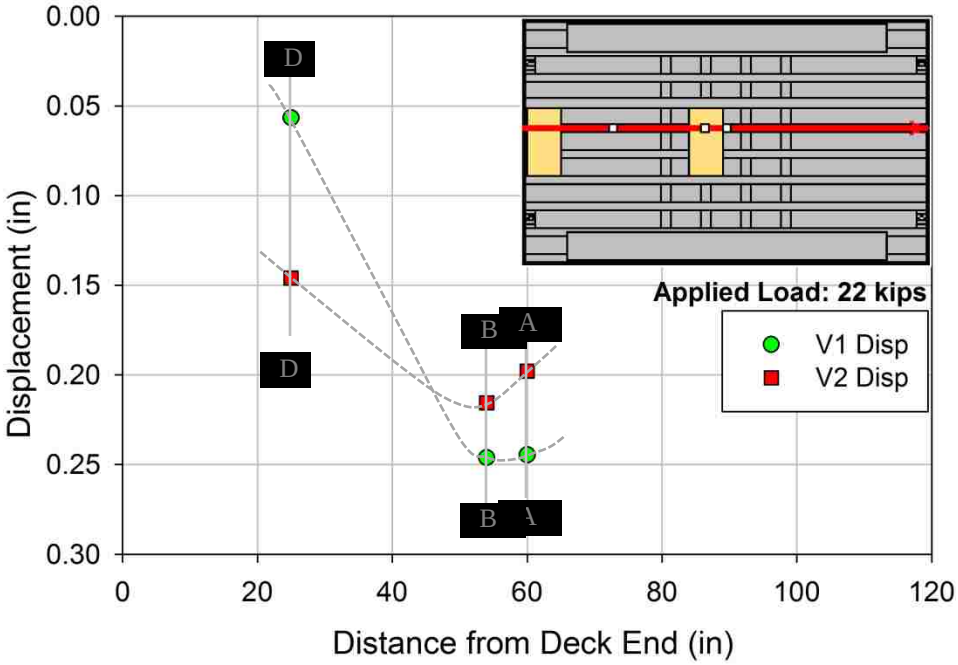

Figure 54. V1 versus V2 deck displacement along stringer S5

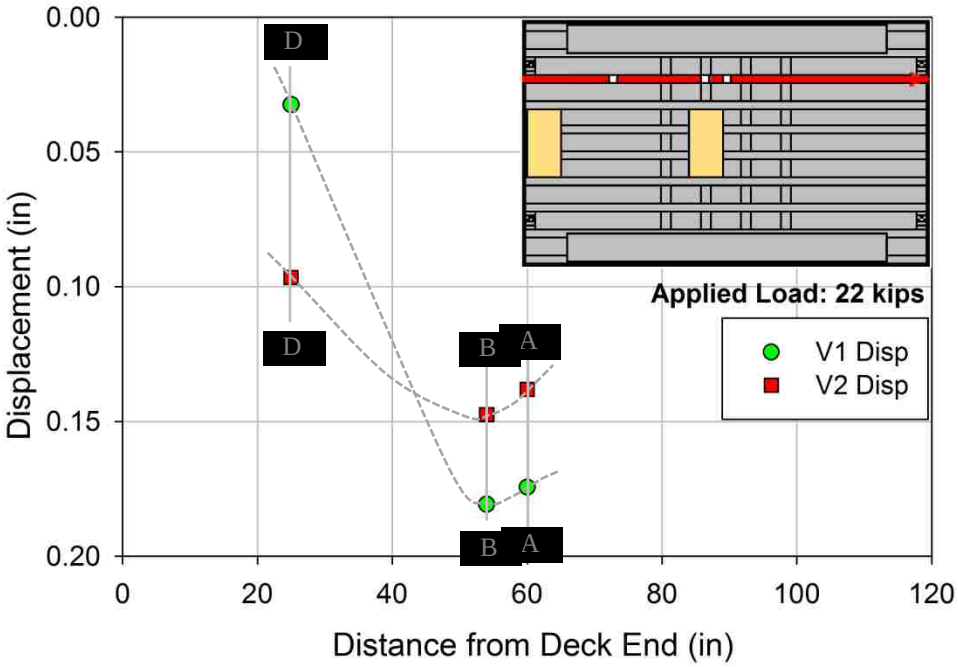

Figure 55. V1 versus V2 deck displacement along stringer S3

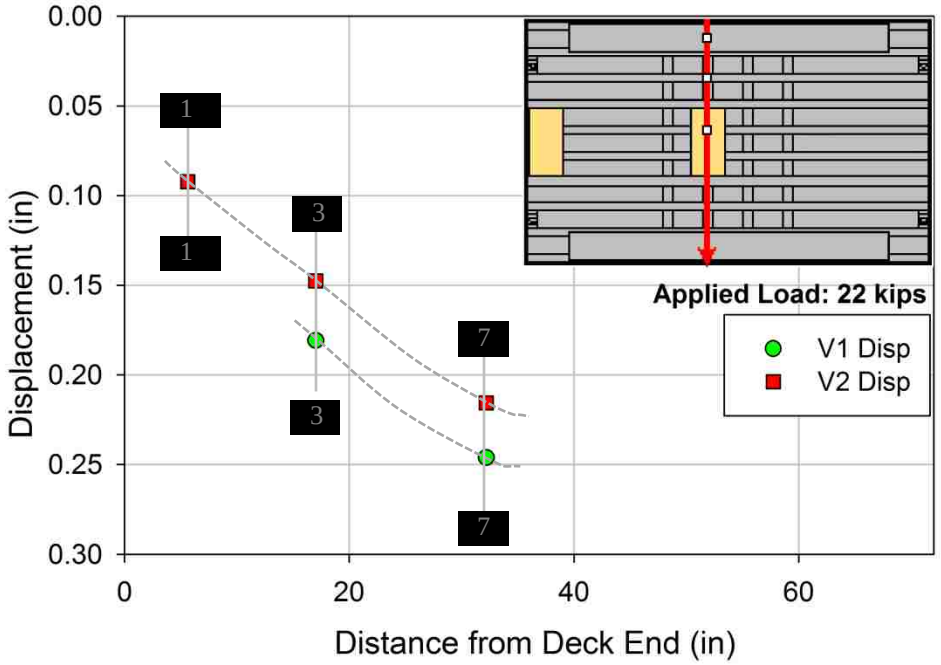

Figure 56. V1 versus V2 deck displacement along tube T2

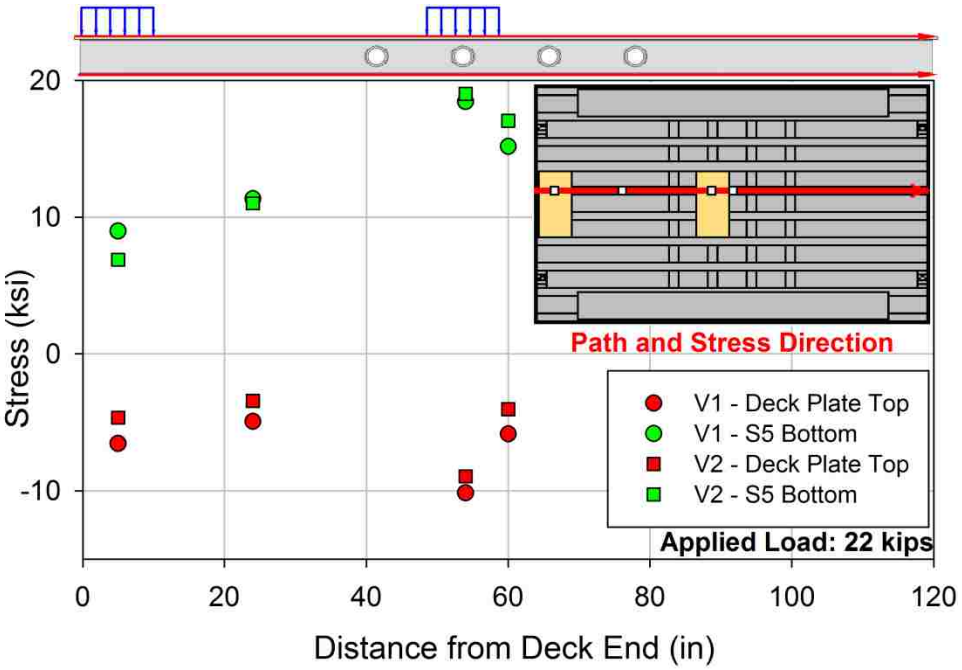

Figure 57. V1 versus V2 deck longitudinal stress along stringer S5

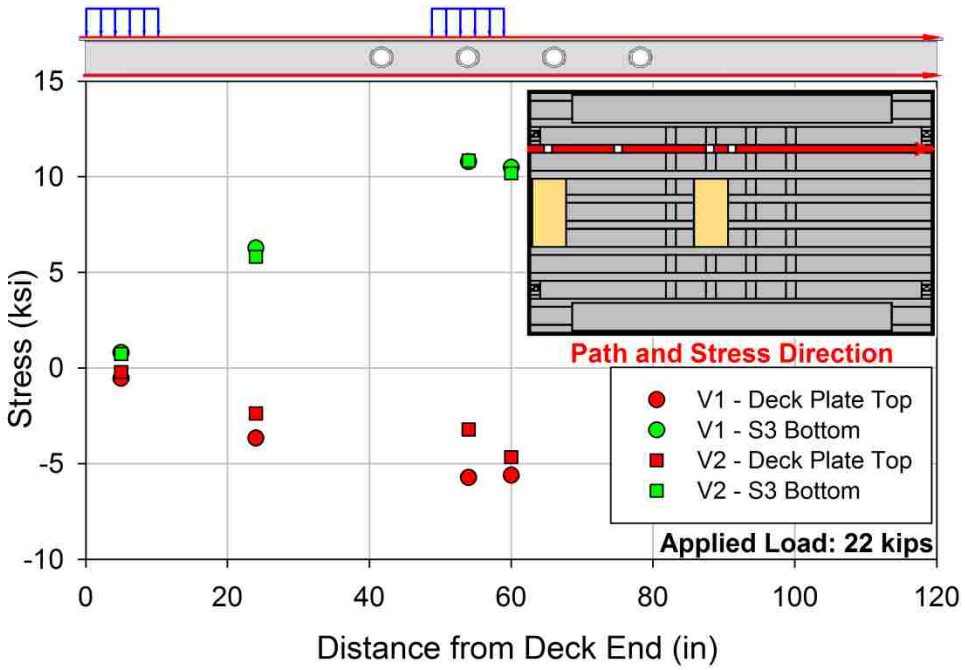

Figure 58. V1 versus V2 deck longitudinal stress along stringer S3

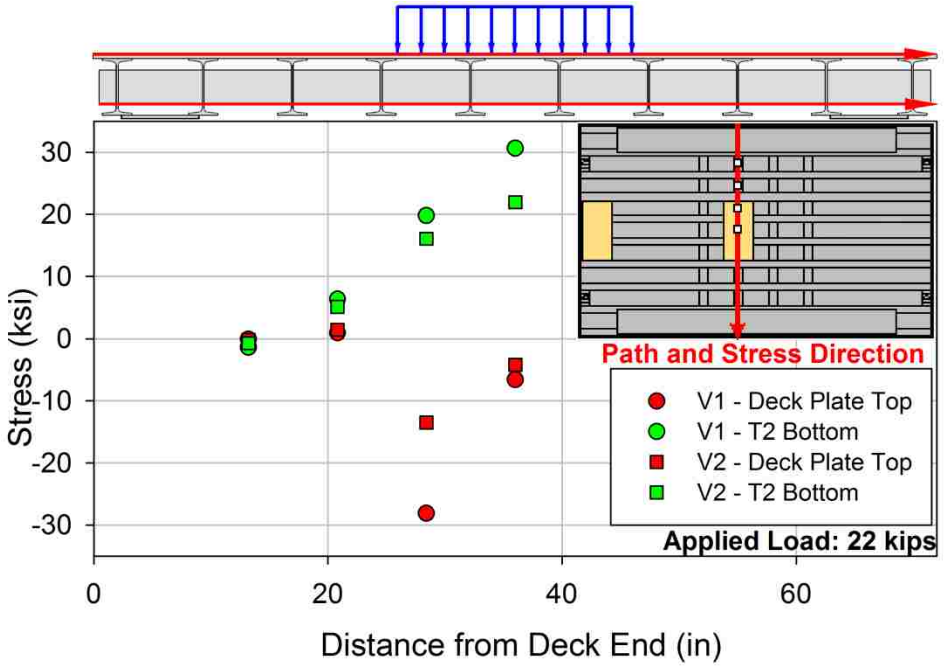

Figure 59. V1 versus V2 deck transverse stress along tube T2

Figure 60. Specimen #1, crack at the east weld of the S5-T2 intersection

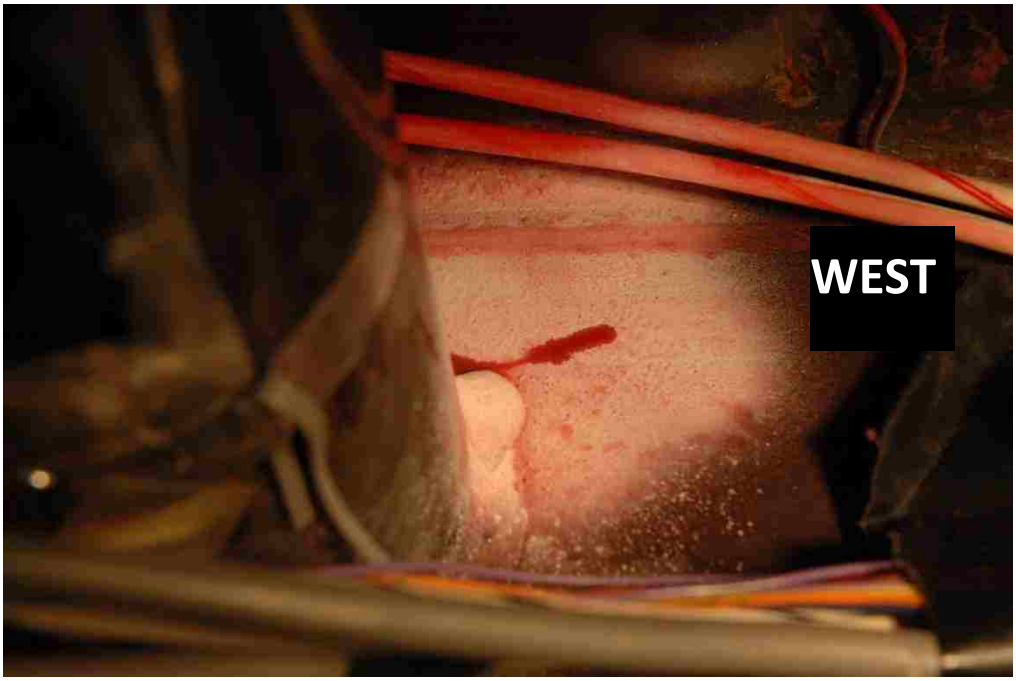

Figure 61. Specimen #1, crack at the west weld of the S5-T2 intersection

Figure 62. Specimen #1, cracks at S7-T3 intersection, shown with dye penetrant

Figure 63. Specimen #1, cracks at S9-T4 intersection, shown with dye penetrant

Figure 64. Specimen #1, cracks at S7-T1 intersection, shown with dye penetrant

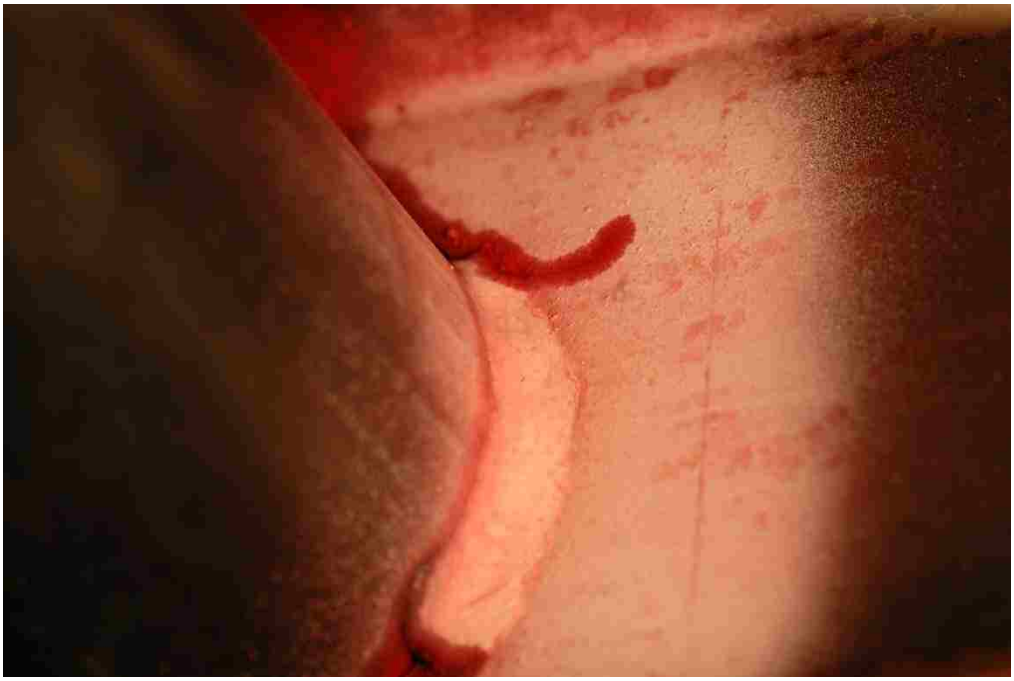

Figure 65. Specimen #2, crack at west weld of the S9-T1 intersection

Figure 66. Specimen #2, crack at east weld of the S9-T1 intersection

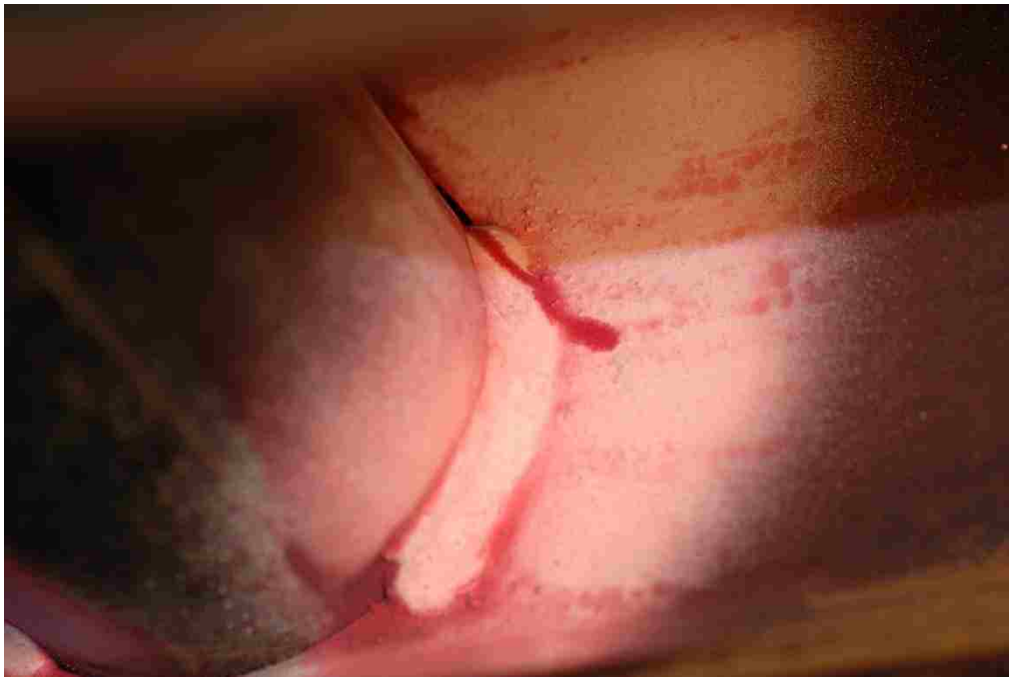

Figure 67. Specimen #2, crack at west weld of the S7-T1 intersection

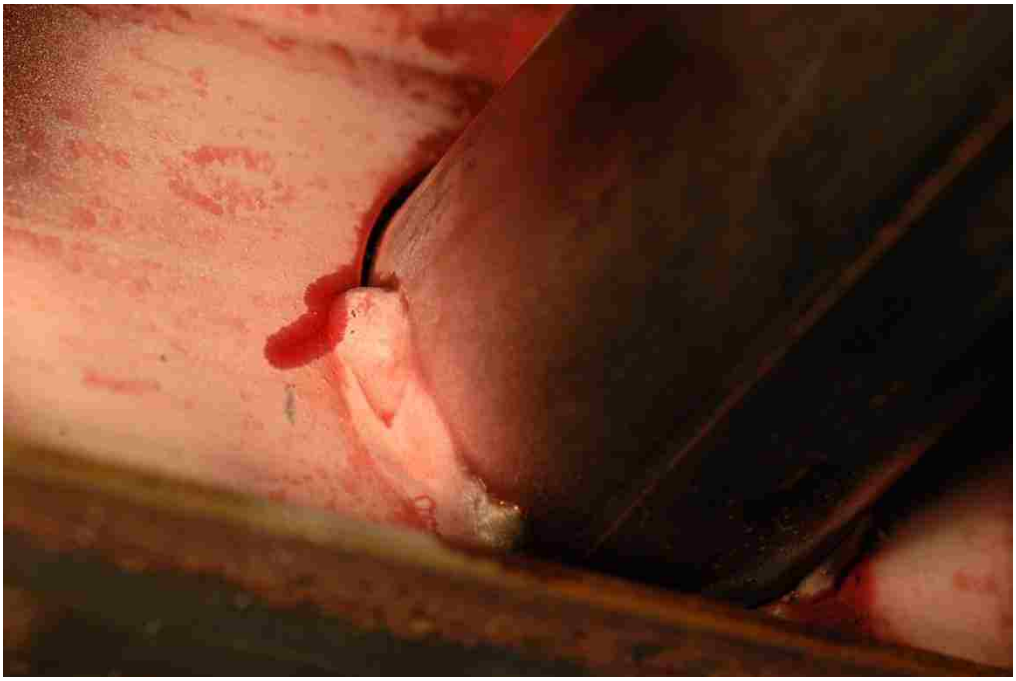

Figure 68. Specimen #2, crack at east weld of the S8-T1 intersection

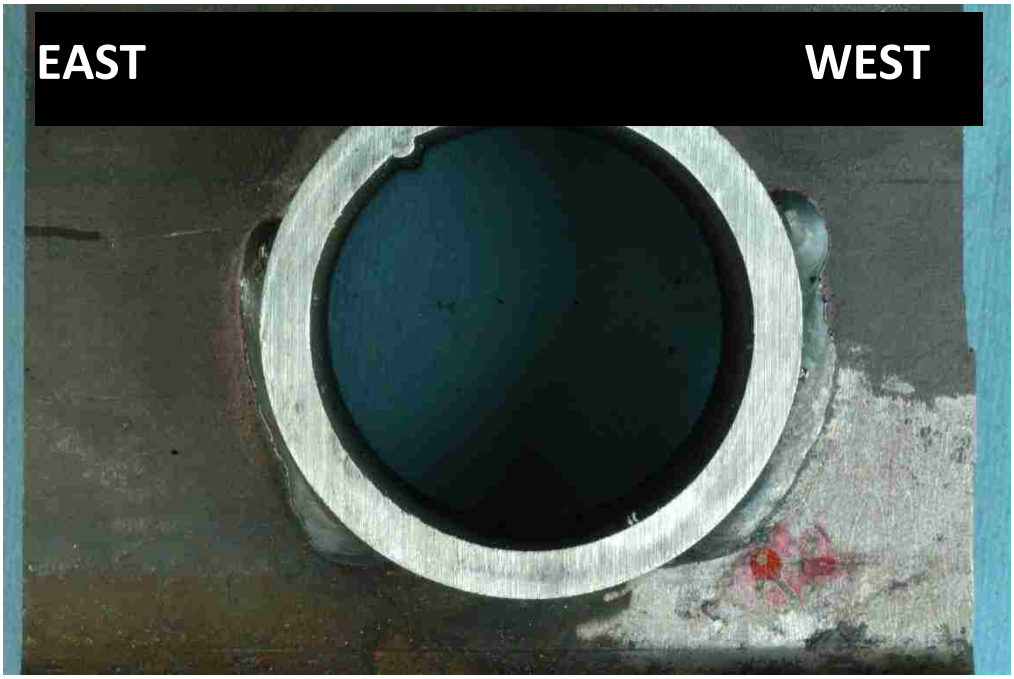

Figure 69. S5-T2 connection cut out, north face

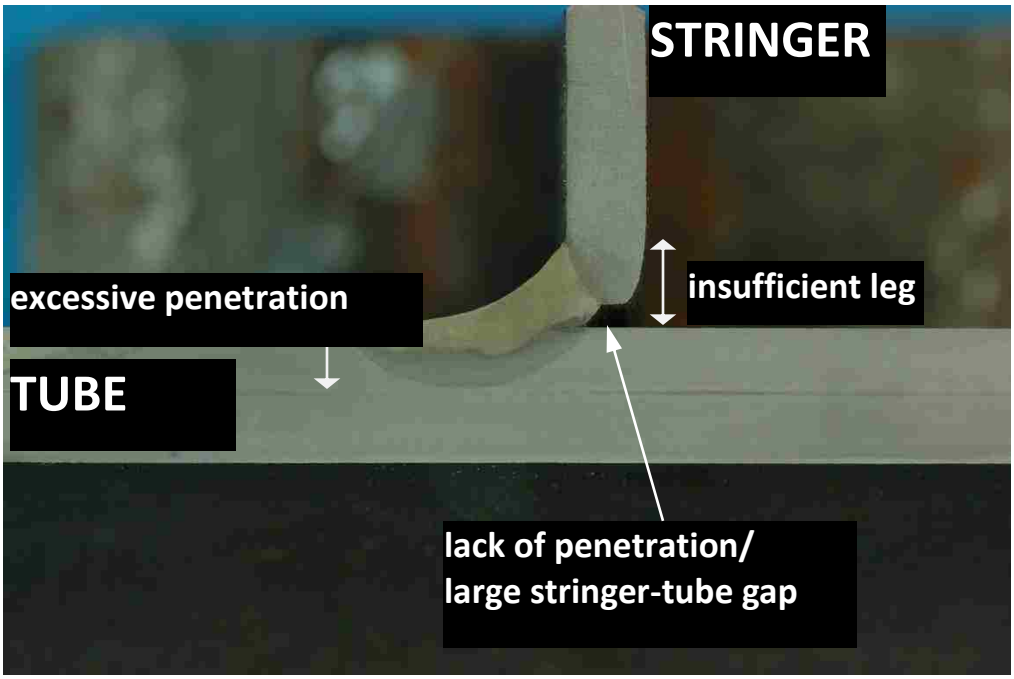

Figure 70. Profile of S5-T2 east weld

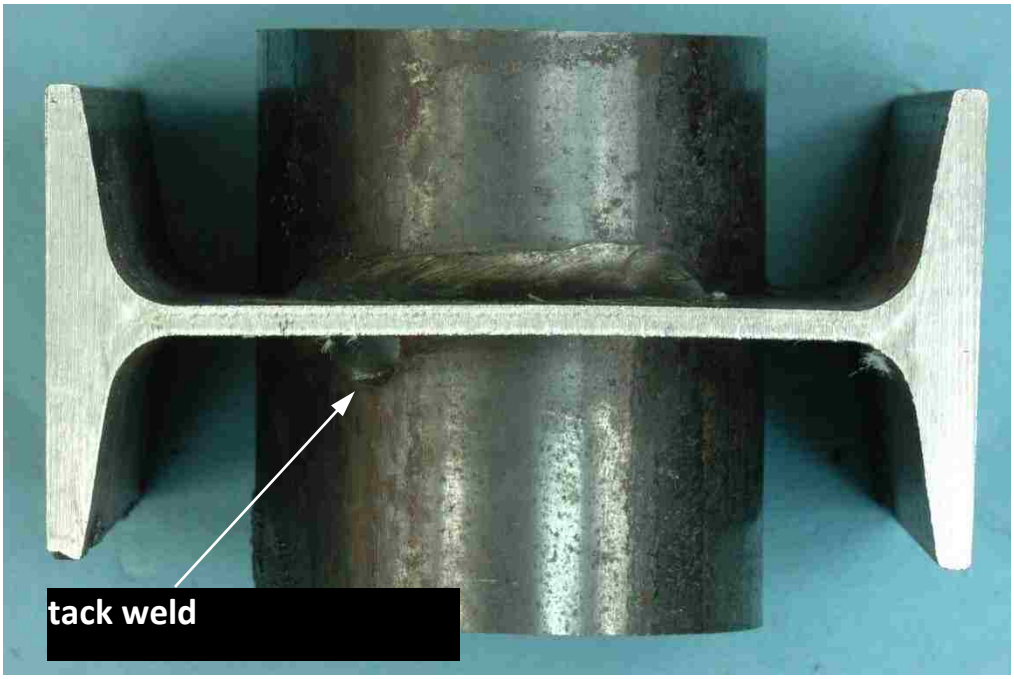

Figure 71. S9-T2 connection cutout, west face

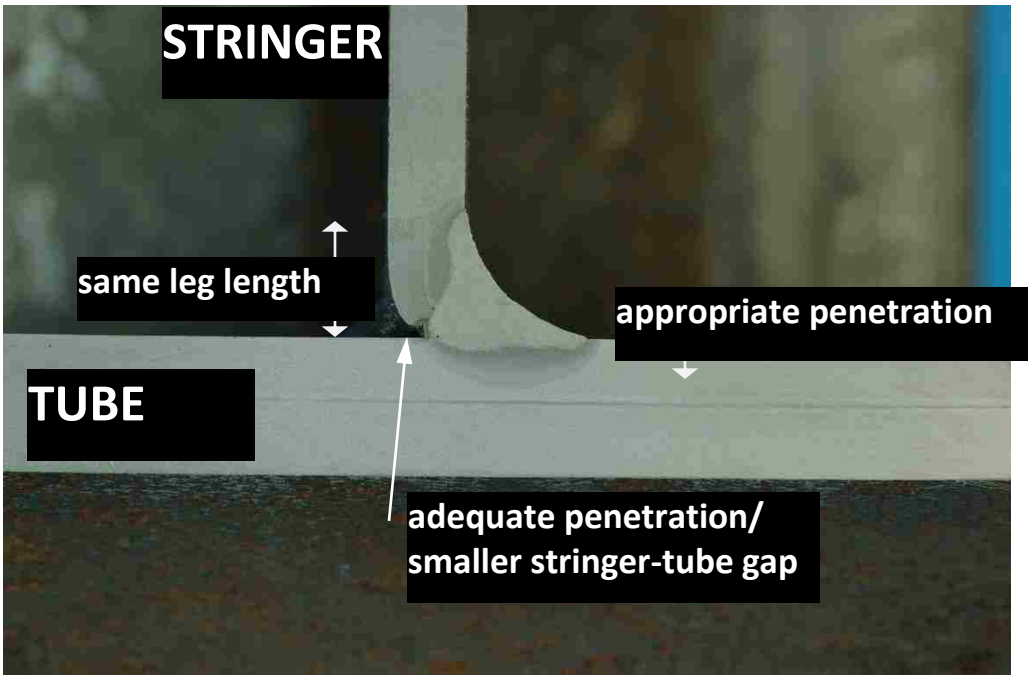

Figure 72. Profile of S9-T2 west weld

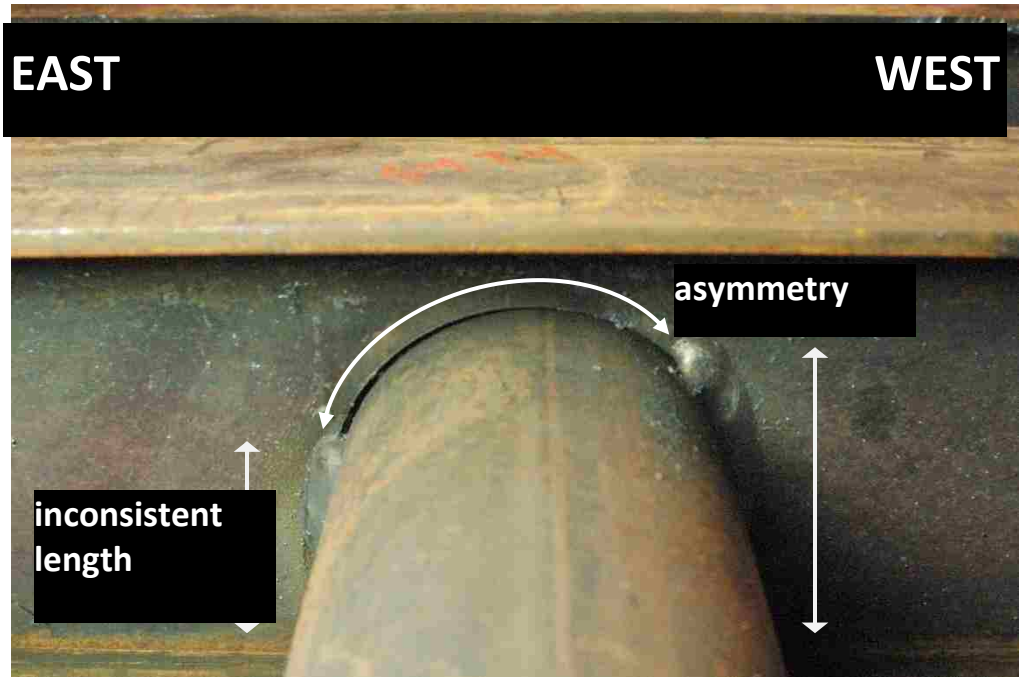

Figure 73. Welds at intersection of S4-T4 in specimen #1

Figure 74. West weld at intersection of S8-T2 in specimen #1

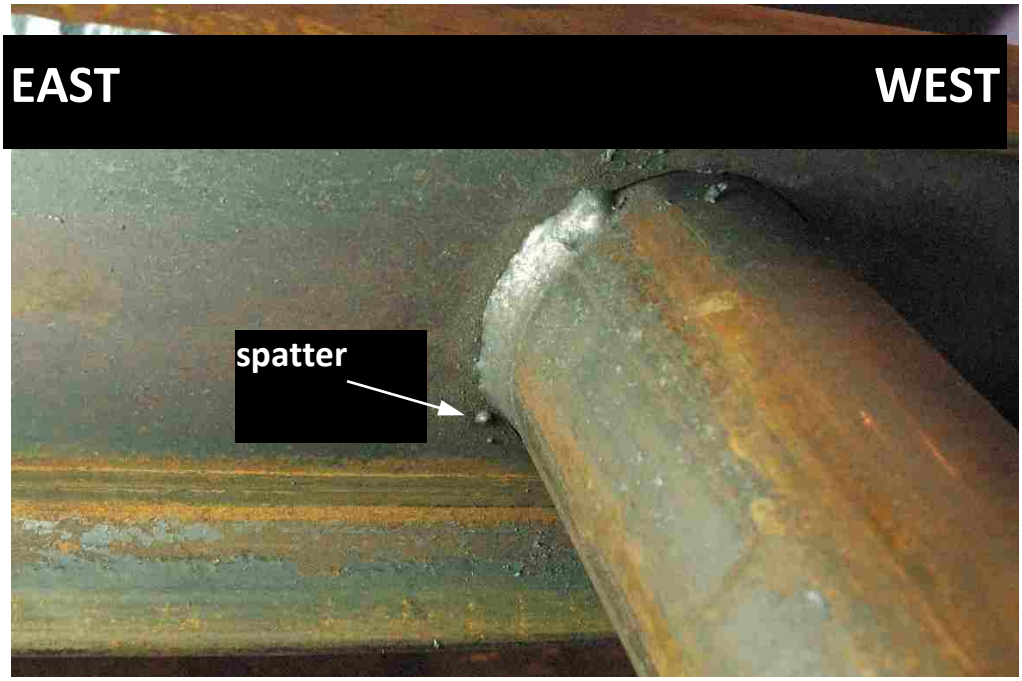

Figure 75. East weld at intersection of S8-T3 in specimen #1

Figure 76. S5-T2 east crack plane, bottom half

Figure 77. S5-T2 west crack plane, bottom half

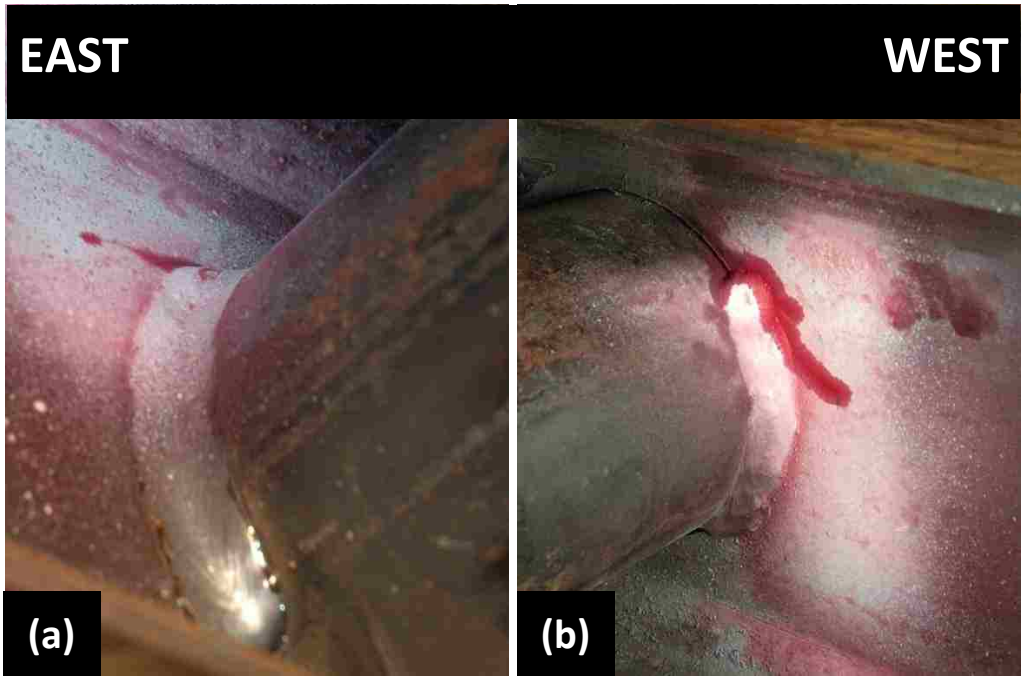

Figure 78. Specimen #1, cracks at S9-T2 connection (a) east weld crack, (b) west weld crack

Figure 79. S9-T2 west crack plane, bottom half

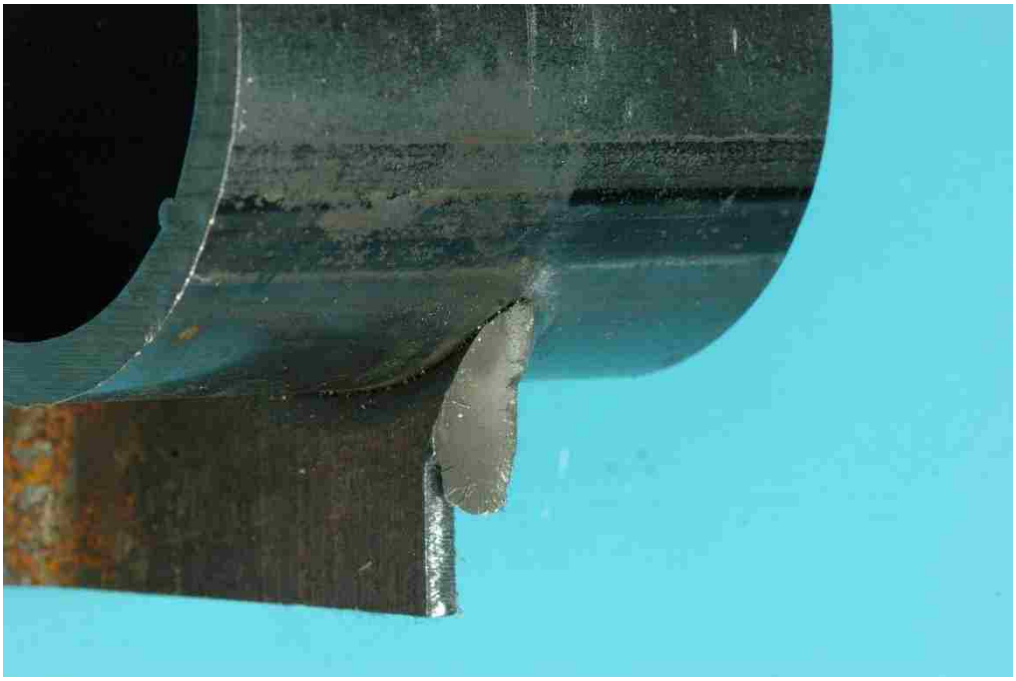

Figure 80. S9-T2 east crack plane, bottom half

Figure 81. SEM image of S5-T2 east weld fracture surface

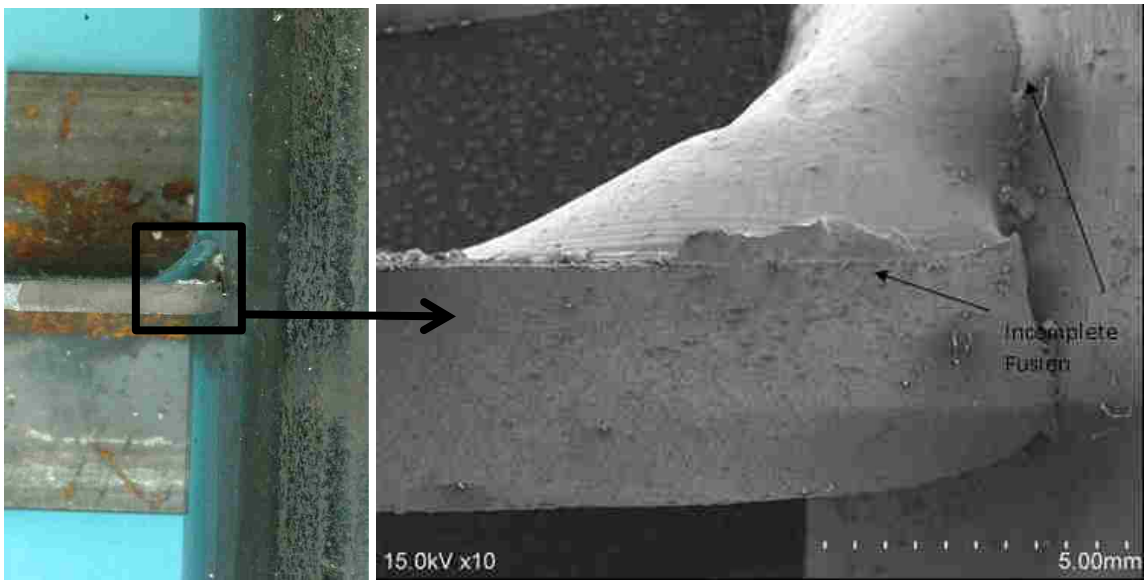

Figure 82. SEM image of S5-T2 west weld fracture surface

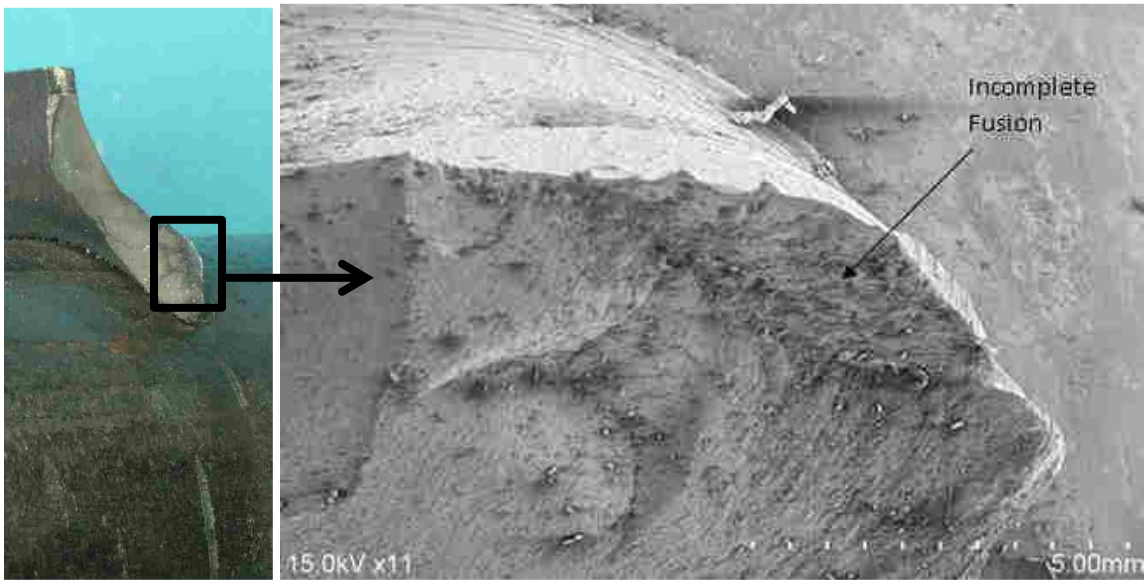

Figure 83. SEM image of S9-T2 west weld fracture surface

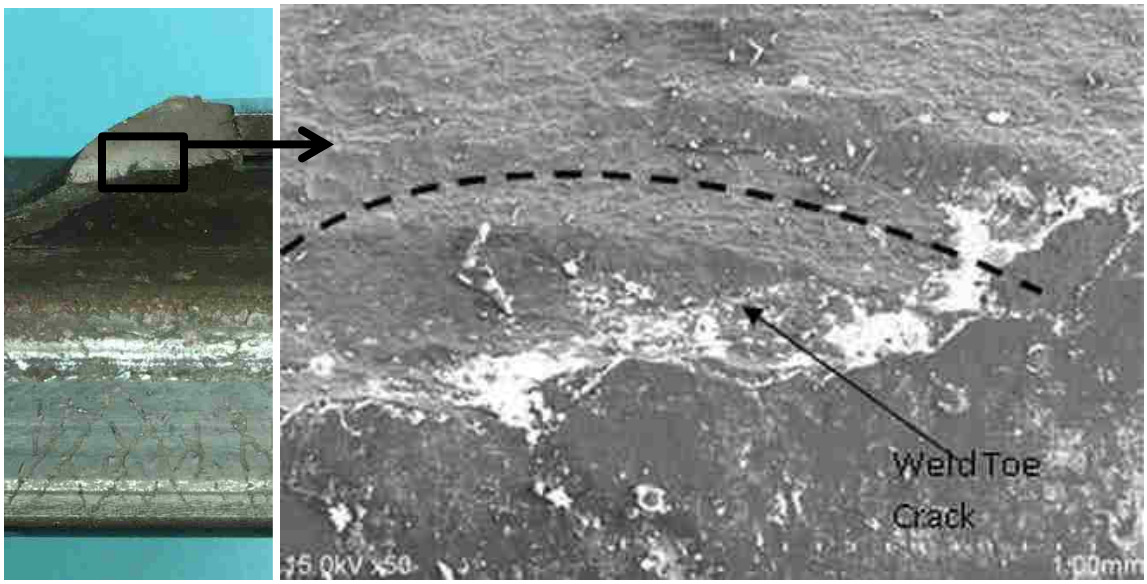

Figure 84. SEM image of S9-T2 east weld fracture surface

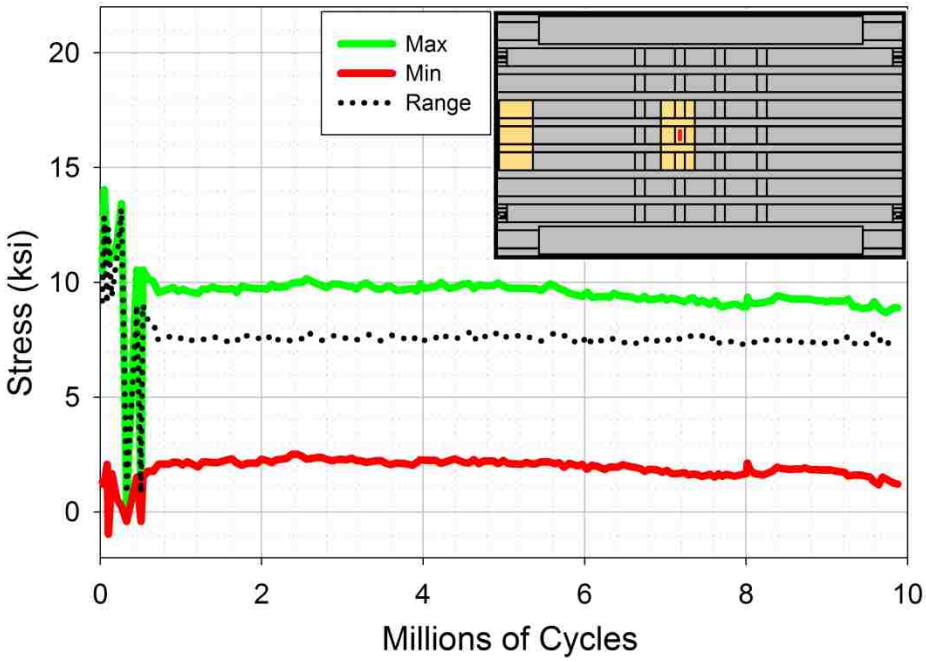

Figure 85. Specimen #1, measurements at strain gauge T2_4 during fatigue test

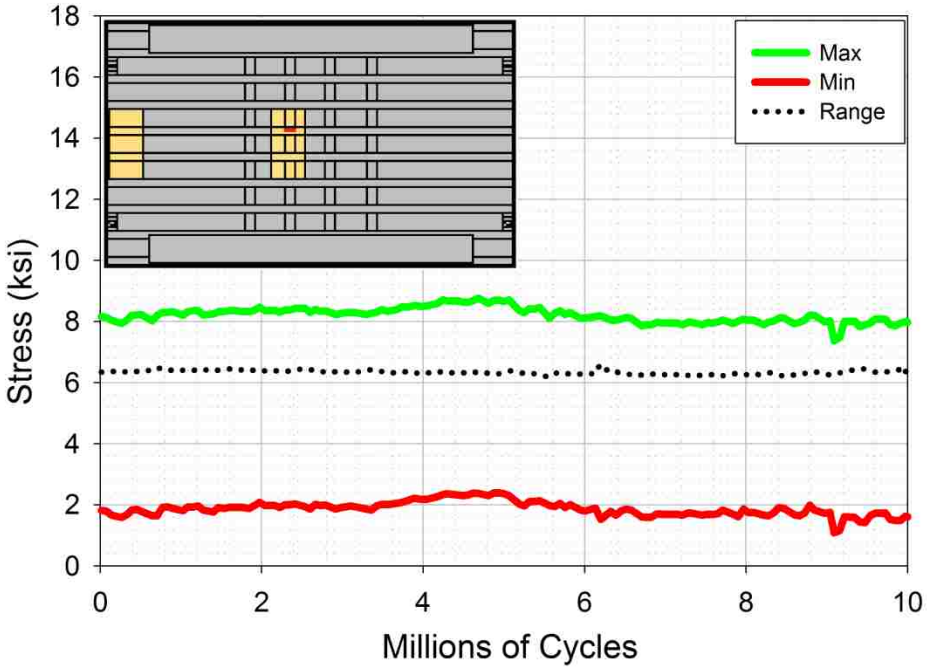

Figure 86. Specimen #2, measurements at strain gauge S5_B3 during fatigue test

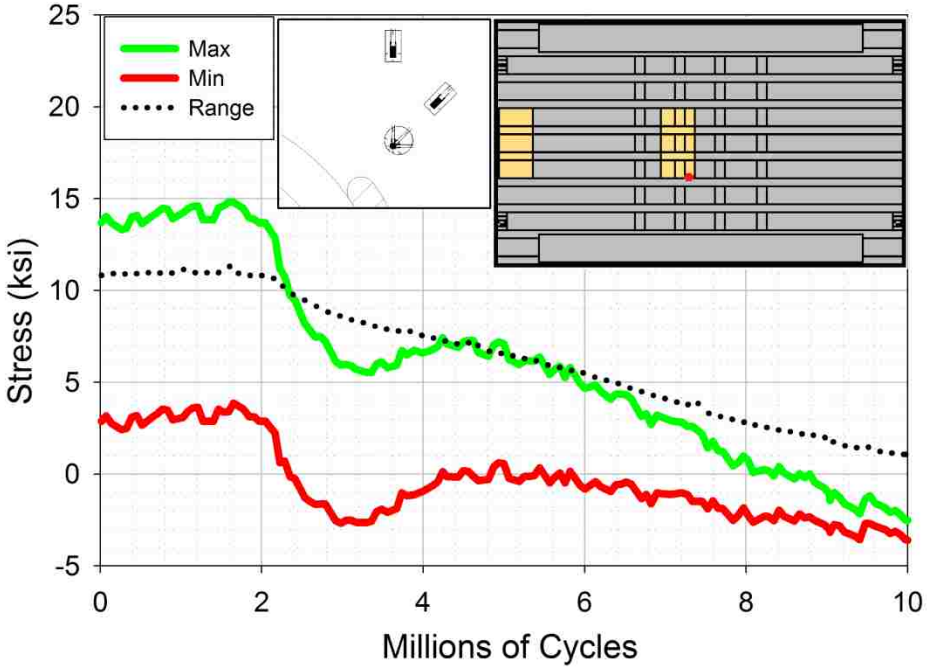

Figure 87. Specimen #2, principal stress "P" at S7_T2_N rosette during fatigue test

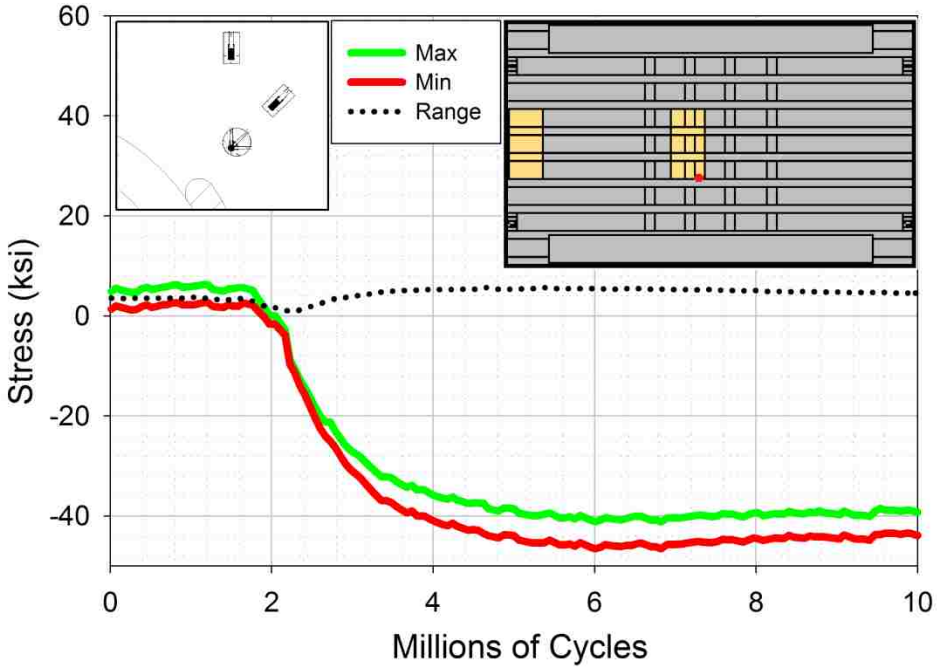

Figure 88. Specimen #2, principal stress "Q" at S7_T2_N rosette during fatigue test

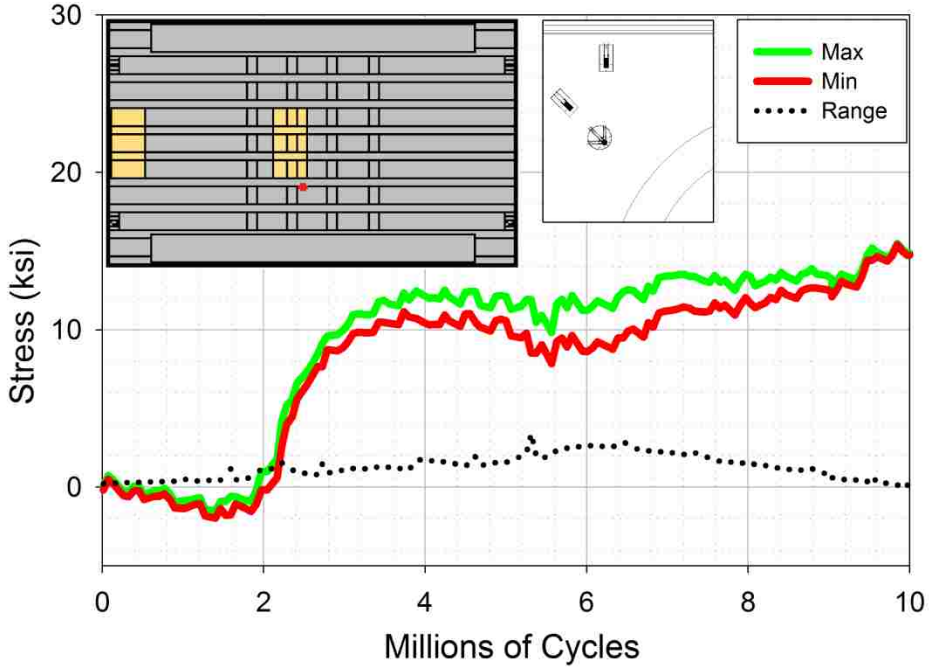

Figure 89. Specimen #2, principal stress "P" at S7_T2_S rosette during fatigue test

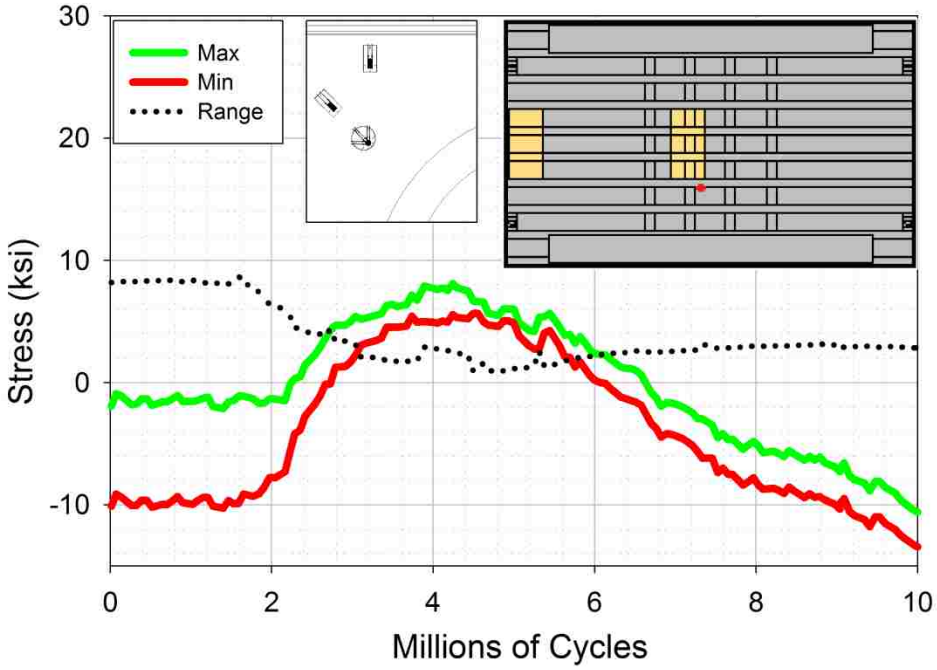

Figure 90. Specimen #2, principal stress "Q" at S7_T2_S rosette during fatigue test

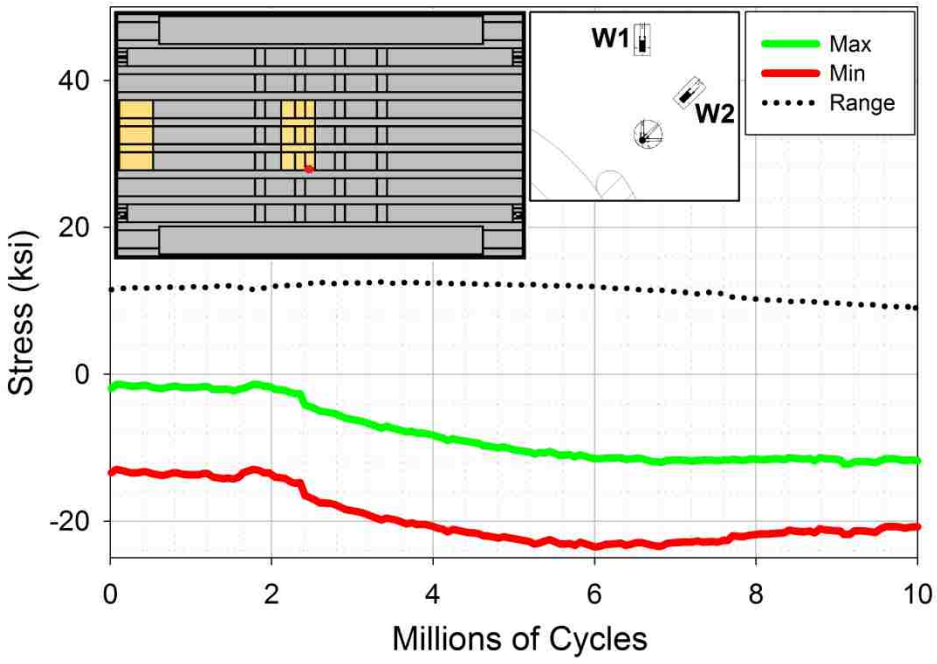

Figure 91. Specimen #2, measurements at strain gauge S7T2_W1 during fatigue test

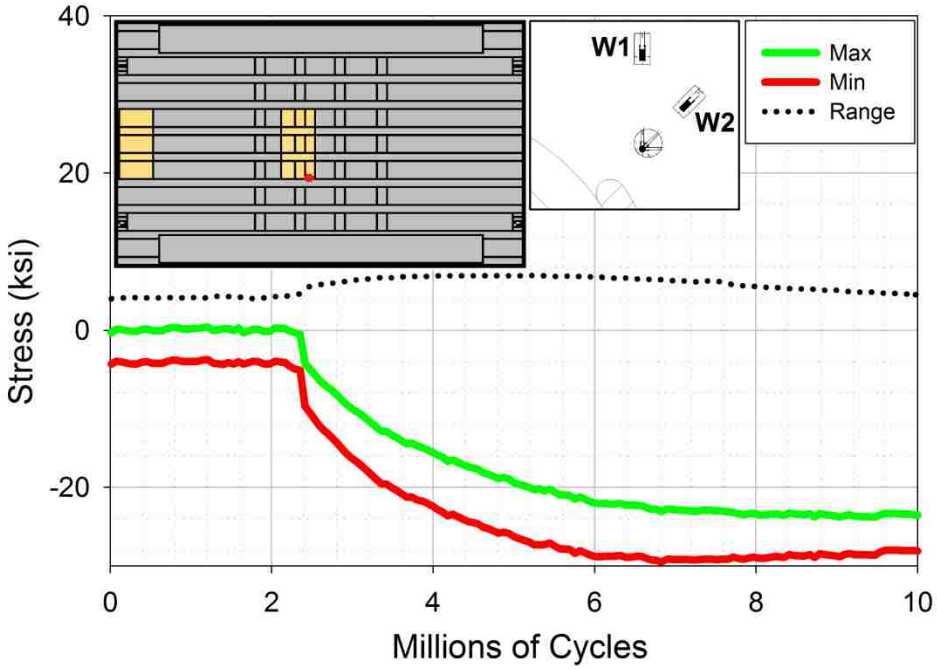

Figure 92. Specimen #2, measurements at strain gauge S7T2_W2 during fatigue test

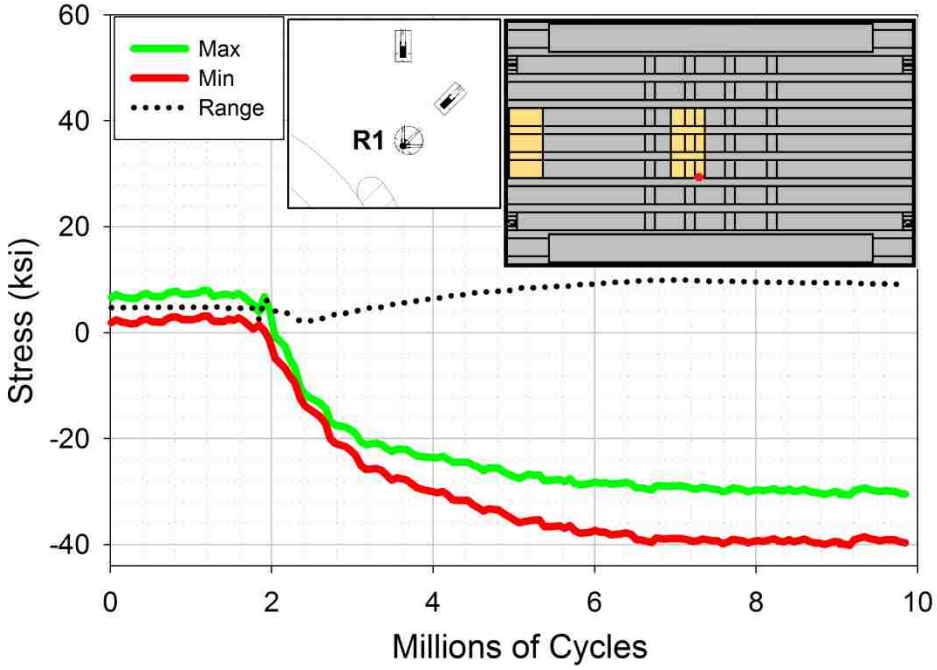

Figure 93. Specimen #2, measurements at strain gauge S7_T2R1 during fatigue test

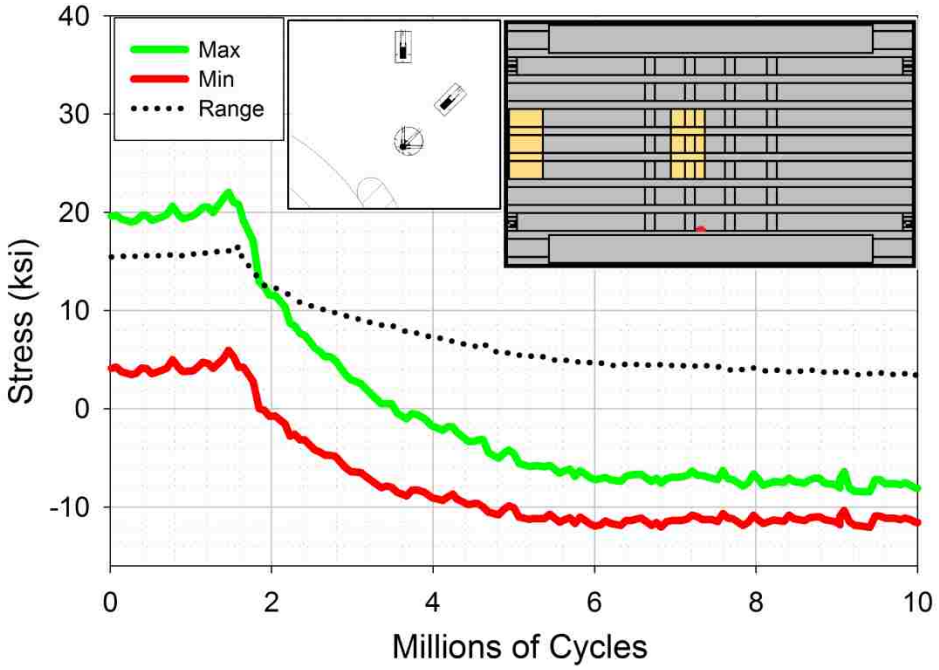

Figure 94. Specimen #2, principal stress "P" at S9_T2_N rosette during fatigue test

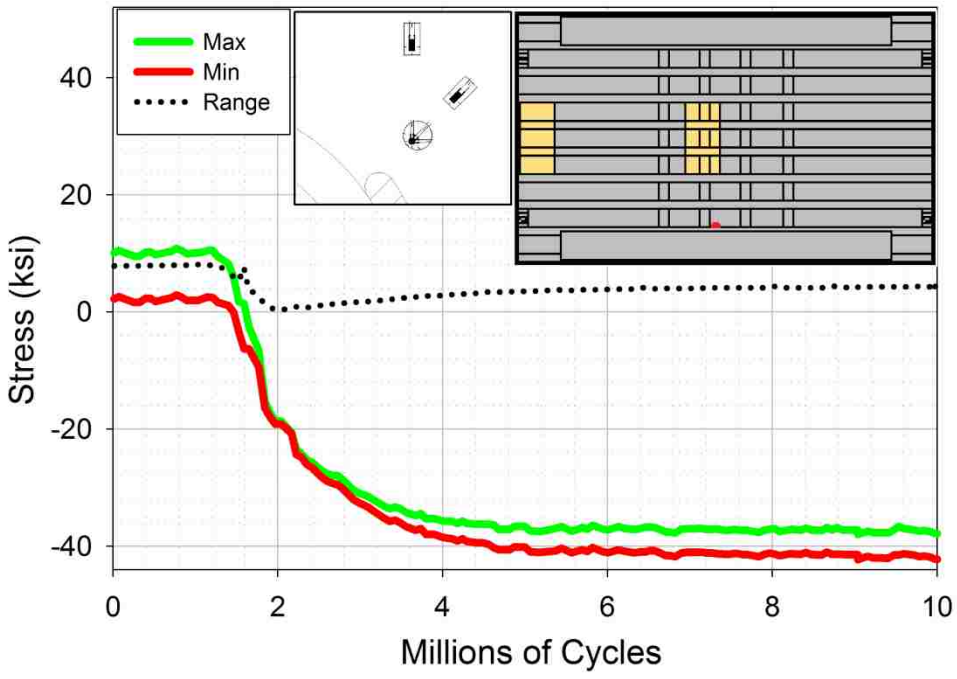

Figure 95. Specimen #2, principal stress "Q" at S9_T2_N rosette during fatigue test

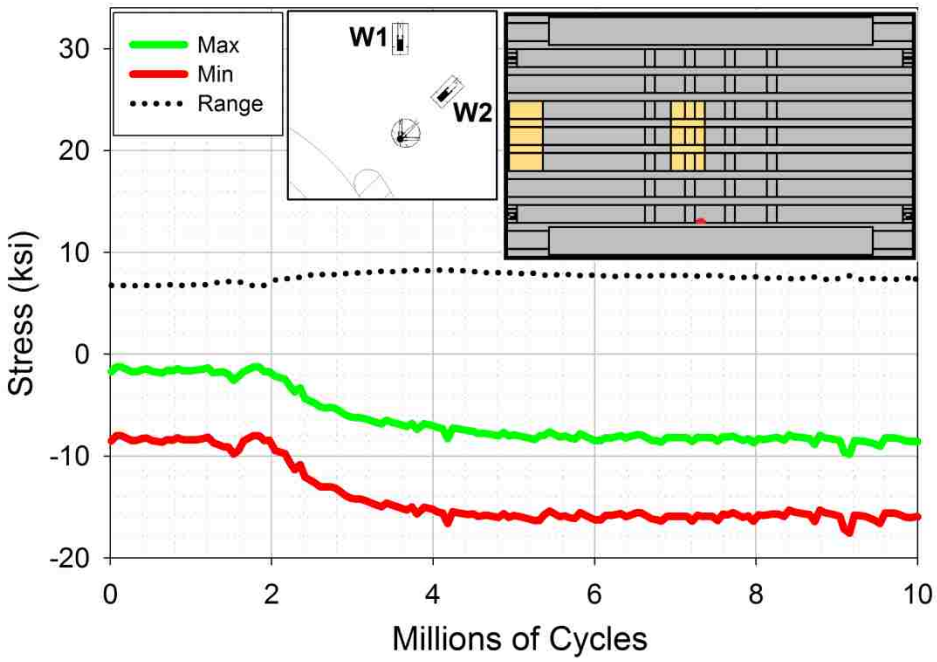

Figure 96. Specimen #2, measurements at strain gauge S9_T2W1 during fatigue test

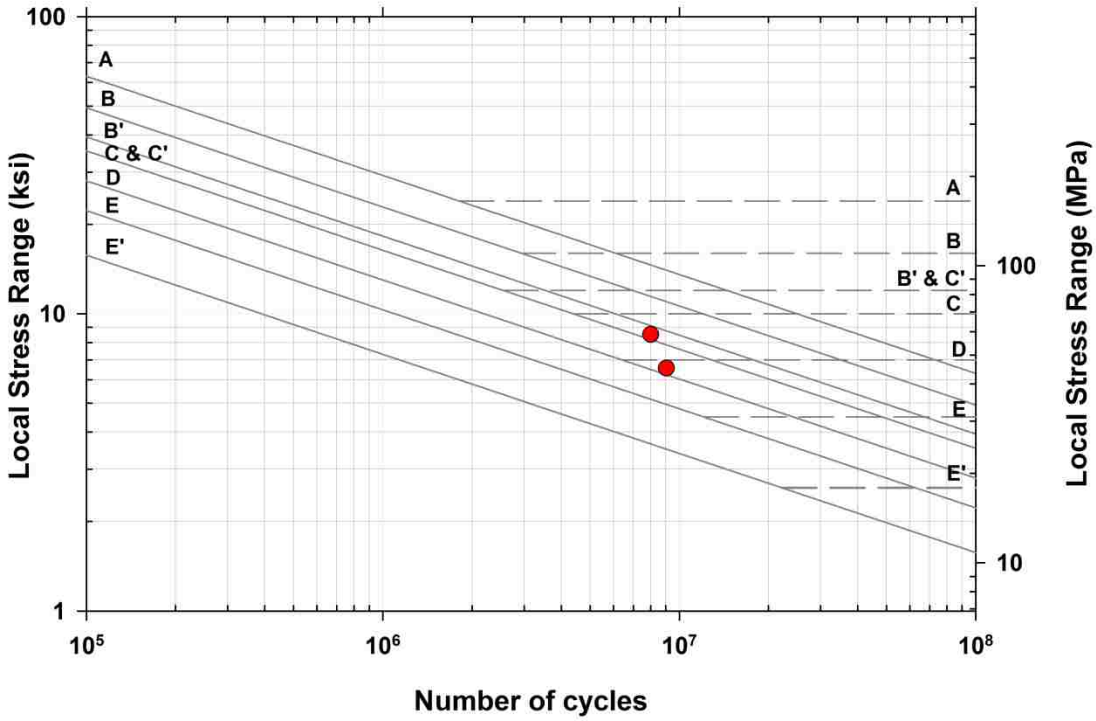

Figure 97. Fatigue test results plotted on the fatigue design curves of the AASHTO LRDF BDS

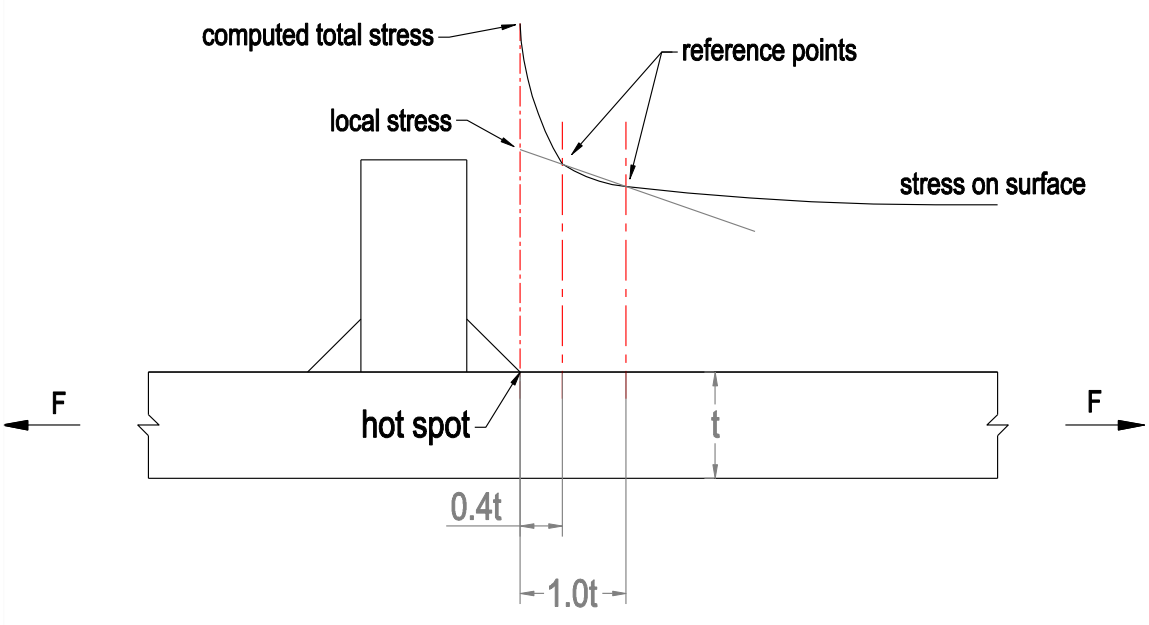

Figure 98. Extrapolation of hot spot stress from reference points

REFERENCES

AASHTO. (2012). *LRFD Bridge Design Specifications*. American Association of State Highway and Transportation Officials, Washington, DC.

Ahmed, M. Z. and Weisgerber, F. E. (1996). "Torsion Constant for Matrix Analysis of Structures Including Warping Effect." International Journal of Solids and Structures, Elsevier, 33 (3), 361-374.

ASM International. 2012. "Nondestructive Evaluation and Quality Control." In ASM Handbook. 9th ed. Vol. 17. Materials Park, Ohio: ASM International.

Dassault Systèmes Simulia Corp. (2012). ABAQUS/Standard Version 6.10, Dassault Systèmes, Inc. Providence, RI, http://simulia.com/

Galambos, Theodore V. 1978. "Elastic Behavior of Members." Chap. Chapter 2, In Structural Members and Frames, 22. St.Louis, MO.

LARSA. (2010). "LARSA 4D, the Complete Package for Bridge Design and Construction," http://www.larsa4d.com.

Hambly, E. C. and E. Pennells. (1975). "Grillage Analysis Applied to Cellular Bridge Decks." The Journal of the Institution of Structural Engineers 53 (7): 267-275.

Hambly, E. C. (1991). "Multicellular Decks." Chap. 5, In Bridge Deck Behavior. 2nd Edition ed., 106-133. New York, NY: Taylor & Francis.

IIW. (2005). Recommendations for Fatigue Design of Welded Joints and Components. The International Institute of Welding, Abington Publishing, Cambridge, England

Jaeger, L. G. and Bakht B. (1982). "The Grillage Analogy in Bridge Analysis." Canadian Journal of Civil Engineering 9 (2): 224-235.

Lightfoot, E. (1964). “A Grid Framework Analogy for Laterally Loaded Plates.” International Journal of Mechanical Sciences 6 (3): 201-208.

Sanchez, T. A. Grunauer (2011). "Influence of Bracing Systems on the Behavior of Curved and Skewed Steel I-Girder Bridges during Construction." PhD School of Civil and Environmental Engineering, Georgia Institute of Technology, Atlanta, GA.

APPENDIX A COMPARISON OF THE STATIC TEST RESULTS OF THE V1 AND V2 DECKS

The following tables present a comparison of the static test results the V1 and V2 decks, at their maximum load level of 22 kip (98 kN). The tables compare the measurements of the third static test of V1 deck Specimen #1, and the measurements of the fourth static test of V2 deck Specimen #1. These results were compared to prevent the residual deck stresses from influencing the results. The static test results are labeled as "V1 Deck" or "V2 Deck".

The measurements at the rectangular rosette gauges and uniaxial strain gauges placed at the V2 deck Specimen #1 stringer-to-tube connections are also presented. These gauges were not present on the V1 deck, therefore no comparison could be made.

Table A-1. Comparison of V1 and V2 Deck Stresses on Top of Deck Plate

Grid Location	Gauge Name	V1 Deck σ (ksi)	V2 Deck σ (ksi)
A1	TDP_7	-5.08	-5.33
A2	TDP_L10	-4.93	-5.34
	TDP_T10	0.42	0.28
A3	S3_T4	-5.61	-4.65
A4	TDP_L11	-5.68	-5.26
	TDP_T11	-0.05	0.79
A5	S4_T4	-5.61	-4.81
A6	TDP_L12	-4.18	-4.04
	TDP_T12	-6.41	-2.95
A7	S5_T4	-5.86	-4.04
A8	TDP_L13	-5.72	-4.62
	TDP_T13	-1.29	-1.49
B1	TDP_6	-5.96	-2.22
B2	TDP_L6	-6.65	-2.85
	TDP_T6	-0.08	-0.16
B3	S3_T3	-5.73	-3.21
B4	TDP_L7	-5.98	-3.77
	TDP_T7	0.93	1.43
B5	S4_T3	-6.89	-5.45
B6	TDP_L8	-15.12	-
	TDP_T8	-28.12	-13.51
B7	S5_T3	-10.16	-8.95
B8	TDP_L9	-9.13	-9.11
	TDP_T9	-6.61	-4.23
D1	TDP_1	-2.48	-1.76
D3	S3_T2	-3.66	-2.38
D5	S4_T2	-4.29	-2.93
D7	S5_T2	-4.92	-3.43
D8	TDP_5	-5.08	-3.32
E1	TDP_L1	-0.94	-0.44
	TDP_T1	0.05	-0.06
E1.5	S2_T1	-1.12	-0.62
E2	TDP_L2	-0.75	-0.19
	TDP_T2	-0.23	-0.27
E3	S3_T1	-0.54	-0.21
E4	TDP_L3	0.34	-0.01

	TDP_T3	2.55	1.44
E5	S4_T1	-1.31	-1.44
E6	TDP_L4	-16.06	-
	TDP_T4	-32.64	-10.71
E7	S5_T1	-6.56	-4.66
E8	TDP_L5	-7.00	-5.22
	TDP_T5	-9.06	-3.05

Table A-2. Comparison of V1 and V2 Deck Stresses on Bottom of Deck

Grid Location	Gauge Name	V1 Deck σ (ksi)	V2 Deck σ (ksi)
A1	BCP_3	7.56	5.40
A2	BDP_L6	-6.90	-1.63
	BDP_T6	-0.31	0.70
A3	S3_B4	10.48	10.17
A4	BDP_L7	-5.85	-1.90
	BDP_T7	-1.52	-0.02
A5	S4_B4	14.15	14.09
A6	BDP_L8	-7.78	-3.65
	BDP_T8	3.33	4.21
A7	S5_B4	15.17	17.04
A8	BDP_L9	-6.27	-3.66
	BDP_T9	-0.97	2.53
B1	BCP_2	8.97	5.53
B2	T2_1	-1.40	-0.72
B3	S3_B3	10.79	10.84
B4	T2_2	6.37	5.12
B5	S4_B3	14.94	15.50
B6	T2_3	19.78	16.09
B7	S5_B3	18.43	19.01
B8	T2_4	30.66	21.95
C8	T1_4	25.67	20.43
D1	BCP_1	3.68	2.92
D4	S3_B2	6.26	5.82
D6	S4_B2	8.74	8.36
D7	S5_B2	11.35	11.01
D8	BDP_4	-4.65	-2.48
E1	BDP_L1	-0.72	0.20

	BDP_T1	0.44	-0.36
E1.5	S2_B1	2.88	2.04
E2	BDP_L2	-0.50	0.01
	BDP_T2	0.43	-0.44
E3	S3_B1	0.80	0.73
E4	BDP_L3	-1.12	-1.98
	BDP_T3	-2.51	-0.84
E5	S4_B1	3.32	2.91
E6	BDP_L4	12.15	9.46
	BDP_T4	29.59	5.58
E7	S5_B1	8.99	6.90
E8	BDP_L5	2.73	1.45
	BDP_T5	6.21	2.35

Table A-3. Comparison of V1 and V2 Deck Stresses at Stringer-to-Deck Welds

Grid Location	Gauge Name	V1 Deck σ (ksi)	V2 Deck σ (ksi)
N/A	S5_DW1 (V1: S5_DW3)	-7.11	-1.68
N/A	S5_DW2 (V1: S5_DW4)	-9.09	-7.22
N/A	S5_DW3 (V1: S5_DW5)	-7.48	-7.37
N/A	S5_DW4 (V1: S5_DW6)	-5.66	0.38

Table A-4. Comparison of V1 and V2 Deck Displacements

Grid Location	Gauge Name	V1 Deck (in.)	V2 Deck (in.)
A1	CP_DISPL_1	-	0.06
B1	CP_DISPL_2	-	0.09
D1	CP_DISPL_3	-	0.09
A3	S3_DISPL_1	0.03	0.10
B3	S3_DISPL_2	0.18	0.15
D3	S3_DISPL_3	0.17	0.14
A7	S5_DISPL_1	0.06	0.15
B7	S5_DISPL_2	0.25	0.22
D7	S5_DISPL_3	0.24	0.20

Table A-5. V2 Deck Specimen #1 Static Test Results at S4-T2

Grid Location	Web Face	Gauge Name	V2 Deck σ (ksi)
B5	North	S4_T2R1	-41.18
		S4_T2R2	-38.81
		S4_T2R3	-22.44
		S4_T2W1	45.48
		S4_T2W2	4.68
B5	South	S4_T2R4	45.18
		S4_T2R5	48.02
		S4_T2R6	21.12
		S4_T2W3	-44.68
		S4_T2W4	-11.22

Table A-6. V2 Deck Specimen #1 Static Test Results at S5-T2

Grid Location	Location	Gauge Name	V2 Deck σ (ksi)
B7	Web	S5_T2R1	21.56
		S5_T2R2	12.84
		S5_T2R3	5.78
		S5_T2W1	18.02
B7	Tube	S5_T2R4	17.36
		S5_T2R5	11.50
		S5_T2R6	4.66
		S5_T2W2	13.06

VITA

Ellen Sarah Grace Sweet was born in Würzburg, Germany on September 15, 1987, to William and Cynthia Sweet. Ellen received her Bachelors of Science degree in Civil Engineering from Lehigh University, in Bethlehem, PA in Spring 2009. Following graduation, she spent two years working as a small bridge inspector. Ellen came back to Lehigh University for her graduate degree in the Fall of 2011, and joined the ATLSS Research Center as a Graduate Assistant in the Summer of 2012. She will receive her Masters in Structural Engineering from the Department of Civil and Environmental Engineering at Lehigh University in December, 2013.